# Stimuli Responsive Microgel Particles and Microgel Crystals as Studied By Light Based Techniques

*By*

**D. KARTHICKEYAN**

**Enrollment No: PHYS02201104009**

**INDIRA GANDHI CENTRE FOR ATOMIC RESEARCH, KALPAKKAM, TAMIL NADU, INDIA, 603 102**

*A thesis submitted to the*

*Board of Studies in Physical Sciences*

*In partial fulfillment of requirements for the Degree of*

**DOCTOR OF PHILOSOPHY**

*of*

**HOMI BHABHA NATIONAL INSTITUTE**


**February, 2017**

## Homi Bhabha National Institute[1]

### Recommendations of the Viva Voce Committee

As members of the Viva Voce Committee, we certify that we have read the dissertation prepared by **D. Karthickeyan** entitled **Stimuli Response of Microgel Particles and Particle Assemblies as Studied by Light Based Techniques** and recommend that it may be accepted as fulfilling the thesis requirement for the award of Degree of Doctor of Philosophy.

Chairman – **Dr. G. Amerandra** **Date:** June 6, 2017

Guide / Convener – **Dr. B. V. R. Tata** **Date:** 6/6/2017

Co-guide - ~~Dr.~~ **T. R. Ravindran** **Date:** 6.6.2017

Examiner – **Dr. Abhijit P Deshpande** **Date:** 06/06/2017

Member 1- **Dr. John Philip** **Date:** 06/6/17

Member 2- **Dr. Raktim Dasgupta** **Date:** 6/6/17

for N.V. Chandra Shekar

Final approval and acceptance of this thesis is contingent upon the candidate's submission of the final copies of the thesis to HBNI.

I/We hereby certify that I/we have read this thesis prepared under my/our direction and recommend that it may be accepted as fulfilling the thesis requirement.

**Date:** 6.6.2017

**Place:** Kalpakkam

<Signature>
**Co-guide** (if applicable)

<Signature>
**Guide**

[1] This page is to be included only for final submission after successful completion of viva voce.

## STATEMENT BY AUTHOR

This dissertation has been submitted in partial fulfillment of requirements for an advanced degree at Homi Bhabha National Institute (HBNI) and is deposited in the Library to be made available to borrowers under rules of the HBNI.

Brief quotations from this dissertation are allowable without special permission, provided that accurate acknowledgement of source is made. Requests for permission for extended quotation from or reproduction of this manuscript in whole or in part may be granted by the Competent Authority of HBNI when in his or her judgment the proposed use of the material is in the interests of scholarship. In all other instances, however, permission must be obtained from the author.

D. Karthickeyan

## DECLARATION

I, hereby declare that the investigation presented in the thesis has been carried out by me. The work is original and has not been submitted earlier as a whole or in part for a degree / diploma at this or any other Institution / University.

D. Karthickeyan

## List of Publications arising from the thesis

### Journal

1. "Identification of Volume Phase Transition of a Single Microgel Particle using Optical Tweezers", **D. Karthickeyan**, Deepak K. Gupta and B. V. R. Tata*, J. Opt.*, **2016,** *18*, 105401-105407
2. *"Temperature-driven volume phase transition of a single stimuli-responsive microgel particle using optical tweezers", Deepak K. Gupta, **D. Karthickeyan**, B. V. R. Tata and T. R. Ravindran, *Colloid Polym. Sci*., **2016**, *294*, 1901-1908
3. "FCC-HCP Coexistence in Dense Thermo-responsive Microgel crystals", **D. Karthickeyan**, R. G. Joshi and B. V. R. Tata, *J. Chem. Phys*., **2017,** *146,*

### Communicated/in preparation

4. "Light scattering studies on immobilized stimuli responsive microgel crystals", **D. Karthickeyan**, R. G. Joshi and B. V. R. Tata, (Manuscript under preparation)
5. "Effect of Temperature on Diffraction of Light From Microgel Crystal Immobilized in a Hydrogel matrix"
   R. G. Joshi, **D. Karthickeyan**, Deepak K. Gupta and B. V. R. Tata, (Manuscript under preparation)

### Conferences

1. *"Yielding behaviour of dense microgel glasses", R. G. Joshi, B. V. R. Tata and **D. Karthickeyan**, AIP conf. proc., **2013**, *1512*, 164.
2. "Effect of UV-irradiation on the Lattice constant of Photonic Crystals of stimuli responsive microgel particles", **D. Karthickeyan**, B.V. R. Tata and R. G. Joshi, MRSI-AGM 2013, held at IGCAR, Kalpakkam Feb 11-13, 2013.

3. “Effect of rate of cooling on crystal structure of Thermo-responsive microgel colloidal crystals across melting”, **D. Karthickeyan**, B. V. R. Tata and R. G. Joshi, in XVIth National conference on surfactants, emulsions and biocolloids (NATCOSEB), Nov., 28-30, 2013 (oral).
4. “Optical tweezers experiment on pH responsive microgel particles”, **D. Karthickeyan**, Deepak K. Gupta and B. V. R. Tata, in NLS-23, S. V. University, Tirupathi, Dec., 3-6, 2014
5. “FCC-HCP coexistence in thermoresponsive microgels crystals”, **D. Karthickeyan**, Deepak K. Gupta, R. G. Joshi and B. V. R. Tata, in Statistical physics of Soft matter, BHU, Varanasi, Nov., 26-30, 2015

***** Papers not included in this thesis.

D. Karthickeyan

**DEDICATED**

**To**

**MY FATHER**

## ACKNOWLEDGEMENTS

I would like to thank people who have played their part in shaping this thesis and help me to evolve as a researcher. Firstly, I would like to express my gratitude to my thesis advisor **Dr. B. V. R. Tata**, for the support, for his patience, motivation, and immense knowledge. His guidance helped me in all the time of research and writing of this thesis.

I would like to thank my doctoral committee members **Dr. G. Amerandra,** Chairman, **Dr. T. R. Ravindran,** co-guide, **Dr. John Philip** and **Dr. Raktim Dasgupta** for their insightful comments and encouragement, but also for the hard question which made me to widen my research from various perspectives.

I express my gratitude to **Dr. S. V. M. Satyanarayana** for his constant inspiration and motivation and **Dr. S. Sivakumar** for his help in understanding many theoretical concepts in optics and holography.

I am indebted for **Mrs. P. V. Rajamani**, **Dr. S. Ayyappan, Dr. K. Saravanan** and **Dr. R. Mohandoss** for going through my thesis and providing valuable suggestions to improve my thesis.

I thank my lab mates **Dr. J. Brijitta**, **Dr. K. Saravanakumar**, **Dr. R. G. Joshi**, **Mr. Deepak K. Gupta**, **Mrs. Soumee Pal** and **Miss. R. Rajitha** for affording comfortable and joyful laboratory environment.

I thank all my batch mates **Manas Ranjan Prusty**, **Sanjay kumar**, **Prema**, **Thangam**, **Samba siva rao**, **Subrata ghosh** and JRF enclavians for providing pleasant and conducive environment during my stay in JRF enclave.

I wish to thank my friends **Mahendran**, **Devidas**, **Manan**, **Anees**, **Srinivasan**, **Radhakrishana**, **Gurpreet Kaur**, **Vairavel**, **Lakshmanan**, **Nilakanda Meher**, **Radhikesh**, **Irshad**, **Raghavendra**, **Saikumaran**, **Shivakumar**, **Raghavendran** and **Bala Krishnan** for giving me unforgettable moments during my stay at IGCAR.

I owe my gratitude to my mother **D. Jothi** whose innumerable sacrifice, unconditional love and confidence has driven me this far. I thank my sisters **D. Mathivani and D. Sathiyavani** for their affection and wishes. I am grateful to my in-laws **A. Chelladurai, C. Chitra** and **C. Narendran** for their understanding and support.

It will not be complete without asserting the role of my wife **C. Roobala** whose love, support and encouragement made me to overcome all the worst situations with ease and made this dissertation possible.

# CONTENTS

## SYNOPSIS

Stimuli responsive microgels are sub-micron/micron sized particles of hydrogels which responds to the external stimuli like temperature, pH, ionic strength and electric field. Poly (N-isopropyl acrylamide) (PNIPAM) microgel system is one of the well-studied stimuli responsive systems which responds to temperature by showing variation in particle size. Upon increasing the temperature, they undergo a sudden transition from swollen to collapsed state around 34 °C, which is known as volume phase transition (VPT), which is reversible. When co-polymerized with acrylic acid (Aac), PNIPAM-co-Aac microgels also respond to pH in addition to temperature. PNIPAM and PNIPAM-co-Aac microgel particles are soft, deformable and they have core shell structure. The core is densely cross-linked whereas the shell (~ 20 – 30 nm) is loosely cross linked and has dangling polymer chains (hairs). Dense suspensions of monodisperse PNIPAM and PNIPAM-co-Aac microgel spheres exhibit structural ordering (liquid-like, crystalline and glass-like) similar to that observed in other colloidal systems as well as in atomic systems. Hence it serves as a model condensed matter system for studying basic phenomena like crystallization, glass transition etc. PNIPAM and PNIPAM-co-Aac microgel particles have emerged as important building blocks for chemical separation and site specific drug delivery. Ordered structures of these microgel crystals are popularly known as tunable photonic microgel crystals as their lattice constant can be tuned using stimuli such as temperature and pH and has application in various sensors.

Many of the above mentioned applications require knowledge about VPT induced either by varying temperature or pH. Dynamic light scattering (DLS) is the conventional technique to determine VPT of the microgel particles. Using DLS, particle diameter (also known as hydrodynamic size), $d$ as a function of $T$ or pH is measured and the large change in $d$ occurring due to sudden swelling/deswelling of microgel particles at a critical $T$ or pH is identified as VPT. However the identification of VPT using DLS requires suspension with particle concentration ~ $10^7$ particles/cm$^3$ to satisfy the Gaussian approximation underlying the Siegert's relation. Further, DLS measurements as well as analysis become complicated if microgel particles are highly polydisperse. To overcome this limitation, we developed an alternative method which involves the measurement of VPT on a single particle using optical tweezers (OT). We have designed and developed an optical tweezers set-up and have been used to identify VPT of PNIPAM-co-Aac microgel particles by studying its pH response.

Monodisperse PNIPAM spheres are known to freeze into RHCP (random hexagonal close packed) structure under as prepared condition and into FCC (face centered cubic) structure upon annealing which is analogous to that of hard sphere suspension with volume fraction, $\phi = 0.5$. Unlike hard spheres, PNIPAM microgel particles are soft and deformable in addition to the core-shell structure with highly cross-linked dense core and a thin shell (~ 20 – 30 nm) consists of dangling polymer chains. Joshi *et. al*., have shown that PNIPAM microgel particles undergo deswelling due to osmotic pressure exerted by neighbouring microgel spheres when the suspensions is

concentrated beyond a volume fraction of 0.74. Further it was shown that under osmotic compression, particles exhibit sub-diffusion behaviour at short times and was attributed to entanglement (overlap) of dangling polymer chains (hairs) between neighbouring PNIPAM microgel spheres. However, there have been no reports of structural studies on dense PNIPAM microgel crystals, in particular when concentrated to a volume fraction beyond 0.74. Here we report light scattering (static and dynamic) and UV-Visible spectroscopy studies to understand the crystal structure of dense PNIPAM microgel crystals with volume fraction below and above closed pack limit.

Having investigated the crystal structure of neutral PNIPAM microgels at high concentration, we have investigated the crystal structure of dense ionic PNIPAM-co-Aac microgel particles. In addition to thermoresponsive nature, PNIPAM-co-Aac microgel particle are pH responsive due to the presence of acrylic acid moieties and exhibits VPT with respect to pH at 4.25. At pH < 4.25, these microgel spheres are in protonated (neutral) state and at pH > 4.25, they are in deprotonated (charged) state. Unlike neutral PNIPAM microgel particles, PNIPAM-co-Aac microgel particles crystallize at very low volume fraction and remain in fluid state even above close-packed limit. The phase behaviour of PNIPAM-co-Aac microgel system is expected to be pH dependent as they exhibit VPT with respect to pH, and also interaction potential of PNIPAM-co-Aac microgel particles changes from repulsive to weekly attractive across pH (VPT-pH). Theoretical calculations have predicted that ionic microgels will exhibit non-cubic structures at high concentration. It is important to understand the effect of change in interaction potential across VPT-pH on the structure of dense microgel crystals. Here, we report the crystal structure of dense PNIPAM-co-Aac microgel particles as a function of pH at constant number density using static light scattering technique.

Crystals of stimuli responsive microgel particles are known as tunable photonic crystals and have potential application in sensors, filters, etc. These crystals are fragile and relatively unstable against shear and hence are limited for fabricating any devices. This limitation is overcome by immobilizing the colloidal crystal in a polymer hydrogel matrix which is known to improve their stability against shear resistance and make them as portable photonic crystals. Though, hard spheres and charged colloidal crystals are immobilized and well-studied for their applications, there are not many studies exist on the immobilization of stimuli responsive microgel crystals. This thesis reports the static and dynamic light scattering studies on immobilized PNIPAM microgel crystals and their response to temperature.

To address the issues mentioned above, PNIPAM and PNIPAM-co-Aac microgel suspensions of various particle sizes have been synthesized by free radical polymerization. Synthesized particles were characterized for their average size and size polydispersity using dynamic light scattering. DLS and optical tweezers (OT) were used to identify the VPT. The advantage of using OT over DLS to characterize the VPT is discussed in chapter 3. Structural ordering and dynamics in dense microgel suspensions in their ordered and disordered state were investigated by employing light based techniques such

as static light scattering, dynamic light scattering and UV-Visible spectroscopy. The thesis is organized in to seven chapters and the contents of each chapter are summarized as follows.

**Chapter 1 – Introduction**

Colloidal suspensions of hard spheres, charged colloids and stimuli responsive microgels are discussed with respect to their stability, interparticle interactions, phase behaviour and dynamics in dense colloidal systems. Motivation for the thesis along with the reported literature on PNIPAM microgels and PNIPAM-co-Aac microgels are presented in this chapter.

**Chapter 2 – Experimental techniques and sample synthesis**

Synthesis of PNIPAM and PNIPAM-co-Aac microgel particles through free radical precipitation polymerization method is discussed. Experimental techniques like optical tweezers for the identification of VPT on a single microgel particle, SLS and UV-Visible spectroscopy for the investigation of structural ordering in microgel crystals, DLS to study the dynamics of these microgel suspensions and their theory is presented in detail.

**Chapter 3 – Identification of Volume Phase Transition (VPT) of a single microgel particle using Optical Tweezers (OT)**

Conventionally VPT is identified using DLS which requires particle concentration of $n_p \sim 10^7$ particles/cm$^3$. Size polydispersity in particles strongly influences the DLS data and makes the analysis difficult to obtain particle size and accurate identification of VPT. Since VPT is the property of the polymer, measurement on single particle should enable to identify the VPT of the particle unambiguously. Earlier, optical tweezers have been employed for the measurement of single particle's property like refractive index, rigidity, electrophoretic forces, etc. We have indigenously designed and assembled optical tweezers and employed it in identifying VPT of PNIPAM-co-Aac microgel particles as a function of pH. In this chapter, technical details of our indigenously designed and assembled optical tweezers are presented. The sample preparation for the experiment to determine the trap stiffness as a function of pH and the analysis methods are discussed. At each pH, individual particle is trapped and its position in the trap as function of time is recorded to extract the trap stiffness. Trap stiffness as a function of pH showed a sudden jump at pH ~ 4.25 which is identified as VPT-pH and it is in good agreement with the DLS experiment. Numerical calculation of trap stiffness as a function of pH also showed sudden jump across VPT and agrees qualitatively with the experimental results. The reasons for the sudden jump in the trap stiffness are discussed by numerically computing trap stiffness as a function of size and refractive index variation as a function of pH.

**Chapter 4 – Structure and dynamics of thermo-responsive dense microgel crystals**

Self-assembled colloidal crystals often co-exist in FCC-HCP crystal structures due to very less free energy difference ($\sim 10^{-3} k_B T$ ) between FCC and HCP structure. Hard sphere colloidal crystals freezes in RHCP and FCC co-existing structures at volume fraction, $\phi \approx 0.5$ . Hard sphere colloidal crystals tend towards thermodynamically favoured FCC structure on the time scales of months. Unlike hard spheres, stimuli responsive microgels are soft and respond to external stimuli like temperature, pH, ionic strength, etc., by undergoing swelling/de-swelling. This results in not only size change but also change in the interaction potential, hence their phase behaviour. At $\phi \approx 0.5$, the equilibrium crystal structure of PNIPAM microgel crystals is found to be FCC and is consistent with the literature. There are no reports on the crystal structure of dense PNIPAM microgel suspensions with $\phi > 0.74$. Here, we present the detailed structure of neutral PNIPAM microgel crystals with $\phi < 0.74$ and $\phi > 0.74$ using SLS technique as well as UV-Visible spectroscopy. Sample with $\phi < 0.74$ initially crystallized in FCC-HCP coexisting structure whereas upon annealing and cooled at 0.5 °C/hour, the suspension crystallized in FCC structure, consistent with the literature. As prepared sample with $\phi > 0.74$ exhibited glass-like disorder and upon annealing with a cooling rate of 0.5 °C/hour the sample has crystallized into FCC-HCP coexistence. Upon further annealing with a cooling rate of 0.1 °C/hour the sample was found to remain FCC-HCP coexistence. The entanglement of dangling polymer chains of neighbouring PNIPAM spheres, inferred based on the sub-diffusive dynamics at short times, was argued to be the reason for FCC-HCP coexistence. The entanglement of polymer chains stabilizes the HCP structure and is consistent with the recent reports on stabilizing HCP phase in hard sphere crystals by adding interacting polymer chains. Further the evolution of crystal phases across freezing transition was monitored using UV-Vis spectroscopy and found that at freezing transition, the suspension got crystallized in to FCC structure and with further cooling HCP structure gets stabilized. We observed the change in cooling rates alter only the relative fractions of FCC and HCP phases in the coexistence state.

**Chapter 5 – Structure and dynamics of pH responsive dense microgel crystals**

The crystal structure of dense suspensions of neutral PNIPAM microgel suspensions was found to be FCC-HCP coexisting structure at high concentration. The crystal structure of microgels with electrostatic interaction at such high concentration has not been investigated. Theoretical calculations have predicted non-cubic structures at high concentration in ionic microgel system. Experimental investigations on charged microgel systems with volume fraction, $\phi > 0.8$ have reported RHCP structure. Here, we have investigated the crystal structure of dense PNIPAM-co-Aac microgel particles which are pH responsive and exhibits VPT at pH 4.25. The phase behaviour is expected to be pH dependent. We have prepared PNIPAM-co-Aac microgel crystals with same number density, $n_p$ at different pH to understand the effect of change in interaction potential in dense microgel suspension on its structure. The structure of dense PNIPAM-co-Aac

microgel crystals in as prepared condition is found to be to FCC-HCP coexisting structure. At low pH (3.40), the microgel suspension with $\phi$ ~ 0.5, upon annealing and cooled at 0.1 °C/hour, is found to crystallize in FCC structure whereas the sample at pH 5.0 (charged state and $\phi$ ~ 1.6) remained in FCC-HCP coexisting structure. The dynamics of these particles at short times is found to be diffusive at pH 3.40 ($\phi$ ~ 0.5) and it is sub-diffusive at all other pH (3.7, 4.0, 4.35, 4.7, 5.0). At high concentration, the entanglement of dangling polymer chains of neighbouring particles is argued to be the reason for the observed sub-diffusive dynamics at short times despite the electrostatic repulsion between polymer chains (at pH > 4.25). We conclude that, at volume fraction, $\phi$ > 0.74, PNIPAM-co-Aac microgel particles behaves like neutral particles.

**Chapter 6 – Light scattering studies on the immobilized stimuli responsive microgel crystals**

Having determined the structure of Colloidal crystals unambiguously at high concentration, we have immobilized these stimuli responsive microgel crystal in a hydrogel matrix, to preserve the ordering in the sample against shear. It is important to immobilize these crystals to retain their periodic arrangement in a matrix to prolong their utility. Immobilization of these crystals in hydrogel matrix have provided mechanical strength needed for colloidal crystals which are used as filters, chemical sensors, photonic band gap materials, optical switches, etc. Lyon *et. al*., has reported that microgel crystals upon immobilization gets disordered. The structural ordering before and after immobilization in loosely cross-linked hydrogel, the effect of hydrogel matrix on the stimuli induced response of these crystals is essential for all practical applications. In closed packed condition, microgel crystals upon on immobilization are reported to have their crystalline order to get disturbed and particles becomes aggregate. Detailed structural characterization of stimuli responsive microgel crystals and their dynamics has not been well-studied. Here, we have successfully immobilized the microgel crystals without disturbing their order in a loosely cross-linked hydrogel matrix and show that the structure of microgel crystal before and after immobilization remains same. The response of immobilized microgel crystals is found to vary non-monotonously and that is understood in terms of particle size, particle form factor and refractive index of the particle.

**Chapter 7 – Summary and conclusions**

This chapter presents the summary and conclusions of the studies carried out in understanding the structural ordering of stimuli responsive microgels as a function of stimuli. The key findings of the thesis are as follows.

Key findings of this thesis are summarized below.

1. Indigenously designed and developed an optical tweezers set-up. Using which for the first time shown that VPT can be identified on a single microgel particle and

shown that it gives a sharp transition as compared to that of conventional method of identifying VPT using DLS. VPT manifests as a sudden jump in the trap stiffness and is understood to arise from sudden decrease in the particle size with concomitant increase in the refractive index of the particle.

2. For the first time FCC-HCP coexistence is shown to be the stable state for dense PNIPAM microgel crystals with volume fraction, $\phi > 0.74$ by performing detailed annealing studies. It is also shown that PNIPAM microgel crystals with volume fraction, $\phi < 0.74$ crystallize into FCC structure. Entanglement of dangling polymer chains between shells of neighboring microgel spheres is shown to occur in PNIPAM microgel crystals with, $\phi > 0.74$ and is evidenced by observing sub-diffusive behavior at short times. The entanglement is shown to disappear upon heating the crystals well about their melting temperature.
3. Through detailed annealing studies, it was shown that overlap of dangling polymer chains between the shells of neighbouring spheres is responsible for the stability of FCC-HCP coexistence observed in microgel crystals with $\phi > 0.74$.
4. In dense pH responsive microgel crystals, as prepared samples in the pH range 3.00 to 5.00 crystallized in FCC-HCP coexisting structure. At pH = 3.40 ($\phi \approx 0.5$), the sample upon recrystallization was found to crystallize into FCC structure whereas the samples at other pH (3.7, 4.0, 4.35, 4.7, 5.0) with $\phi > 0.74$ has remained in the FCC-HCP state. Dynamics of PNIPAM-co-Aac microgel particles at short times in dense suspensions is found to be diffusive in sample with $\phi < 0.74$ and is sub-diffusive in sample with $\phi > 0.74$. The phase behaviour of ionic microgel crystals with $\phi > 0.74$ was found to be similar to that of dense microgel crystals of uncharged PNIPAM spheres. Our results suggested that coulombic interaction between PNIPAM-co-Aac microgel particles is not dominant under dense conditions and does not play a major role in stabilizing the crystal structure.
5. Stimuli responsive PNIPAM-co-Aac microgel crystals were successfully immobilized in poly-acrylamide hydrogel (PAAm) matrix. The structure of stimuli responsive microgel crystal is shown to remain unaltered before and after the immobilization. Immobilization of microgel crystals is shown to extend the stability of microgel crystals against melting beyond VPT. Bragg peak intensity as a function of temperature from immobilized microgel crystals was found to vary non-monotonically. That non-monotonic behaviour is shown to arise from the simultaneous decrease of particle diameter with concomitant increase in the refractive index of the microgel particle with increasing temperature.

## LIST OF FIGURES

## List of Tables

## List of symbols

| | | |
|---|---|---|
| Hard sphere interaction potential | : | $U_{HS}(r)$ |
| Inter-particle distance | : | $r$ |
| Hydrodynamic diameter or diameter of the microgel particle | : | $d$ |
| Particle number density | : | $n_p$ |
| Conductivity | : | $\sigma$ |
| Effective surface charge density | : | $\sigma_e$ |
| Avagardo number | : | $N_A$ |
| Number of particles | : | N |
| Hydrogen ions | : | $H^+$ |
| Equivalent conductance of $H^+$ | : | $\lambda_{H^+}$ |
| Charge of an electron | : | $e$ |
| Disassociation constant | : | $pK_a$ |
| Ionic strength | : | $I$ |
| Time lag | : | $\tau$ |
| Characteristic decay time | : | $\tau_c$ |
| Time | : | $t$ |
| Scattering wave vector | : | $\vec{q}$ |
| Normalized intensity auto correlation function | : | $g^{(2)}(q,t)$ |
| Normalized electric field auto correlation function | : | $g^{(1)}(q,t)$ |
| Scattered intensity | : | $I_s(q,t)$ |
| Scattered electric field | : | $E_s(q,t)$ |
| Coherence factor | : | $\beta$ |
| Free diffusion coefficient | : | $D_0$ |
| Decay constant | : | $\Gamma$ |
| Boltzmann constant | : | $k_B$ |
| Viscosity of the medium | : | $\eta$ |
| Temperature | : | $T$ |
| Average decay constant | : | $\bar{\Gamma}$ |
| Average diffusion constant | : | $\bar{D}$ |
| Time exponent | : | $\alpha$ |
| Time | : | $t$ |

| | | |
|---|---|---|
| Scattering volume | : | $V_s$ |
| Scattering angle | : | $\theta$ |
| Planck's constant | : | $h$ |
| Incident wave vector | : | $\vec{k}_i$ |
| Scattered wave vector | : | $\vec{k}_s$ |
| Refractive index of the medium | : | $\mu_m$ |
| Refractive index of the particle | : | $\mu_p$ |
| Refractive index of the suspension | : | $\mu_s$ |
| Relative refractive index | : | $\mu$ |
| Incident intensity | : | $I_0$ |
| Wavelength | : | $\lambda$ |
| Particle form factor or Intra-particle structure factor | : | $P(q)$ |
| Inter-particle Structure factor | : | $S(q)$ |
| Inter-planar distance | : | $d_{hkl}$ |
| Lattice constant of FCC structure | : | $a_F$ |
| Lattice constants of HCP structure | : | $a_H, c_H$ |
| Glancing angle | : | $\theta_g$ |
| Miller indices | : | ($hkl$) |
| Nearest neighbour distance | : | $d_{nn}$ |
| Volume fraction | : | $\phi$ |
| Coherence factor | : | $\beta$ |
| Normalized intensity cross correlation | : | $g_{12}^{(2)}(q,\tau)$ |
| Non-ergodicity factor | : | $Y$ |
| Time averaged scattered intensity | : | $\langle I_s(q)\rangle_t$ |
| Ensemble averaged scattered intensity | : | $\langle I_s(q)\rangle_E$ |
| Mean square fluctuation of scattered intensity | : | $\sigma_I^2$ |
| Percentage transmission | : | %T |
| Transmitted intensity | : | $I_T$ |
| Absorbance | : | $abs$ |
| Molar extinction co-efficient | : | $\vartheta$ |
| Molar concentration | : | $C$ |
| Optical path length | : | $l$ |

| | | |
|---|---|---|
| Trap stiffness | : | $\kappa$ |
| Trap stiffness along *x* direction | : | $\kappa_x$ |
| Scattering force | : | $F_{scat}$ |
| Gradient force | : | $F_{grad}$ |
| Angle of incidence | : | $\theta_1$ |
| Angle of refraction | : | $\theta_2$ |
| Beam waist of the laser | : | $\omega$ |
| Relative difference of the dielectric constants | : | $\varepsilon$ |
| Dielectric constant of the particle | : | $\varepsilon_p$ |
| Dielectric constant of the medium | : | $\varepsilon_m$ |
| Eccentricity | : | $\epsilon$ |
| Optical trap potential | : | $U$ |
| Probability distribution | : | $P(x)$ |
| Line width distribution | : | $G(\Gamma)$ |
| Laser power | : | $P$ |
| Force along *x* direction | : | $F_x$ |
| Freezing point | : | $\phi_f$ |
| Melting point | : | $\phi_m$ |
| Boltzmann constant | : | $k_B$ |
| Temperature | : | $T$ |
| Glass transition point | : | $\phi_g$ |
| Cubic close packed volume fraction | : | $\phi_{max}$ |
| Nearest- neighbour distance | : | $d_{nn}$ |
| Debye screening length | : | $\xi^{-1}$ |
| Charge of an electron | : | $e$ |
| Number of monovalent charges | : | $Z$ |
| Radius of the particle | : | $a$ |
| Salt concentration | : | $C_s$ |
| Van der Waals interaction potential | : | $U_{vdW}(r)$ |
| Hamaker consant | : | $A_H$ |
| Radius of the core | : | $a_c$ |
| Thickness of the shell | : | $\rho$ |
| Velocity | : | $V(t)$ |

| | | |
|---|---|---|
| Mass of the particle | : | $m$ |
| Co-efficient of friction | : | $\zeta$ |
| Viscosity of the solvent | : | $\eta_s$ |
| Random force | : | $F(t)$ |
| Mean square displacement | : | $\langle r^2(t) \rangle$ |
| Brownian time | : | $\tau_B$ |
| Cage rearrangement time | : | $\tau_R$ |
| Free diffusion coefficient | : | $D_0$ |
| Time exponent | : | $\alpha$ |
| Short time diffusion co-efficient | : | $D_s$ |
| Long time diffusion co-efficient | : | $D_L$ |
| Laser power | : | $P$ |
| Van de Hulst complex forward scattering factor | : | $S(0)$ |
| Trapping efficiency | : | $Q$ |
| Pair correlation function | : | $g(r)$ |
| Osmotic pressure due to mixing of polymer and solvent | : | $\prod_{mix}$ |
| Osmotic pressure due to elastic deformation of polymer | : | $\prod_{elastic}$ |
| Osmotic pressure due to charges on polymer network | : | $\prod_{ion}$ |
| Flory polymer-solvent interaction parameter | : | $\chi$ |
| Molar volume of the solvent | : | $v_s$ |
| Polymer volume fraction within the particle in swollen state | : | $\Phi$ |
| Polymer volume fraction within the particle in collapsed state | : | $\Phi_o$ |

# List of Abbreviations

| | | |
|---|---|---|
| PMMA | : | Poly methyl methacrylate |
| PNIPAM | : | Poly (N-isopropyl acrylamide) |
| VPT | : | Volume phase transition |
| DLS | : | Dynamic light scattering |
| OT | : | Optical tweezers |
| SLS | : | Static light scattering |
| 3D- DLS | : | Three dimension-Dynamic light scattering |
| NIPAM | : | N-isopropyl acrylamide |

| | | |
|---|---|---|
| BIS | : | N, N’-Methelenebisacrylamide |
| SDS | : | Sodium dodecyl sulphate |
| KPS | : | Potassium persulfate |
| PNIPAM-co-Aac | : | Poly (N-isopropyl acrylamide)-co-acrylic acid |
| Aac | : | Acrylic acid |
| CMC | : | Critical micelle concentration |
| SPD | : | Size polydispersity |
| NWML | : | Nominal molecular weight limit |
| QELS | : | Quasi elastic light scattering |
| PCS | : | Photon correlations spectroscopy |
| MSD | : | Mean square displacement |
| RGD | : | Rayleigh-Gans-Debye |
| FCC | : | Face centered cubic |
| BCC | : | Body centered cubic |
| HCP | : | Hexagonal close packed |
| RHCP | : | Random hexagonal close packed |
| PMT | : | Photo multiplier tube |
| APD | : | Avalanche photo diodes |
| AOM | : | Acousto-optic modulators |
| UV-Vis spectroscopy | : | Ultra violet – Visible spectroscopy |
| OT | : | Optical tweezers |
| NA | : | Numerical aperture |
| CCD | : | Charge coupled device |
| CPD | : | Charge polydispersity |
| RCP | : | Random close packed |
| SANS | : | Small angle neutron scattering |
| SAXS | : | Small angle X-ray scattering |

# CHAPTER 1

# INTRODUCTION

This chapter presents an introduction to colloidal dispersions, types of colloidal dispersions and their phase behaviour, stimuli responsive microgel particles as building blocks for colloidal crystals with relevant literature. This chapter also discusses the motivation for the thesis and key findings of the thesis.

## 1.1 Colloidal suspensions

Colloidal suspensions are heterogeneous systems composed of solid particles of size ranging from 10 nm to 1 μm as dispersed phase (micron/submicron sized solid particles) dispersed uniformly in a solvent such as water. The size range ensures that Brownian forces arising due to thermal fluctuations in the solvent influence the dynamics of the colloidal particles. Uniformly dispersed solid particles in the suspension tend to aggregate due to van der Waals attraction between them. In order to prevent the aggregation due to van der Waals attraction between particles, these colloidal suspensions are stabilized by adding a thin layer of polymer on the particle surface, known as steric stabilization or by adding charges on the surface of the colloidal particles known as charge stabilization. Suspensions of monodisperse colloidal particles display rich phase behaviour and exhibit structural ordering similar to that observed in atomic systems *viz.*, crystalline, liquid, gas and even glasses [1-6]. At lower concentration of particles, colloidal suspensions exhibit structural ordering similar to liquid or fluid phase as stable equilibrium state. Under dense conditions, colloidal suspensions freeze into either spatially ordered crystalline state or into a kinetically arrested glassy state [1-6]. Ordered structures of colloids, popularly known

as colloidal crystals exhibit iridescence due to Bragg diffraction of visible light [7]. Colloidal particles are three orders of magnitude larger in size as compared to atoms. Due to the large structural length, the number density, $n_p = \frac{N}{V}$ (where N is the number of particles in volume, V) of colloidal suspension is roughly $10^{12}$ times smaller than in atomic systems. It is reflected in the elastic constant of the system being $10^{12}$ weaker than atomic systems despite the fact that free energy per particle of atomic and colloidal systems are comparable [8,9]. Therefore, colloidal crystals are extremely soft where the ordering can be disturbed easily. Colloidal particles exhibit slow dynamics typically between microseconds to hundreds of seconds which facilitate to study the structure and dynamics of metastable phases. Hence, colloidal systems serve as model condensed matter system to explore non-equilibrium processes like crystal nucleation and growth [10-14] and the glass transition [15,16] which are found common with atomic or molecular systems. In addition specific to colloidal system are, various kinds of interaction potentials ranging from highly repulsive to weak attractive, create more interest in probing the system. Ordered structures of monodisperse colloids are found to have several high tech applications *viz.*, sensors [17-20], Bragg filters [21,22], optical switches [23,24], display devices [25], photonic crystals [26,27], template for the growth of novel materials [28,29], etc.

### 1.2 Hard sphere colloidal suspensions

Hard sphere colloidal suspensions are the simplest systems investigated for its phase behaviour as they exhibit fluid and solid phase and the phase behaviour of hard sphere suspensions can be predicted by a single parameter, the volume fraction of the suspension, $\phi$ (= $n_p \pi d^3/6$) and $d$ is the hard sphere diameter. The interaction potential between hard spheres, $U_{HS}(r)$ can be expressed as

$$U_{HS}(r) = \begin{cases} 0 & r \geq d \\ \infty & r < d \end{cases} \tag{1.1}$$

where $r$ is inter-particle distance. Crystallization in hard spheres is driven by entropy as there are no other interactions responsible for structural ordering. Equilibrium crystal structure of hard spheres was reported to be face centered cubic (FCC) structure [11,30]. Sterically stabilized poly methyl methacrylate (PMMA) suspensions constitute the best example for hard sphere suspensions [31-33]. The phase diagram of monodisperse hard sphere colloidal suspension is shown in Fig. 1.1 [34].

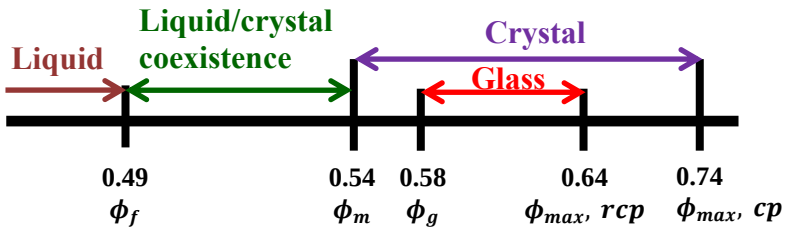


**Figure 1.1** Phase diagram of monodisperse hard sphere suspensions.

Monodisperse suspenion of hard spheres exhibit fluid phase below $\phi = 0.49$ and upon increasing $\phi$ beyond 0.49 exhibit crystalline order which coexists with fluid phase. Hard sphere suspension form entropically driven colloidal crystals above $\phi_f = 0.494$ and sample becomes completely crystalline above $\phi_m = 0.545$. The crystal structure of hard sphere suspension is FCC structure [35-37]. However, hexagonal close packed structure (HCP), FCC-HCP coexistence and random hexagonal close packed structure (RHCP) are also observed due to free energy difference between FCC and HCP structure being less than $10^{-3}k_BT$ per particle [38,39]. Here $k_B$ is the Boltzmann constant and $T$ is the temperature. Further increase in $\phi$ beyond 0.58, hard sphere suspensions were found to freeze into kinetically arrested non-equilibrium glassy phase. $\phi_g = 0.58$ is known as a hard-sphere glass transition volume fraction. A disordered phase prepared at this concentration will

remain in the same state due to lack of particle mobility, which frustrates the system evolving from glassy state to equilibrium crystalline state. The glassy phase of hard sphere system continues upto $\phi = 0.64$ where randomly organized particles touch each other to exhibit random close packed structure (RCP). Regularly packed monodisperse spheres form FCC or HCP structures which are different in the stacking sequence, can have a maximum volumefraction, $\phi_{max} = 0.74$. Particles arranged in ABCABC…. stacking gives rise to FCC structure and with ABABAB… stacking gives HCP structure (Fig. 1.2). However, size polydispersity (SPD) which is inevitable to colloids results in different phase behaviour [40]. SPD is known to shift the freezing point to a shift to higher volume fraction. Suspensions with SPD < 11 % were observed to show crystallization and SPD > 11 % showed glassy (disordered) state.

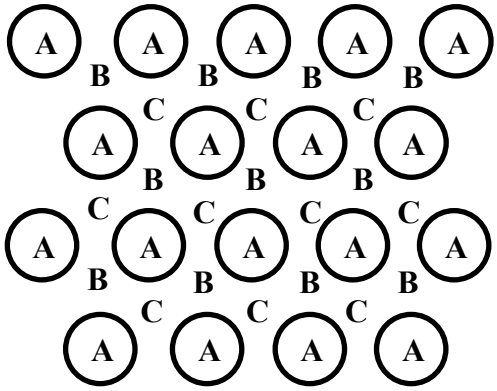


**Figure 1.2** Hexagonally packed planes of spheres with particles in this planes are denoted by a circle and denoted by A. Particle positions in the two possible subsequent planes are denoted by B and C with each plane displaced by a distance of $\sqrt{\frac{2}{3}}d_{nn}$along the orthogonal direction to this plane. $d_{nn}$ is the distance between the nearest neighbours.

### 1.3 Charge stabilized colloidal suspensions

Unlike hard sphere suspenions, charged stabilized suspensions freeze into a crystalline state due to electrostatic interactions which are predominantly repulsive and described by Derjaguin-Landau-Verwey-Overbeek (DLVO) theory [2,41,42]. As per the DLVO theory, the interaction potential between charged colloidal particles is the sum of screened Coulombic repulsion, $U_s(r)$ plus short range van der Waals attraction, $U_{vdW}(r)$.

$$U(r) = U_s(r) + U_{vdW}(r) \tag{1.2}$$

The screen Coulomb interaction [8] between charged collodial particles is given by,

$$U_s(r) = \frac{e^2}{\varepsilon_m}\left[\frac{Ze^{\xi a}}{1+\xi a}\right]\frac{e^{-\xi r}}{r} \tag{1.3}$$

where $e$ is the charge of an electron, $\varepsilon_m$ is the dielectric constant of the medium, $Z$ is surface charge on the particle, $a$ is the radius of the particle, $r$ is the centre to centre distance between particles and $\xi$ is the inverse Debye screening length given by,

$$\xi^2 = \frac{4\pi e^2}{\varepsilon k_B T}\left(n_p Z + C_s\right) \tag{1.4}$$

where $k_B$ is the Boltzmann constant, $T$ is the temperature, $n_p Z$ is the number of counterions and $C_s$ is the salt concentration, in the suspension.

The van der Waals attraction, $U_{vdW}(r)$ is given by,

$$U_A(r) = -\frac{A_H}{6}\left[\frac{2a^2}{r^2-4a^2} + \frac{2a^2}{r^2} + ln\left(\frac{r^2-4a^2}{r^2}\right)\right] \tag{1.5}$$

where $A_H$ is the Hamaker constant. In the case of hard spheres, $\phi$ is the only parameter to study the phase behaviour, in charged colloids one can vary $Z$, $C_s$ in addition to volume fraction, $\phi$ and realize various phases. Deionized suspensions of charged colloids exhibit crystalline ordering at a volume fraction as low as 0.005 due to long range screened Coulomb interaction. Addition of salt decreases the strength and range of screened coulomb interaction results in the melting of crystalline order. A typical phase diagram of charged colloid system is shown in Fig. 1.3 [4].

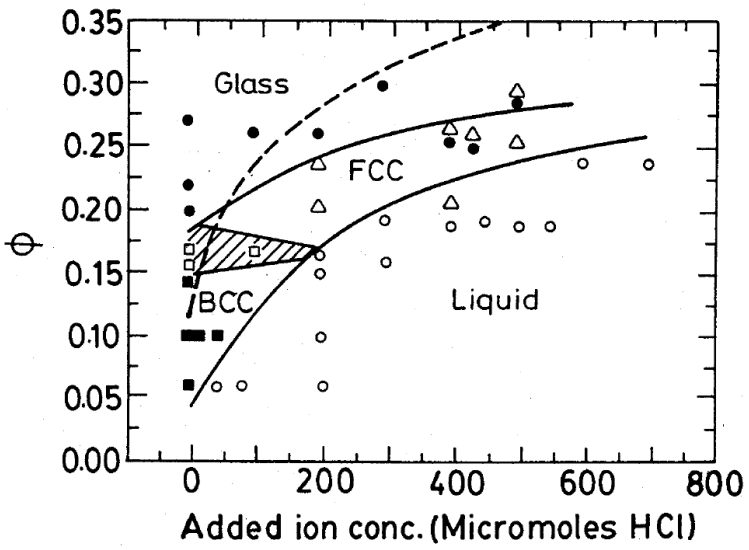


**Figure 1.3** Phase diagram of charged polystyrene colloidal suspensions reported in Ref. [4]. Open circles indicate Liquid, open triangle : fcc, closed square : bcc, open square : bcc-fcc coexistence, closed circles : glass. The continuous lines are guide to eye. Dashed line is fcc-liquid phase boundary for a similar point charge Yukawa system.

It can be seen from the phase diagram that charge colloids exhibit not only FCC ordering but also BCC (body centered cubic) at lower volume fraction, $\phi$ and low salt concentration [43]. During this transition, the suspension also exhibited BCC-FCC coexistence for a range of $\phi$ and charge density. At higher $\phi$, the suspension becomes glassy. Since the interactions are purely repulsive, the phase diagram contains fluid-solid phase but not a gas-liquid or gas-solid phase.

Charged colloids with high charge density particle suspensions was found to turn inhomogeneous (in the form of gas-solid and gas-liquid coexistence) [2]. The transition from homogeneous phase (observed in low charge density particles) to inhomogeneous phases (observed in high charge density particles) was understood to arise from to long-range attraction between like charged colloids mediated by counter ions, in addition to usual screened coulomb repulsion [44,45]. Confocal microscopy experiments on dilute suspensions of highly charged polystyrene particles showed bound pairs, which constitute the direct evidence for the existence of long range attractive interaction between charged colloidal particles mediated counter by ions [46]. In the case of charged colloids not only size polydispersity (SPD) but also charge polydispersity (CPD) plays an important role in determining the phase behaviour. 26% of CPD was shown to disrupt the crystalline order in charged colloidal crystals. Deionised charged colloids with CPD up to 26% exhibit crystalline order whereas hard sphere suspensions are known to freeze into crystalline order when SPD < 11% [47].

### 1.4 Stimuli responsive microgel suspensions

In the case of hard spheres and charged colloids, the size of the particle as well as size polydispersity is fixed during the synthesis of these particles in a suspension. Hence, phase behaviour of these suspensions can be varied only by changing the number density, $n_p$ but not by particle size. Stimuli responsive microgel suspensions are free from such limitation as their particle size can be varied by varying the external stimuli like temperature, pH, ionic strength, pressure etc. These microgel particles swell/deswell in size in response to the external stimuli. Microgel particles have core-shell structure, with a dense core of cross-linked polymer chains and a thin

shell (~ 20 nm to 30 nm) of dangling polymer chains. When microgel particles are suspended in a polar solvent such as water, polymer networks expand/contract with respect to external stimuli which manifests in swelling/deswelling of microgel particles. Stimuli responsive microgel particles are of considerable interest in view of their numerous practical applications based on property changes (e.g. particle size, refractive index, swelling/ deswelling etc.) across VPT [48]. Among several stimuli responsive microgels, Poly (N-isopropyl acrylamide) (PNIPAM) microgel system is one among the mostly studied stimuli responsive microgel system, as it is thermoresponsive and undergo swelling/deswelling upon decreasing/increasing the temperature [49,50]. The response is reversible. PNIPAM microgel particles, when functionalized with acrylic acid groups (Aac) respond to pH and are referred to as poly (N-isopropyl acrylamide-co-acrylic acid) (PNIPAM-co-Aac) microgel particles [51]. Because of their unique reversible stimuli response, PNIPAM and PNIPAM-co-Aac microgel particles have emerged as important materials for practical applications such as sensors, chemical separation and drug delivery [52,53].

### 1.4.1 Thermo responsive behaviour of PNIPAM microgel particles

PNIPAM microgel particles suspended in water respond by deswelling (swelling) with increase (decrease) in temperature, *T*. PNIPAM microgel particles undergo sudden decrease in the diameter of the particle at around 34 ºC (Fig. 1.4(a)). Upon increasing the temperature, this sudden collapse in volume of PNIPAM particles is termed as volume phase transition (VPT) and the corresponding temperatuare as volume phase transition temperature [54,55]. The breadth of the VPT and temperature at which it occurs can be manipulated with the addition of co-monomers and cross-linker's concentratoin during the synthesis of microgel particles

[56]. Below VPT, microgel particles are in swollen state (hydrophilic state). Water molecules around the polymer chains form a structure surrounding the polymer and forms hydrogen bond with the amide groups which keep the particle in its swollen state. As temperature is increased, hydrogen bond between amide groups and water molecules gets broken and water molecules are expelled from the polymer chains. This results in the deswelling of microgel particles (Fig. 1.4(b)) [57,58]. PNIPAM microgel particle contain ~2-3% polymer and the rest is water (solvent) in the swollen state in contrast to the deswollen state where microgel contain about 60% of polymer and 40% of water [59]. Since microgel particles are rich in water content in their swollen state, the suspension appears transperent below VPT due to close refractive index matching of microgel particles with that of the surrounding solvent (water). The increase in the polymer content inside the particle above VPT turns the suspension turbid because of increased refractive index of the particles leading to poor index matching between the particle and the solvent. Beyond VPT, the diameter of the particle is found not to change significantly (Fig. 1.4(a)).

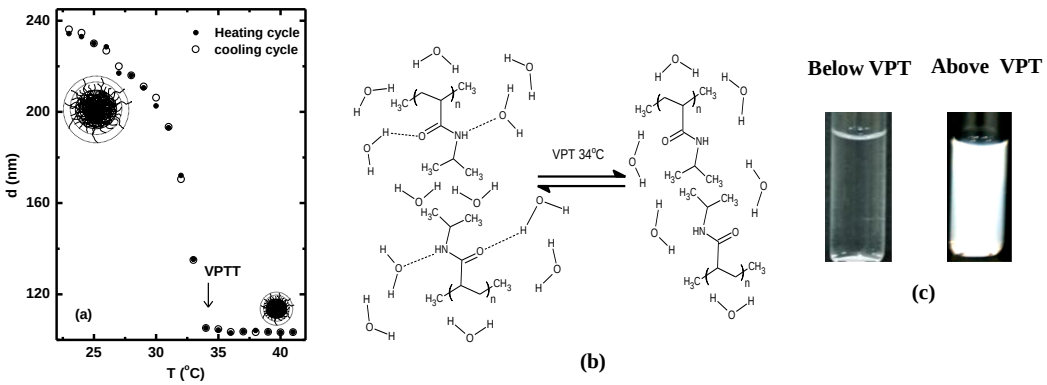


**Figure 1.4** (a) Variation of hydrodynamic diameter, *d* of PNIPAM microgel particles with temperature, *T*. Inset shows schematic showing transition of PNIPAM microgel from swollen (hydrophilic) to deswollen (hydrophobic) state. (b) Schematic diagram of the structural change occurring across the volume phase transition for the PNIPAM microgel. (c) Photograph of PNIPAM microgel suspension before and after VPT with respect to temperature, *T*.

Schematic diagram in Fig. 1.4(b) shows the changes observed in the chemical structure of PNIPAM microgel particles below and above VPT. Below VPT, water molecules solvate the polymer chains and forms hydrogen bond with the amide groups. As the temperature increases, the bond between water molecules and amide groups break and water molecules are expelled from the microgel particles. At VPT, most of the water molecules are expelled from the particle resulting in the sudden decrease in the diameter of the particle. Fig. 1.4(c) shows the photograph of PNIPAM microgel suspension below and above VPT. The sample turns turbid above VPT due to increased refractive index of PNIPAM microgel particles leading to increase in multiple scattering.

### 1.4.2 pH responsive behaviour of PNIPAM-co-Aac microgel particles

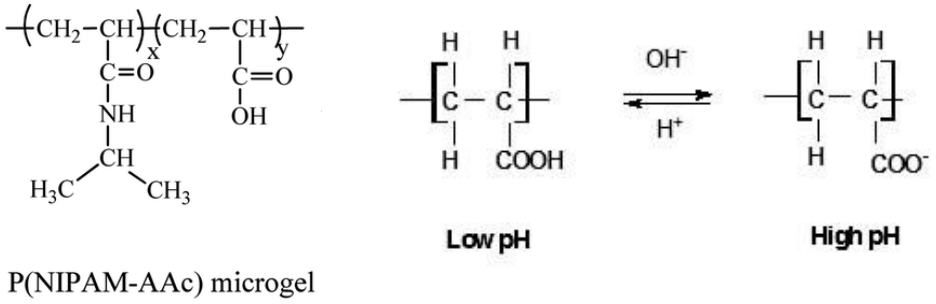


**(a)** **(b)**

**Fig.1.5** (a) Schematic diagram of the chemical structure of PNIPAM-co-Aac microgel particle (b) Protonation and deprotonation of acrylic acid group at low and high pH.

PNIPAM microgel particles functionalized with acrylic acid moieties (Aac) are termed as PNIPAM-co-Aac microgels and respond to pH apart from being thermo responsive [48]. Fig. 1.5(a) shows the chemical structure of PNIPAM-co-Aac microgel particle. Microgel particles swell as the pH of the suspension is increased. The dissociation constant of acrylic acid, $pK_a$ is ~ 4.25. Below $pK_a$, acrylic acid

groups remain protonated, hence the microgel particles remain in the deswollen state. Above $pK_a$, acrylic acid groups deprotonate and residual carboxylate ions remain attached to the polymer chain (Fig. 1.5(b)). As a result, microgel particles as well as polymer chains within the microgel particle acquire charge. Microgel particles swell due to electrostatic repulsion between the polymer chains. At pH 4.25, most of the acrylic acid groups undergo deprotonation resulting in sudden swelling of microgel particle at pH 4.25 is identified as VPT and the pH at which it happens is VPT-pH. This transition is also known as neutral to charged transition of PNIPAM-co-Aac microgels.

### 1.4.3 Core-shell structure of PNIPAM microgel particles

PNIPAM microgel particles consist of roughly about 2-3 % of polymer and the rest is water (solvent) [59]. Microgel particles have network structure due to cross-linked polymer chains and also due to self cross-linking of polymers chains [60,61]. These polymer chains span the entire volume of the particle. PNIPAM microgel particles are soft, porous, compressible and permeable to solvent in nature. Small angle neutron scattering (SANS) studies on the internal structure of PNIPAM microgels as a function of temperature have revealed that microgel particles has core-shell structure (Fig. 1.6(a)) [59,62]. The polymer concentration at the central part of the spherical particles is reported to be almost constant and decreases rapidly towards the periphery (Fig. 1.6 (b)) [63]. SANS showed that microgel particles are core-shell structure with dense core and a thin shell of thickness ~ 20-30 nm [58,59]. The polymer density in the core is found to increase with increase in temperature, *T*. However, the thickness of the shell is found to remain almost constant with increase in temperature [59]. The concentration of the cross-linker (BIS) decides the size of the

core and shell thickness [61]. Increase in cross-linker concentration, the particles morphology is shown to transform from branching chains to a more compact particle.

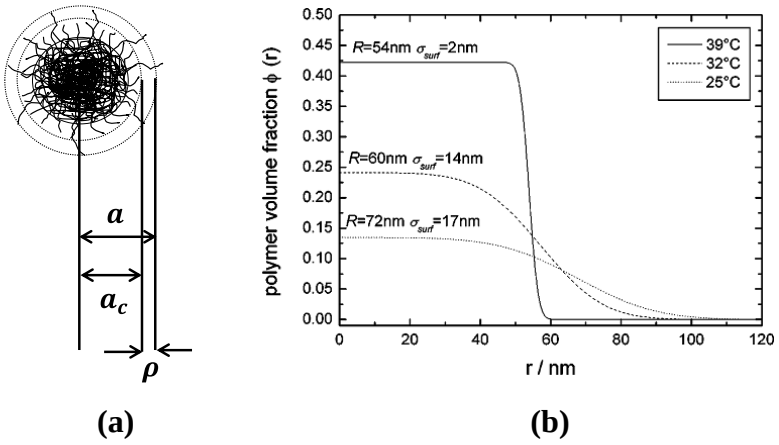


**Fig. 1.6** (a) Schematic of core-shell structure of PNIPAM microgel particle in swollen state, with core of radius $a_c$ and shell of thickness $\rho$. $a = d/2$, is the hydrodynamic radius and (b) Radial polymer density profiles of PNIPAM microgel particle at various temperatures measured using small angle neutron scattering, (Adapted from Stieger *et al*.[62]).

### 1.4.4 Interparticle interaction between neutral and ionic Microgel particles

Neutral thermo-responsive microgel particles are soft and deformable spheres and exhibit deswelling upon increasing the temperature. The size variation and associated increase in polymer content within the microgel particle effect in the interparticle interaction between microgels. In the swollen state (i.e., T << VPT) the van der Waals attraction between neutral microgels (e.g, PNIPAM) is negligible as the microgel contains almost 97% water, hence the Hamaker constant is same as that of solvent (water) [40]. Hence in the swollen state neutral microgel spheres are stable. As de-swelling occurs (while increasing temperature) so the van der Waals forces become increasingly more significant. Thus nature of interaction between microgel particles depends on temperature and exhibit phase behavior different from Hard-sphere suspensions. Further, neutral microgel particles are also known to have dense

polymer core and hairy shell. There have been several propositions for their effective interparticle interaction [41,43,57]. Modelling the microgel particles as hard spheres dressed with additional power-law interactions, Wu *et al*., proposed the following function [57] for the interparticle interaction between PNIPAM thermo-responsive microgels,

$$\frac{u(r)}{k_B T} = \begin{cases} \infty & r < d \\ -\frac{T_0}{T}\left(\frac{d_0}{d}\right)^{6+n}\left(\frac{d}{r}\right)^{n} & r \geq d \end{cases} \qquad (1.6)$$

where $T_0$ is an empirical proportionality constant that has the unit of temperature and $d_0$ is the particle diameter at the reference temperature where the conformation of the network chains is closest to that of unperturbed Gaussian chains. The phase diagram calculated using a thermodynamic perturbation theory combined with light-scattering and spectroscopic measurements is shown in Fig. 1.7 [57]. At low temperature (i.e. below VPT) the phase diagram shows fluid-solid transition spanning over a wide range of particle concentration and a phase separated state (i.e. metastable fluid-fluid transition) at high temperatures (just above VPT). At low T, microgel particles behave like hard spheres as predicted by the theory [57] and experiments as well [64,65]. The phase separation arises due to increased van der walls attraction due particle deswelling.

Brijitta *et. al*.[54], have showen that fluid (liquid-like) to fluid (gas-like) transition happens even below VPT without a significant change in number density across the transition. This suggest the interparticle interactions is repulsive even close to VPT. Further, there is no evidence of aggregation of particles above VPT. These deviations suggest that temperature dependent part of the interaction potential of

microgels needs to be improved considering the core shell nature and inhomogeneous nature of the core to describe the observed phase behaviour of neutral microgels.

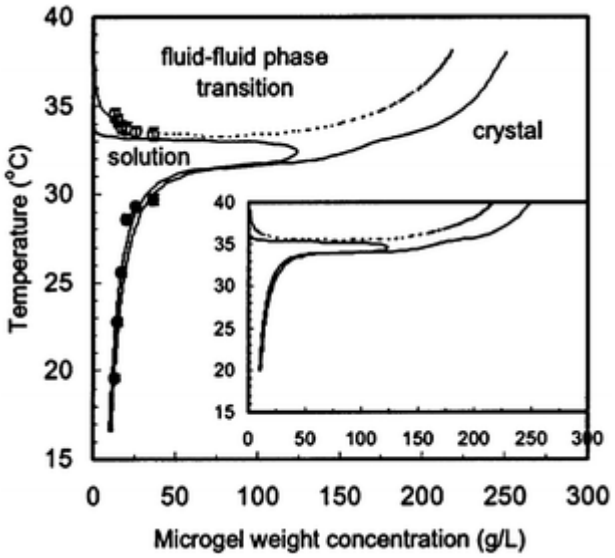


**Figure 1.7** Phase diagram of aqueous PNIPAM microgel particles reported in Ref. [57] determined from turbidity measurements (symbols) and from the thermodynamic perturbation theory with emprical correction to temperature (lines). Inset shows the phase diagram without emperical correction to the temperature.

Gottwald *et al*. [5], have proposed an effective interaction potentials between spherical polyelectrolyte microgels in order to investigate theoretically the structure and phase behavior of ionic microgel solutions. By combining a genetic algorithm with accurate free energy calculations, they obtained phase diagram for ionic microgels consisting of Hexagonal, body-centered orthogonal, and trigonal crystalline strctures being stable at high concentrations and charges of the microgels, accompanied by re-entrant melting behavior and fluid-fcc-bcc transitions below the overlap concentration (Fig. 1.8). Mohnaty and Richtering [3] have investigated pH responsive charged microgels using light scattering and verified the preditions of Gottwald *et. al*. simulations. However, experiements could not prove the predition of re-entrant transition by Gottwald simulations.

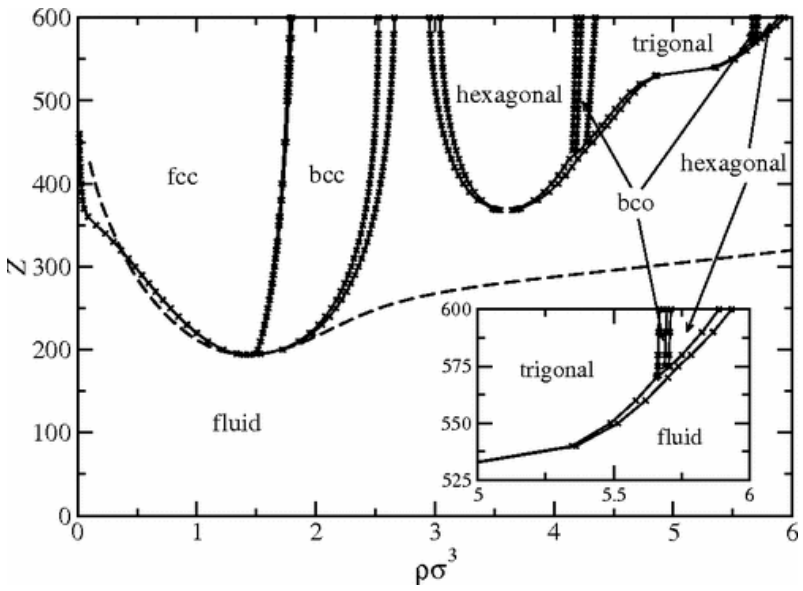


**Figure 1.8** Phase diagram of ionic microgels with diameter $\sigma = 100\ nm$ adopted from [5]. The crosses denote calculated phase boundaries, whereas the lines are guides to the eye. Inset shows the high-density, high charge in detail.

### 1.4.5 Phase behaviour of neutral and ionic microgel suspensions

Since PNIPAM microgel particles in their swollen states has close to 97 % water [59], the refractive index of the particle is closely matched with that of water. Close matching in refractive index of PNPAM microgel particles with that of solvent helps to study dense microgel suspension for their structural ordering and dynamics using light scattering experiments without the problem of multiple scattering of light. PNIPAM microgels are known to exhibit liquid, crystal and glass-like structural ordering under appropriate conditions [54,63,65]. The advantage of stimuli responsive microgel particles over hard spheres or charged colloids is their response to external stimuli like *T*, pH or ionic strength, hence can be used to study the phase behaviour of microgel system. PNIPAM microgel crystals and glasses are shown to melt into liquid-like order upon increasing the temperature [54,57].

PNIPAM microgel particles are soft in nature and their softness have a decisive role in determining the phase behaviour of the microgel system [66]. Soft nature of PNIPAM microgel particles enables them to be compressed due to osmotic pressure. These suspensions can be packed to a volume fraction, $\phi > 0.74$ (cubic close packed limit) which suggest they are soft and deformable [51]. Particle softness can be tweaked by varying the cross-linker concentration. Softness of PNIPAM microgel particle is inversely proportional to the coss linker concentartion [54,67]. The form of inter-particle potential of PNIPAM microgel system with respect to external stimuli is still unknown. The phase behaviour of soft sphere system predicted by assuming an inter-particle potential of the form, $U(r) = (d/r)^n$ has shown that the freezing point shifts to higher volume fraction, $\phi$ with increase in the degree of softness. In addition, the width of liquid-crystal coexistence region decreased compared to that of hard sphere system [68,69]. In PNIPAM microgel suspension, the freezing point was found to be at higher volume fraction than predicted and experimentally observed in case of hard spheres ($\phi_f = 0.494$) [54]. This striking experimental fact suggests that the soft repulsive potential can explain the phase behaviour of PNIPAM microgel suspension at low temperatures, *T*.

### 1.4.6 Structure of PNIPAM and PNIPAM-co-Aac microgel crystals

The structure of PNIPAM microgel crystals is shown to be FCC using scattering techniques [65] and also using confocal laser scanning microscopy (CLSM) [70]. PNIPAM microgel crystals with $\phi = 0.44$ is found to exhibit RHCP structure under as prepared conditions. Recrystallized samples, prepared by raising the temperature of the sample above VPT and then cooling the sample to room temperature at a slower rate, showed FCC structure. Annealing is shown to remove

stacking faults in the sample and change the crystal structure of the sample from RHCP to FCC [70]. The crystal structure was determined by calculating the pair correlation function, *g(r)* in real space using confocal images. Brijitta *et. al*., have identified the stacking sequence and stacking fault probability by analyzing the stacking sequence of consecutive layers. Fig. 1.9 shows the stacking sequence for FCC and HCP structures [70]. PNIPAM microgel crystals with widely different cross-linker densities investigated using SANS also showed FCC structure. Even at low cross-linker density, PNIPAM microgel crystals were found to crystallize much like hard sphere system [65].

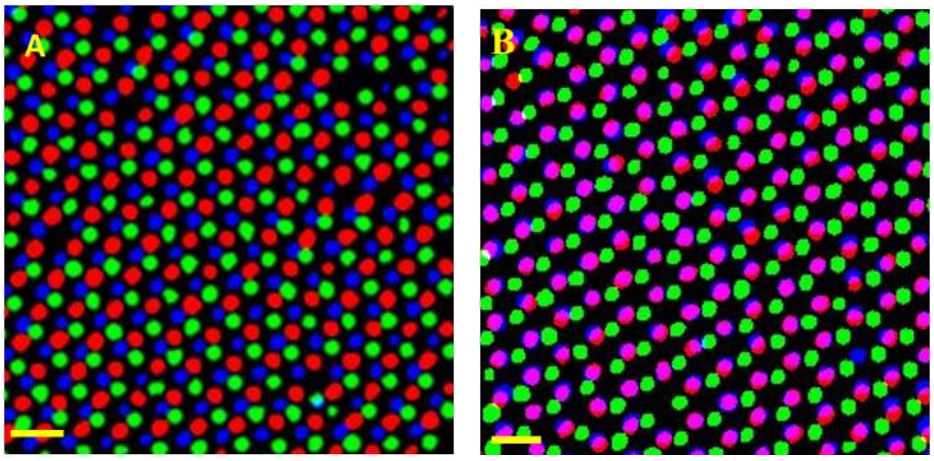


**Fig. 1.9** Micrograph obtained by merging three consecutive layers of PNIPAM colloidal crystal imaged through CLSM. Three psuedocolours Red, Blue, Green were assigned to each layer before merging. Micrographs showing (a) ABC stacking and (b) showing AB stacking. (Adapted from Brijitta *et al*. [70]).

The crystal structure of PNIPAM-co-Aac microgel crystals at volume fraction, $\phi < 0.74$, is reported to be random hexagonal close packed (RHCP) structure which later transformed into FCC structure [3,71], as predicted by theoretical calculations [5,72]. At low concentration fluid-FCC-BCC transition is observed experimentally which is consistent with the literature [3]. At high concentrations and charges of the microgels, hexagonal, body centered orthogonal (BCO) and trigonal structures are

predicted theoretically [5]. Microgel suspensions with volume fraction, $\phi > 0.8$ has been reported to crystallize in RHCP structure through SANS and SAXS studies [73,74].

### 1.4.7 Swelling and de-swelling of neutral and ionic microgel particles

Swelling or de-swelling behaviour of microgels with external stimuli can be described using Flory-Rehnar theory [75]. The equilibrium size of a microgel particle immersed in water (solvent) can be obtained under the condition of osmotic pressure inside and outside the gel to be same. The osmotic pressue has contributions from mixing of polymer and solvent and elastic contributions. From Flory-Rehner theory, osmotic pressure can be written as,

$$\prod_{mix} + \prod_{elastic} = 0 \tag{1.7}$$

where $\prod_{mix}$ accounts for the free energy change due to mixing of polymer and solvent, $\prod_{elastic}$ results from the deformation of the polymer chains inside the microgel particles with respect to their equilibrium contribution. Both contributions depend on the swelling ratio and can be estimated using Flory's theory [42] with corrections incorporated to take into account of inhomogeneities in microgel particles [76],

$$\prod_{mix} = -\frac{N_a k_B T}{v_s}[\Phi + \ln(1-\Phi) + \chi\Phi^2]$$
$$\prod_{elastic} = \frac{N_c k_B T}{V_o}\left[\frac{\Phi}{2\Phi_o} - \left(\frac{\Phi}{\Phi_o}\right)^{1/3}\right] \tag{1.8}$$

where $N_a$ is the Avogadro number, $k_B$ is the Boltzmann constant, $T$ is the absolute temperature, $v_s$ is the molar volume of the solvent, $\chi$ is the Flory polymer-solvent interaction parameter $\Phi$ and $\Phi_o$ are polymer volume fraction within the particle in the

swollen and collapsed states respectively. $V_o = \pi d_o^3/6$ is the volume of the particle in the collapsed state with diameter, $d_o$. For isotropic swelling, the diameter, $d$ and the polymer volume fraction are related by $\frac{\Phi}{\Phi_o} = \left(\frac{d_o}{d}\right)^3$.

In case of ionic microgels, an additional term to describe the osmotic pressure arising due to the charges on the polymer network has to be inclued in Eqn. (1.7) and becomes,

$$\prod_{mix} + \prod_{elastic} + \prod_{ion} = 0 \tag{1.9}$$

where $\prod_{ion} = k_B T \frac{f}{V}$ with $f$ being total number of mobile counterions inside the gel and $V = \pi d^3/6$ is the volume of the particle. For the fullfilment of electroneutrality, the number of mobile counterions inside the gel, $f$ should be equal to the network charge, $q$. The osmotic pressure due to ions can be written as $\prod_{ion} = \Pi_{ion}^{in} - \Pi_{ion}^{out}$ where $\Pi_{ion}^{in}$ is osmotic pressure due to counterions inside the particle and $\Pi_{ion}^{out}$ is osmotic pressure due to the counterions outised the particle. Eqn.(1.8) becomes[77],

$$\prod_{mix} + \prod_{elastic} + \Pi_{ion}^{in} - \Pi_{ion}^{out} = \prod_{total} = 0 \tag{1.10}$$

Microgel particles swell or deswell depending on the sign of $\prod_{net}$. The size of microgel particle is unchanged if $\prod_{net} = 0$. It has been shown by Joshi *et. al.*, in dense PNIPAM microgel suspension of volume fraction, $\phi > 0.74$, the net osmotic pressure experienced by the particle, $\prod_{total}$ is of the order of kPa which is greater than the bulk modulus of PNIPAM microgel particles [78] leading to deswelling of microgel particles. The temperature dependence of swelling/deswelling of microgels is incorporated in Flory parameter, $\chi$ and is defined as [27],

$$\chi = \chi_1 + \chi_2 \Phi$$

where, $\chi_1 = (\Delta H - T\Delta S)/k_B T$ with $\Delta H$ = -12.46 x $10^{-21}$ J and $\Delta S$ = -4.717 x $10^{-23}$ J/K. Here $\Delta H$ is enthalpy change and $\Delta S$ is entropy change per monomeric unit of network related to volume phase transition. $\chi_2$ is the fitting parameter and depends on the cross-linker density.

### 1.5 Immobilization of colloidal crystals

Colloidal crystals grown in aqueous medium are fragile and relatively unstable against shear and hence are not widely used for the fabrication of devices [7,79]. In order to improve the mechanical stability, colloidal crystals have been locked in solid matrix. It is important to immobilize these crystals to retain their periodic arrangement in a matrix to prolong their utility. This has been achieved by introducing polymerizable monomers in colloidal crystals which can form hydrogel network around colloidal spheres. Colloidal crystals immobilized in a solid matrix is known as portable photonic crystals [24]. Immobilization of these crystals in hydrogel matrix have provided mechanical strength needed for colloidal crystals [17]. Hard sphere crystals, charged colloidal crystals and microgel crytals are immobilized and well-studied for their applications [79,80]. Immobilized colloidal crystals have been used for controlled uptake and release of drugs [81,82], Bragg filters [83], tunable photonic crystals [26,84], non-linear optical switches [23,24], chemical sensors [85], etc. Crystals of stimuli responsive microgel particles is known as tunable photonic crystals [52].

### 1.6 Dynamics in colloidal suspensions

Monodisperse colloidal systems, though they mimic atomic systems in structural ordering and phase behaviour, they differ in dynamics due to presence of

solvent. Colloidal particles suspended in a solvent exhibit brownian motion. The motion of the colloidal particles disperesed in a solvent is described by Langevin equation of motion, given as [86],

$$m\frac{dV(t)}{dt} = -\zeta V(t) + F(t) \tag{1.11}$$

Here $V(t)$ is the velocity of the colloidal particle with mass $m$. The frictional force $(-\zeta V(t))$ opposes the motion of the particle and $F(t)$ is a random force. The frictional force is velocity dependent with $\zeta$ being the frictional co-efficient and it slows down the colloidal particle. The motion of colloial particle is overdamped due to viscous drag. For a spherical particle with sticky boundary conditions in newtonian fluid, $\zeta$ is given by the stokes expression, $\zeta = 6\pi\eta_s a$, where $a$ is the radius of the particle and $\eta_s$ being the viscosity of the solvent [87]. The random force, $F(t)$ arises due to the fluctuations in the solvent molecules which accelerate or decelerate the colloidal particle due to collisions. The velocity of colloidal particles in the solvent undergoing brownian was obtained by solving Eqn. 1.11 and given by,

$$V(t) = V(0)\exp\left(-\frac{\zeta}{m}t\right) + \int_0^t d\tau \exp\left(-\frac{\zeta}{m}(t-\tau)\right)F(\tau) \tag{1.12}$$

The velocity correlation function averaged over maxwellian distribution is given by,

$$\langle V(t)V(0)\rangle = \langle V(0)\rangle^2 exp\left(-\frac{\zeta}{m}t\right) = \frac{3k_BT}{m}exp\left(-\frac{\zeta}{m}t\right) \tag{1.13}$$

Since the random force is uncorrelated with the initial velocity, $V(0)$, the correlation term $\langle F(\tau)V(0)\rangle$ is zero and the second term in Eqn. 1.12 vanishes. The displacement of colloidal particles vary for different particle for the given interval of time. Hence to

characterize the motion of the Brownian particle which is randomly moving, mean square displacement (MSD) is the better quantity to characterize the motion. MSD $\langle r^2(t)\rangle$ of colloidal particle was obtained from velocity correlation function using the expression [86],

$$\langle r^2(t)\rangle = 2\int_0^t d\tau\ (t-\tau)\langle V(\tau)V(0)\rangle \tag{1.14}$$

As a consequence of large mass and size difference between colloidal particles and solvent molecules, particles behaviour expressed as an averaged quantity over different time scales is sufficient to understand their dynamics. Towards that, MSD of the particle at three different times scales *viz.*, short time, intermediate time and long-time are used to investigate the dynamics of the colloidal particles. The time to which an impact from solvent molecules to colloidal particles exists is in the range of $10^{-13}$ to $10^{-12}$ s for low viscosity liquids, known as impact time. Any notable change in the momentum of Brownian particle needs numerous collisions with the solvent molecules. The time scale in which the velocity of Brownian particles fluctuates is much longer than the impact time. These time regimes are classified based on two characteristics time scales, i.e., Brownian time ($\tau_B$) and cage rearrangement time ($\tau_R$). $\tau_B = \frac{m}{\zeta}$ is the time required to decouple the momentum of the solvent molecules and colloidal particle. $\tau_R = \frac{a^2}{D_0}$ is the time required for the particle to diffuse over a distance equal to its own diameter, where $a$ is the radius of the particle and $D_0$ is the free diffusion coefficient. The time between $\tau_B \ll t \ll \tau_R$ is termed as short time, $t \approx \tau_R$ as intermediate time and $t \gg \tau_R$ as long time [88]. MSD data as a function of time was analysed for characterizing the particle dynamics and classified to be diffusive ($\alpha = 1$) or sub-diffusive ($\alpha < 1$) [86], by fitting to the power law,

$$\langle r^2(t)\rangle \propto t^{\alpha} \tag{1.15}$$

Here $\alpha$ is the time exponent.

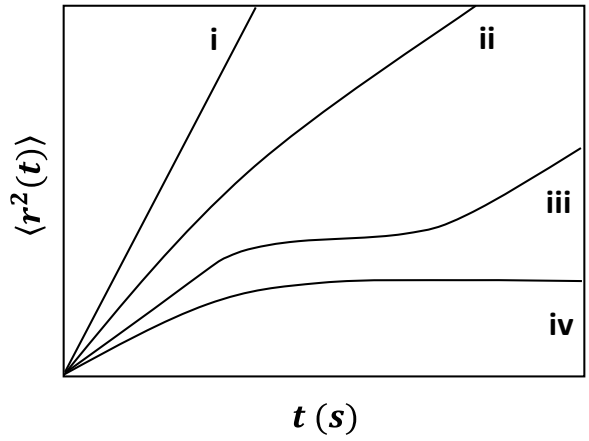


**Fig. 1.10** Schematic showing MSD ($\langle r^2(t)\rangle$) of colloidal particles as a function of time, $t$ in suspension with different structural ordering. Line indicates (i) gas-like, (ii) liquid-like (iii) supercooled liquid and (iv) crystalline or glass-like ordering.

MSD of particles at different particle densities are shown in Fig. 1.10. In dilute condition (gaseous state), colloidal particles exhibit free diffusive motion ($\langle r^2(t)\rangle \propto t$) at all times and characterized by a single diffusion coefficient, $D_0$ (Fig. 1.10(i)). MSD of suspension exhibiting liquid-like ordering is shown in Fig. 1.10(ii). The short time diffusion coefficient, $D_s$ is slower than the free diffusion co-efficient, $D_0$ due to hydrodynamic interactions. At longer times along with hydrodynamic interactions, colloidal particles experiences direct interparticle interaction which slows down the particle and is characterised by long time diffusion coefficient, $D_L$ [89]. The change in the slope of the curve (ii) in Fig. 1.10 indicates the diffusion coefficient has changed from $D_s$ to $D_L$. The MSD of supercooled liquid was altogether different. The particle exhibits diffusive motion at short times whereas it is sub-diffusive ($\langle r^2(t)\rangle \propto t^{\alpha}$, with $\alpha < 1$) at intermediate times due to the cage effect from the neighbouring particles. At long time, motion of the particle has become diffusive as the cage around

the particle changes dynamically (Fig. 1.10 (iii)). In the case of crystal or gas, the long time diffusion coefficient becomes zero while the short time diffusion co-efficent remains to exist (Fig. 1.10(iv)) [15,87].

### 1.7 Motivation for the thesis

Poly (N-isopropyl acrylamide) (PNIPAM) microgel particles are temperature sensitive which show variation in particle size with respect to temperature [54]. Upon increasing the temperature, PNIPAM microgel particles undergo a sudden transition from swollen to collapsed state at around 34 °C, which is known as volume phase transition (VPT), which is reversible. With the incorporation of acrylic acid groups (Aac) during polymerization, PNIPAM-co-Aac microgels also respond to pH and ionic strength in addition to the temperature [90]. These microgel particles are soft, deformable, inhomogeneous (core-shell structured) having densely crosslinked core and a thin shell (~ 20 – 30 nm) which is loosely cross linked and has dangling polymer chains (hairs) [59,62]. In swollen state, PNIPAM microgel particles contain 2-3% of polymer and the rest is water [59]. Hence, they are closely refractive index matched with water (solvent) which makes them ideal for investigating using light scattering technique, as they are free from multiple scattering of light even under dense conditions. Across VPT, microgel suspensions turn turbid due to increase in refractive index of the particle leading to multiple scattering of light. 3D DLS, which employs cross correlation technique, helps in investigating turbid samples for their structural ordering and dynamics. Dense suspensions of monodisperse microgel spheres exhibit structural ordering (liquid-like, crystalline and glass-like) similar to that observed in other colloidal systems as well as in atomic systems [24] which hence serve as a model condensed matter sytem [91].

Applications of microgels in sensors and site specific drug delivery requires accurate determination of VPT of these particles induced by external stimuli. DLS is used to identify the VPT of these microgel particles with respect to either *T*, pH or ionic strength [54,88,92]. Using DLS, hydrodynamic diameter, *d* of these microgel particles is measured as a function of external stimuli and sudden increase or decrease in the particle diameter at a critical value is identified as the VPT of these microgel paticles. The particle diameter is obtained from the DLS measurement using Siegert's relation which in turn requires atleast $10^7$ particles/$cm^3$ for the measurement to satisfy the Gaussian approximation used in the derivation [86]. Polydispersity in microgel particles is inevitable and interpreting DLS data of polydisperse sample is complicated [93]. Since VPT is the property of polymer itself and hence, measurement on a single particle will determine the VPT unambigiously. Towards this, we have developed an alternative tool to investigate VPT using optical tweezers [94]. Using the home built optical tweezers, the VPT of PNIPAM-co-Aac microgel particles with respect to pH was identified using trap stiffness, $\kappa$ as order parameter. Numerical calculation of trap stiffness was used to validate the experimental results.

Microgel particles in suspension with volume fraction greater than random close packed limit are shown to experience deswelling due to the osmotic pressure [77,88]. As the concentration of the microgel suspension was increased, the soft and core-shell nature of PNIPAM microgel particles are expected to affect the structure and dynamics of these microgel system. In this thesis, we have reported the structure of PNIPAM microgel crytals with volume fraction greater than 0.74 using static light scattering and UV-visible spectroscopy. The structure of PNIPAM microgels at a volume fraction greater than 0.74 is found to FCC-HCP coexistence. These microgel crystals are melted by raising the temperature to 35 $^oC$ and slowly cooled at the rate of

0.1 ºC/hour to room temperature to identify their equilibrium structure. The structure of these crystals is found to be FCC-HCP coexistence even after annealing and cooled at slow rate. The sub-diffusive behaviour at short times exhibited by these microgel particles, due to entanglement of dangling polymer chains of neighbouring polymer chains, is argued to be the reason for the stabilization of FCC-HCP coexistence structure.

PNIPAM-co-Aac microgel particles are pH-responsive as well as thermoresponsive [48]. These microgel at pH > 4.25 are ionic in nature. The crystal structure of PNIPAM-co-Aac microgel suspensions prepared at different pH from 3.00 to 5.00, with same number density, $n_p$ is investigated under as prepared and after recrystallization. All the samples under as prepared condition exhibited FCC-HCP coexistence structure. Upon recrystallization, by melting the sample and cooling at the rate of 0.1 ºC/hour to room temperature, the sample at pH 3.40 has crystallized in FCC structure, rest of the samples at other pH values exhibited FCC-HCP coexistence. The entanglement between neighbouring polymer chains is found to be the reason for the observed FCC-HCP coexistence in the samples. The sub-diffusive behaviour at short times exhibited by these particles provides the evidence for the entanglement of dangling polymer chains. PNIPAM-co-Aac microgel particles exhibit the same behaviour as that of neutral PNIPAM microgel particles at volume fraction greater than 0.74.

Colloidal crystals are fragile and highly unstable against even small shear and are limited for device fabrication [7,79]. These microgel crystals are immobilized in hydrogel matrix to provide sufficient mechanical strength and stability against shear [79,95,96]. Immobilization of these microgel crystals in hydrogel is carried out in a

controlled environment with temperature was maintained around 15 ºC, until the polymerization was completed. Though, there are plenty of applications for microgel crystals immobilized in hydrogels, the reports of detailed studies on the structure and dynamics of these crystals before and after immobilization is seldom present. In this thesis we have reported the structure and dynamics of gel immobilized microgel crystals. The temperature response of these immobilized crystal was understood in terms of particle size, particle form factor and refractive index of the particle.

Towards all the above mentioned studies, nearly monodisperse PNIPAM and PNIPAM-co-Aac microgel particles of different size have been synthesized. At higher temperatures PNIPAM microgel suspension turns turbid due to multiple scattering of light [97]. Investigations at high temperatures have been carried out using 3D DLS technique which uses cross-correlation method to pick-up single scattered light in the presence of multiple scattering. The thesis is organized as follows. The details of synthesis of microgel particle and their characterization and also the details of home built optical tweezers set-up are discussed in Chapter 2. Chapter 3 reports the identification of VPT of a single microgel particle using optical tweezers. Numerical calculations to understand optical tweezers data is also presented. Chapter 4 reports the crystal structure of thermo responsive PNIPAM microgel crystals with volume fraction greater than 0.74 using SLS and UV-visible spectroscopy. The crystal structure of pH responsive PNIPAM-co-Aac microgel crystals as a function of pH with volume fraction greater than 0.74 is presented in chapter 5. Chapter 6 reports the immobilization of microgel crystals in PAAm hydrogel and their structure and dynamics using light scattering techniques. Chapter 7 discusses the summary and conclusions of the investigations carried out using Optical tweezers, SLS, DLS and

UV-Vis spectroscopy, important findings of the thesis and directions for the future work.

### 1.8 Key findings of the thesis

i. Indigenously designed and developed an optical tweezers set-up. Using which for the first time, we have shown that VPT can be identified on a single microgel particle and shown that it gives a sharp transition as compared to that of conventional method of identifying VPT using DLS. VPT manifests as a sudden jump in the trap stiffness and is understood to arise from sudden decrease in the particle size with concomitant increase in the refractive index of the particle.

ii. For the first time FCC-HCP coexistence is shown to be the stable state for dense PNIPAM microgel crystals with volume fraction, $\phi > 0.74\phi > 0.74$ by performing detailed annealing studies. It is also shown that PNIPAM microgel crystals with volume fractions, $\phi < 0.74\phi < 0.74$ crystallize into FCC structure. Entanglement of dangling polymer chains between shells of neighboring microgel spheres is shown to occur in PNIPAM microgel crystals with$\phi > 0.74$, $\phi > 0.74$ and is evidenced by observing sub-diffusive behavior at short times. The entanglement is shown to disappear upon heating the crystals well about their melting temperature.

iii. Through detailed annealing studies, it is shown that overlap of dangling polymer chains between the shells of neighbouring spheres is responsible for the stability of FCC-HCP coexistence observed in microgel crystals with $\phi > 0.74$.

iv. In dense pH responsive microgel crystals, as prepared samples in the pH range 3.00 to 5.00 crystallized in FCC-HCP coexisting structure. At pH = 3.40 ($\phi \approx 0.5$), the sample upon recrystallization was found to crystallize into FCC structure whereas the samples at other pH (3.7, 4.0, 4.35, 4.7, 5.0) with $\phi > 0.74$ has remained in the FCC-HCP state. Dynamics of PNIPAM-co-Aac microgel particles at short times in dense suspensions is found to be diffusive in sample with $\phi < 0.74$ and is sub-diffusive in sample with $\phi > 0.74$. The phase behaviour of ionic microgel crystals with $\phi > 0.74$ was found to be similar to that of dense microgel crystals of uncharged PNIPAM spheres. Our results suggested that Coulombic interaction between PNIPAM-co-Aac microgel particles is not dominant under dense conditions and does not play a major role in stabilizing the crystal structure.

v. Stimuli responsive PNIPAM-co-Aac microgel crystals are successfully immobilized in poly-acrylamide hydrogel (PAAm) matrix. The structure of stimuli responsive microgel crystal is shown to remain unaltered before and after the immobilization. Immobilization of microgel crystals is shown to extend the stability of microgel crystals against melting beyond VPT. Bragg peak intensity as a function of temperature from immobilized microgel crystals is found to vary non-monotonically. That non-monotonic behaviour is shown to arise from the simultaneous decrease of particle diameter with concomitant increase in the refractive index of the microgel particle with increasing temperature.

# CHAPTER 2

# SAMPLE SYNTHESIS AND EXPERIMENTAL TECHNIQUES

This chapter deals with synthesis of PNIPAM microgels in aqueous medium through free radical precipitation polymerization and characterization of these suspensions for their average particle size, size polydispersity, effective surface charge and structural ordering. Initial part of the chapter discusses details about the chemicals used and experimental conditions maintained during the synthesis of PNIPAM microgel particles. Later part of the chapter describes experimental techniques that have been employed to investigate the particle size and size polydispersity, volume phase transition (VPT) of synthesized particles. Static and Dynamic light scattering (DLS) have been used to study particle size, size polydispersity, VPT and dynamics of microgel particles. A home built optical tweezers (OT) has been used to identify the VPT of a single microgel particle. UV-visible spectroscopy technique has been employed to record the Bragg diffraction pattern and dynamics in dense microgel crystals is investigated using 3D- DLS.

## 2.1 Synthesis of thermo-responsive and pH-responsive microgel particles

Poly (N-isopropyl acrylamide) (PNIPAM) microgel particles are synthesized by free radical precipitation polymerization of N-isopropyl acrylamide (NIPAM) monomer with cross linker N, N'-Methelenebisacrylamide (BIS), surfactant sodium dodecyl sulfate (SDS) and initiator potassium persulfate (KPS) [3,54,70,75]. For synthesizing Poly (N-isopropyl acrylamide)-co-acrylic acid (PNIPAM-co-Aac) microgel particles, acrylic acid (Aac) co-monomer is added to the solution before initiating the polymerization. All chemicals used in the synthesis are of analytical

grade reagents and used as supplied. NIPAM, Aac, SDS and BIS are dissolved in Millipore water (resistivity 18.2 MΩ-cm) and the solution is filtered to remove any particulate and dust using 0.1 μm syringe filter (Milex). Filtered solution is transferred to a round bottom flask and purged with argon gas to remove any dissolved oxygen for one hour under rigorous stirring at 70°C. In aqueous solution, above critical micelle concentration (CMC), SDS forms spherical micelles which contain monomer units and act as monomer droplets. The size of the microgel particles is tuned by varying the concentration of surfactant. Variation of SDS amount leads to the variation of size of micelle formed and hence that of microgel particle. The initiator (KPS) is dissolved separately in Millipore water and added to the solution in the round bottom flask shown in Fig. 2.1. KPS dissociates at 70 °C to give free radicals which initiates the polymerization reaction. Beyond a critical chain length, the growing chain collapses to form unstable precursor particles. The precursor particles grow by adding onto other precursor particles. During the polymerization process, BIS cross links polymer chains creating network structure in a microgel particle. Polymerization is allowed to continue for 6 hours while maintaining the temperature of the solution at 70 ± 0.5 °C. Throughout the polymerization reaction argon gas was purged continuously and rigorously by stirring the solution. The solution is cooled down to room temperature after 6 hours to terminate the polymerization reaction. In the absence of the SDS, monomers themselves form droplets. On the other hand, increase in cross linker concentration makes polymer network more compact, resulting in decrease in the size of the particles. At higher concentration of cross linker, due to compaction of polymer network, PNIPAM microgel particles become more rigid than those formed under

lesser cross linker concentration. In the absence of the cross linker, polymer chains forms network structure via self-cross linking.

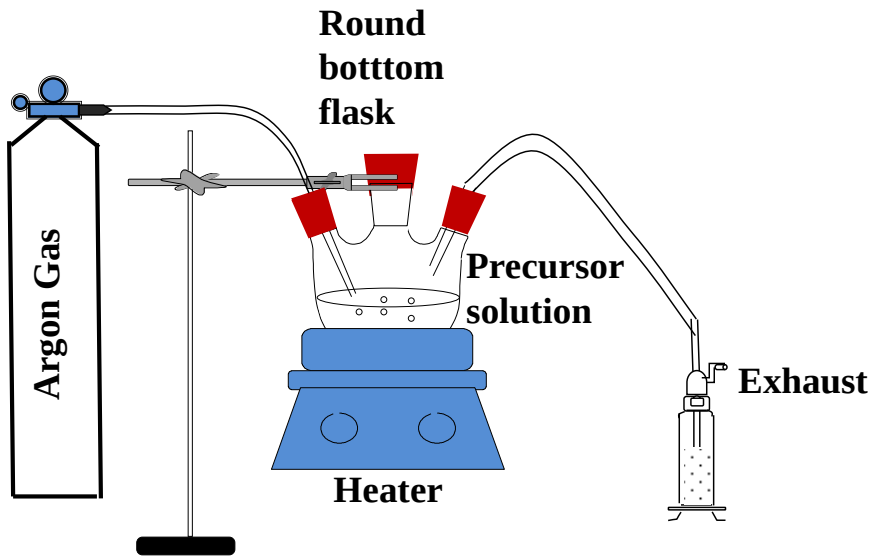


**Figure 2.1** Schematic diagram of the experimental set-up used for synthesizing the PNIPAM microgel particles.

Monodisperse PNIPAM microgel particles of various sizes have been synthesized by varying SDS and BIS. Chemical compositions used for synthesis of microgel particles with different diameters, *d* and size polydispersity, SPD are summarized in Table 2.1.

**Table 2.1** Concentration of chemicals used in the synthesis of PNIPAM and PNIPAM-co-Aac microgels and the mean diameter, *d* and size polydispersity (SPD) of microgel particles measured at 22 °C, using DLS technique.

| **Label** | **NIPAM (mM)** | **BIS (mM)** | **SDS (mM)** | **Acrylic acid (mM)** | **KPS (mM)** | **Diameter, *d* at (22 °C) (nm)** | **SPD (%)** |
|---|---|---|---|---|---|---|---|
| **P1** | 139 | 1.96 | 1.05 | - | 2.22 | 235 | 4.5 |
| **P2** | 139 | 1.96 | - | - | 2.22 | 633 | 8.0 |
| **P3** | 103 | 1.6 | - | 9.25 | 2.22 | 930 | 4.0 |
| **P4** | 103 | 1.6 | - | 18.5 | 2.22 | 1100 | 5.5 |

## 2.2 Purification of PNIPAM and PNIPAM-co-Aac microgel particles

Synthesized PNIPAM microgel suspensions are purified for unreacted monomers and other ionic impurities by dialysis using cellulose tubing's (Himedia, India) with molecular weight cut off 10,000 g/mol against Millipore water (resistivity 18.2 MΩ-cm) for 2 weeks till the dialyze water conductivity goes below 1 µS/cm. After the dialysis, purified microgel suspensions are concentrated by ultrafiltration technique (Fig. 2.2) using a stirred cell equipped with Amicon regenerated cellulose membrane (Millipore, MA, USA) with nominal molecular weight limit (NMWL) 10,000 kDa. Further purification for removing ionic impurities was carried out by keeping the microgel suspensions with mixed bed of ion-exchange resins (Ag501-X8, Bio-Rad laboratories, USA).

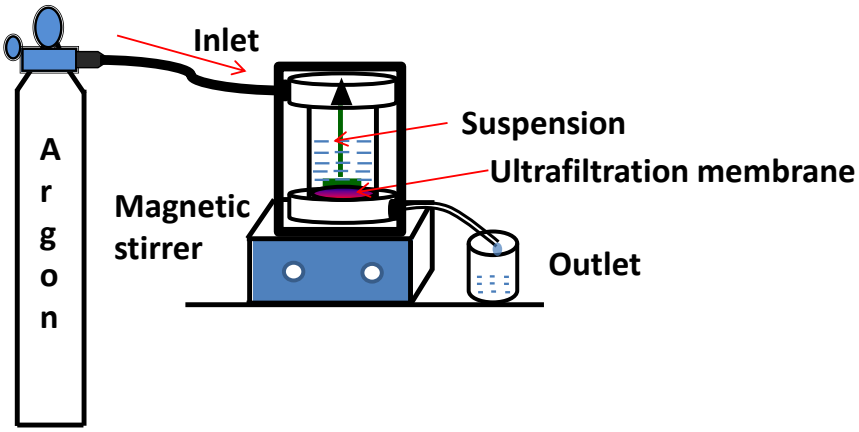


**Figure 2.2** Schematic of stirred cell used for purification/concentration of the microgel suspension using ultrafiltration membrane.

## 2.3 Determination of surface charge density on PNIPAM -co-Aac microgel particles

PNIPAM microgel particles acquire charge from the initiator used during polymerization reaction and due to the addition of ionic co-monomer in the case of ionic microgels. The surface charge density on the PNIPAM-co-Aac microgel

particles suspension is determined by conductivity method [43,98]. Deionized suspensions of PNIPAM-co-Aac particles of known particle number density, $n_p$ was prepared by diluting the concentrated suspension with deionised water whose conductivity is ~ 0.6 μS/cm. The conductivity, $\sigma$ of microgel suspension as a function number density, $n_p$ is measured using conductivity meter. The conductivity of suspension at each concentration is measured using bench pH/Conductivity meter (PC 510, M/s EUTECH INSTURMENTS).

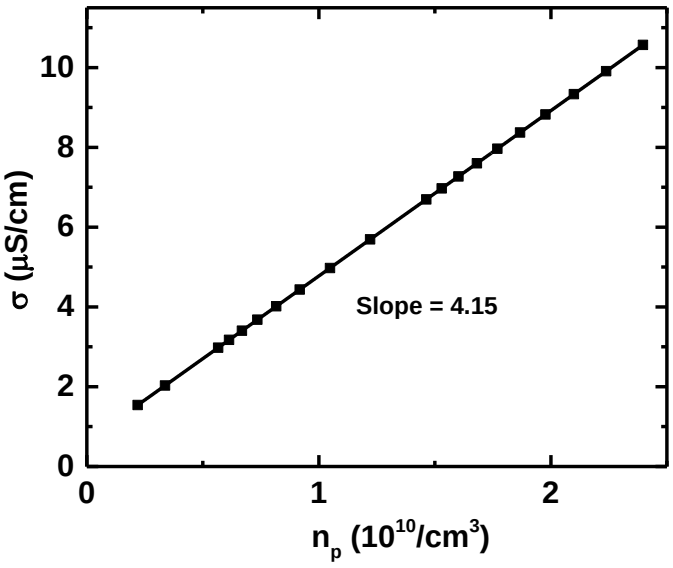


**Figure 2.3** Conductivity, $\sigma$ of microgel suspension as a function of particle number density, $n_p$ for 930 nm PNIPAM-co-Aac microgel particles. Continuous line is linear fit to the data.

Conductivity, $\sigma$ of the microgel suspension varied linearly with $n_p$. Conductivity as a function of number density, $n_p$ is fitted with a linear fit. The slope of the fit is used to calculate surface charge density of the particle and the intercept gives the conductivity of the Millipore water used for diluting of the microgel suspension. Fig. 2.3 shows the plot of $n_p$ verses conductivity for the 930 nm PNIPAM-co-Aac microgel suspension.

The effective charge density, $\sigma_e$ is obtained using the expression,

$$\sigma_e = \text{Slope} \times \frac{N_A}{\lambda_{H^+}} \times \frac{4e}{\pi d^2} \quad (2.1)$$

where $N_A$is Avagardo number, $\lambda_{H^+}$ is the equivalent conductance of $H^+$ at infinite dilution (=349.8 S/cm$^2$ at 25 $^o$C), $e$ is charge of an electron and $d$ is the diameter of the particle. $H^+$ions contributes to the conductivity in deionized suspension. Table 2.2 shows the surface charge densities determined by conductivity method for the PNIPAM-co-Aac suspensions.

**Table 2.2** Effective surface charge densities on the PNIPAM-co-Aac microgel particles.

| **Label** | **Diameter (nm)** | **Effective Surface Charge Density ($\rho$) (μC/cm$^2$)** |
|---|---|---|
| **P3** | 930 | 12.01 |
| **P4** | 1100 | 11.95 |

## 2.4 Preparation of pH buffers

Buffers are prepared by selecting buffering ion with a suitable disassociation constant ($pK_a$) value such that it lies within the range ±1of desired pH value. To start with, 90 ml solution of weak acid (citric acid or acetic acid) is titrated against 100 mM of sodium hydroxide (NaOH) (strong base) to obtain specific pH values. pH values of all the buffer solutions are confirmed by measuring pH many times over a period of 2 days at constant temperature. Those values are used in the estimation of error in pH values. The ionic strength of all the pH buffers is maintained constant at 15 mM, by adding required amount of NaCl, in order to avoid deswelling of microgels due to variation in ionic strength [99] and the uncertainty in the

measurement of pH is ± 0.03. Ionic strength ($I$) of each buffer is calculated using the expression,

$$I = \frac{1}{2}\sum concentration \times no.of\ ions \times (charge\ of\ the\ ion)^2 \qquad (2.2)$$

The conductivity of the buffer solution is measured using conductivity meter and is used in the calculation of ionic strength, ($I$) using the expression

$$I = Russel\ factor\ for\ electrolytes \times conductivity\ (\mu S/cm) \qquad (2.3)$$

Russel factor for electrolytes is 1.6 X $10^{-5}$. The pH value of each buffer is measured using bench pH/Conductivity meter (PC 510, M/s EUTECH INSTURMENTS). The chemicals used in the preparation of pH buffer solutions are listed in Table 2.3.

**Table 2.3** Details of chemical ingredients used in the preparation of pH buffers at an ionic strength of 15 mM.

| pH value | Acidic component | Vol. of 10 mM acid component | Vol. of 100 mM NaOH | Amount of NaCl (g) |
|---|---|---|---|---|
| 3.00 | Citric acid monohydrate | 90 ml | 7.0 ml | 0.061 |
| 3.25 | Citric acid monohydrate | 90 ml | 9.5 ml | 0.053 |
| 3.50 | Citric acid monohydrate | 90 ml | 10.5 ml | 0.045 |
| 3.75 | Citric acid monohydrate | 90 ml | 14.0 ml | 0.039 |
| 3.90 | Citric acid monohydrate | 90 ml | 15.5 ml | 0.03 |
| 4.0 | Acetic acid | 90 ml | 4.4 ml | 0.078 |
| 4.10 | Acetic acid | 90 ml | 5.0 ml | 0.075 |
| 4.20 | Acetic acid | 90 ml | 6.2 ml | 0.072 |
| 4.35 | Acetic acid | 90 ml | 9.0 ml | 0.065 |
| 4.70 | Acetic acid | 90 ml | 11.0 ml | 0.057 |
| 5.00 | Acetic acid | 90 ml | 11.6 ml | 0.48 |

## 2.5 Experimental techniques

### 2.5.1 Light scattering technique

Static light scattering (SLS) and dynamic light scattering (DLS) are two branches of light scattering techniques, which are complementary in the sense that they take advantage of two different and completely independent features of scattered light. SLS utilizes average intensity of scattered light at different angles to obtain molecular weight, particle size, particle shape and interactions. DLS uses the temporal

fluctuations of scattered light at a given angle to derive information like diffusion co-efficient of the particle, etc. [8].

**a) Dynamic light scattering**

The synthesized PNIPAM microgel suspension was characterized for its size and polydispersity using dynamic light scattering (DLS) technique and it is also known as quasi elastic light scattering (QELS) or photon correlation spectroscopy (PCS). DLS is a well-known technique for characterization of sub-micron sized particles or macromolecules. Colloidal particles in a suspension exhibit random motion which includes translational, rotational motion due to non-compensated momentum transfer from the solvent molecules upon collision. Because of this, the light scattered by these particles fluctuates in time around an average value. These fluctuations carry information regarding ordering and dynamics of the particles. Time averaged correlation function offers concise way of obtaining physically meaningful information from these fluctuations which resemble a noise-like signal.

Any physical property, $A(t)$ fluctuating in time, can have two different values at times $t$ and $t+\tau$ if $\tau$ (time lag) is large. For very small values of $\tau$, $A(t+\tau) \approx A(t)$. As the value of $\tau$ increases, the deviation of $A(t+\tau)$ from $A(t)$ increases. In other words, at short $\tau$, $A(t+\tau)$ and $A(t)$ are correlated and this correlation is lost as $\tau$ becomes large compared with the period of the fluctuations. A measure of this correlation is the auto-correlation function of the physical property, $A$ and is defined as [8,100],

$$\langle A(0)A(\tau)\rangle = \lim_{L\to\infty}\frac{1}{L}\int_0^L dt\, A\,(t)A(t+\tau) \tag{2.4}$$

with the assumption that the infinite time average is independent of the starting time. And the average of the physical property, $A(t)$ is

$$\langle A\rangle = \lim_{L\to\infty}\frac{1}{L}\int_0^L dt\, A(t) \tag{2.5}$$

These equations are written in discrete form as

$$\langle A(0)A(\tau)\rangle = \lim_{n\to\infty}\frac{1}{n}\sum_{k=1}^{n} A_k A_{k+m} \tag{2.6}$$

with the average of the property is given as

$$\langle A\rangle = \lim_{n\to\infty}\frac{1}{n}\sum_{k=1}^{N} A_k \tag{2.7}$$

where $A_k$ is the value of the property at the $k^{th}$ interval and $L = N\Delta t$, $t = k\Delta t$ and $\tau = m\Delta t$. The auto correlation function varies as a function of time and it can be shown that it decays from a maximum value of $\langle A^2\rangle$ to a minimum value of $\langle A\rangle^2$ and this variation, in many cases, is single exponential decay in nature and is given by,

$$\langle A(0)A(\tau)\rangle = \langle A\rangle^2 + \{\langle A^2\rangle - \langle A\rangle^2\}\exp\left(\frac{-\tau}{\tau_c}\right) \tag{2.8}$$

where $\tau_c$ is the characteristic decay time of the property, also known as "relaxation time" or "correlation time". Working with auto correlation function of fluctuations in $A$ is much simpler than working with auto correlation function of $A$ itself, as the time invariant part $\langle A\rangle^2$ is discarded in the former case and is given by,

$$\langle \delta A(0)\delta A(\tau)\rangle = \langle \delta A^2\rangle \exp\left(\frac{-\tau}{\tau_c}\right) \quad (2.9)$$

In laser light scattering experiments, a laser beam is focused onto a region of a fluid and is scattered into a detector. From each scattering centres light gets scattered and the superposition of all these scattered light is denoted as the instantaneous scattered field. The scattered electric field at a given scattering wave vector, $q = \frac{4\pi\mu_m}{\lambda} sin\frac{\theta}{2}$ is given by $E_s(q,t)$, where $\mu_m$ is the refractive index of the medium, $\lambda$ is the wavelength of incident light and $\theta$ is the scattering angle The intensity of the scattered electric field detected by the detector at any instance is $I_s(q,t) \propto |E_s(q,t)|^2$ and is fed to a digital correlator for calculating intensity auto correlation function (homodyne correlation function) which is defined as

$$\langle I_s(q,0)I_s(q,t)\rangle = B\langle |E_s(q,0)|^2 |E_s(q,t)|^2\rangle \quad (2.16)$$

where *B* is the proportionality constant and the normalized intensity auto correlation function $g^{(2)}(q,t)$ is defined as

$$g^{(2)}(q,t) = \frac{\langle I_s(q,0)I_s(q,t)\rangle}{\langle I_s(q)\rangle^2} \quad (2.11)$$

and the normalized electric field auto correlation function $g^{(1)}(q,t)$ or $f(q,t)$ is defined as

$$g^{(1)}(q,t) = f(q,t) = \frac{\langle E_s(q,0)E_s(q,t)\rangle}{\langle E_s(q)\rangle^2} \quad (2.12)$$

Normalized intensity auto correlation function, $\left(g^{(2)}(q,t)\right)$ and normalized electric field auto correlation function, $\left(g^{(1)}(q,t)\right)$ is related through Siegert's relations given by [86],

$$g^{(2)}(q,t) = 1 + \beta\left|g^{(1)}(q,t)\right|^2 \tag{2.13}$$

with the following assumptions:

1. Particle motions in the suspension are stochastically independent.
2. The amplitude of the scattered electric field is a Gaussian distribution.

here $\beta$ is the coherence factor and ideally equal to 1. $\beta$ value depends on the size of the aperture placed before the detector. Any deviation in aperture size lead to decrease in the value of $\beta$. In order to maintain the $\beta$ value close to 1, the aperture size is generally chosen as 100 μm or less, the beam exactly focuses at the centre of the scattering volume and the power of the laser is maintained at a constant value.

Upon assuming the instantaneous displacement of colloidal particle, $\vec{r}(t)$ is Gaussian distributed, $f(q,t)$ can be related to mean square displacement (MSD), $\langle r^2(t)\rangle$ through the relation,

$$f(q,t) = \exp\left(-\frac{q^2\langle r^2(t)\rangle}{6}\right) \tag{2.14}$$

MSD obtained using this relation is used to characterize the dynamics of colloidal suspensions. In dilute, non-interacting suspension, a colloidal particle diffuses freely due to Brownian motion with a free diffusion co-efficient $D_0$ and it is related to MSD by the relation, $\langle r^2(t)\rangle = 6D_0t$. Then eqn. 2.14 becomes,

$$f(q,t) = \exp(-q^2D_0t) = \exp(-\Gamma t) \tag{2.15}$$

where $\Gamma = q^2D_0$ is the decay constant. $D_0$ is related to the hydrodynamic diameter, $d$ through Stokes-Einstein relation by $d = k_BT/3\pi\eta D_0$ where $k_B$ is Boltzmann

constant, $T$ is temperature and $\eta$ is the viscosity of the solvent. For suspension with polydispersity, $f(q,t)$ is related to line width distribution, $G(\Gamma)$ by

$$f(q,t) = \int_0^\infty G(\Gamma)\exp(-\Gamma t)\ d\Gamma \tag{2.16}$$

$G(\Gamma)$ can be calculated by Laplace inverse of $f(q,t)$ and the particle size distribution can be derived from it. Deriving precise functional form of $G(\Gamma)$ is rigorous and time consuming. Alternatively, cumulant expansion method is used to obtain the basic information about size and size polydispersity of the suspension from $f(q,t)$. In method of cumulants, $\ln[f(q,t)]$ is expanded in power series expansion as [93],

$$\ln[f(q,t)] = -\bar{\Gamma}t + \frac{k_2}{2!}t^2 - \frac{k_3}{3!}t^3 + \cdots, \tag{2.17}$$

here, $\bar{\Gamma}$ is the average decay rate related to average diffusion constant, $\bar{D}$ by $\bar{\Gamma} = \bar{D}q^2$ and is used to determine the average size of colloidal particles using Stokes-Einstein equation. The size polydispersity (SPD) is obtained using second cumulant, $k_2$ using the expression $SPD = \frac{\sqrt{k_2}}{\bar{\Gamma}}$

MSD data as a function of time, determined using Eqn. (2.14) can be fitted to power law [86],

$$\langle r^2(t)\rangle \propto t^\alpha \tag{2.18}$$

Here, *t* is time and $\alpha$ is the time exponent. If $\alpha = 1$, the particle dynamics is said to be diffusive and $\alpha < 1$, the dynamics is sub-diffusive. If $\alpha > 1$, then the dynamics is termed as super-diffusive [86]. In dense suspensions, multiple scattering of light [101] poses formidable problem in obtaining particle dynamics. The use of 3D DLS

technique which employs cross-correlation technology helps in measuring $g^{(2)}(q,t)$ of single scattered light even in turbid suspension. The 3D DLS set-up has the provision for reducing the path length [102], thus minimizing the multiple scattering of light in the samples which are too turbid.

**b) Static light scattering**

The structural ordering in dense suspensions is characterized using static light scattering (SLS). Since the interparticle separation in colloidal suspensions is of the order of the wavelength of visible light, static light scattering technique is the appropriate tool to characterize the structural ordering in colloidal suspension. Light incident on colloidal suspension is scattered in all directions by the density fluctuations in the scattering volume of the sample. Scattering volume, $V_s$ is defined as the volume at the intersection of the detector cross-section and the incident beam (Fig. 2.4). The detector position which makes an angle with the incident beam defines the scattering angle, $\theta$. In SLS, the elastically scattered light is collected at different scattering angles for a specific time (~ 10 sec). The change in momentum of the photon is given as,

$$\hbar\vec{q} = \hbar\vec{k}_i - \hbar\vec{k}_s \tag{2.19}$$

where $\hbar = h/2\pi$ and $h$ is Planck's constant. $\vec{k}_i$ is wave vector of incident light, $\vec{k}_s$ is wave vector of scattered light and $\vec{q} = \vec{k}_i - \vec{k}_s$ is known as scattering wave vector (Fig. 2.4). For elastic scattering process $|\vec{k}_i| = |\vec{k}_s|$, and the amplitude of scattering wave vector is given by,

$$q = \frac{4\pi\mu_m}{\lambda} sin\frac{\theta}{2} \tag{2.20}$$

Here, $\mu_m$ is refractive index of the solvent and $\lambda$ is wavelength of the incident light.

For a suspension containing $N$ monodisperse colloidal particles of radius, $a$ having refractive index, $\mu_p$ dispersed in the scattering volume, $V_s$, the scattered electric field, $E_S(\vec{q}, t)$, is given by [100],

$$E_S(\vec{q}, t) \propto \sum_{j=1}^{N} \sum_{\alpha_j}^{n} f \exp\left(i\vec{q}.\vec{r}_{j,\alpha_j}(t)\right) \tag{2.21}$$

where $n$ is the number of scattering centres in a colloidal particle with a scattering amplitude of $f$ for each scattering centre, $\vec{r}_{j,\alpha_j}(t)$ is the position vector of the scattering center with respect to an arbitrary origin, $O$, $\alpha_j$ in the $j^{th}$ particle at time, $t$ and can be expressed as

$$\vec{r}_{j,\alpha_j}(t) = \vec{R}_j(t) + \vec{b}_{\alpha_j}(t) \tag{2.22}$$

where $\vec{R}_j(t)$ is the position vector of center of mass of particle $j$ with respect to origin $O$ and $\vec{b}_{\alpha_j}(t)$ is the position vector of scattering center with respect to the center of mass of the particle $j$ at time $t$ (Fig. 2.5). The time averaged scattered intensity, $\langle I(\vec{q})\rangle$ is given by,

$$\langle I(q)\rangle = \langle |E_s(\vec{q})|^2\rangle = Af^2 \langle \sum_{j,k,\alpha_j,\beta_k} \exp\left[i\vec{q}.\left(\vec{r}_{j,\alpha_j} - \vec{r}_{k,\beta_k}\right)\right]\rangle \tag{2.23}$$

Upon substituting equation (2.22) in equation (2.23) and rearranging yields,

$$\langle I(q)\rangle = Af^2\langle \sum_{j,k,\alpha_j,\beta_k} \exp\left[i\vec{q}.\left(\vec{R}_j - \vec{R}_k\right)\right].\exp\left[i\vec{q}.\left(\vec{b}_{\alpha_j} - \vec{b}_{\beta_k}\right)\right]\rangle \quad (2.24)$$

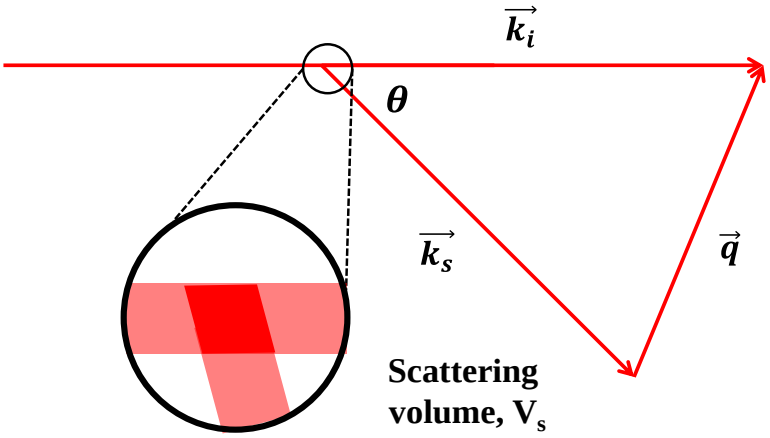


**Figure 2.4** The geometrical representation of scattering wave vector, $\vec{q}$ with respect to incident wave vector, $\overrightarrow{k_i}$ and scattered wave vector, $\overrightarrow{k_s}$ with scattering angle, $\theta$.

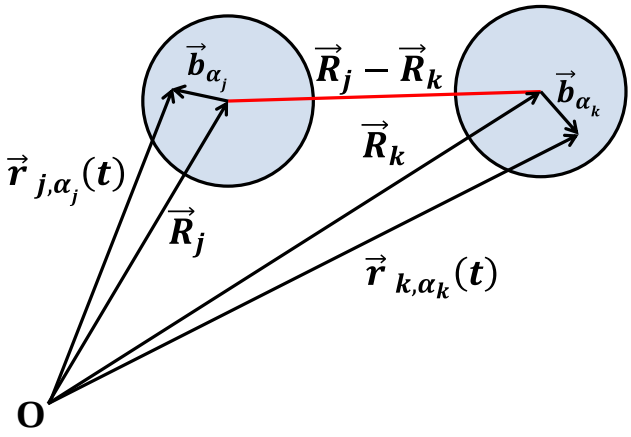


**Figure 2.5** Two spheres having position vector of centre of mass at $\vec{R}_j$ and $\vec{R}_k$ with respect to origin, O and separated by a distance, $\vec{R}_j - \vec{R}_k$. $\vec{r}_{j,\alpha_j}$ and $\vec{b}_{\alpha_j}$ are the distances of the $\alpha^{th}$ scatterer from O and center of the $j^{th}$ sphere, respectively.

Under Rayleigh-Gans-Debye (RGD) approximation, the interparticle contributions and intraparticle contributions to the scattered intensity are separated and written as [37,103],

$$\langle I(q)\rangle = AP(q)S(q) \tag{2.25}$$

where $A = \frac{16\,\pi^4 N a^6}{\lambda^4}\left(\frac{\mu^2-1}{\mu^2+2}\right)^2 \frac{I_0}{L^2}$ is due to Rayleigh scattering from $N$ particles of size $a$ dispersed in a medium of refractive index $\mu_m$, relative refractive index, $\mu = \frac{\mu_p}{\mu_m}$, refractive index of the particle, $\mu_p$ $I_0$ is the intensity of incident radiation of wavelength, $\lambda$. $L$ is the distance between the sample and the detector. $P(q)$ is the particle form factor or intra-particle structure factor and is given by

$$P(q) = \langle \frac{1}{n^2} \sum_{\alpha_j,\beta_k}^{n} \exp\left(i\vec{q}.\left(\vec{b}_{\alpha_j} - \vec{b}_{\beta_k}\right)\right)\rangle \tag{2.26}$$

and for a homogeneous spherical particle of radius, $a$ the particle form factor is given by [104],

$$P(q) = \left\{\frac{3[\sin(qa) - (qa)\cos(qa)]}{(qa)^3}\right\}^2 \tag{2.27}$$

The interparticle structure factor, $S(q)$ is given by,

$$S(q) = \frac{1}{N}\langle \sum_{i,j} \exp\left[i\vec{q}.\left(\vec{R}_i - \vec{R}_j\right)\right]\rangle \tag{2.28}$$

For a dilute suspension, $S(q) = 1$. In order to characterize structural ordering in microgel suspensions, SLS has been used to measure the scattered intensity $I_s(q)$ as a function of $q$. The recorded diffraction pattern is analysed to identify the crystal

structure of PNIPAM microgel crystals which are known to exhibit face centred cubic (FCC) or hexagonal close packed (HCP) or random hexagonal close packed (RHCP) structure [70]. For an FCC structure, the first Bragg peak in the diffraction pattern is from (111) planes. Other allowed Bragg peak positions for FCC structure have been calculated using the position of $q_{111}$ peak and using inter-planar distance $d_{hkl}$ of planes with miller indices (*hkl*), given by,

$$d_{hkl} = \frac{a_F}{\sqrt{h^2 + k^2 + l^2}} \tag{2.29}$$

where $a_F$ is lattice constant of FCC structure and related to the Bragg's law by,

$$n\lambda = 2d_{hkl}\,\mu_m\,sin(\theta_g) \tag{2.30}$$

where $n$ is order of diffraction and $\theta_g$ is the glancing angle. By combining Eqns. 2.29 and 2.30, the subsequent peak position was determined using,

$$sin\left(\frac{\theta_2}{2}\right) = \frac{\sqrt{h_2^2 + k_2^2 + l_2^2}}{\sqrt{h_1^2 + k_1^2 + l_1^2}} sin\left(\frac{\theta_1}{2}\right) \tag{2.31}$$

Similarly, for HCP structure the first peak corresponds to the Bragg reflection from (100) planes and other allowed peak positions for the HCP structure are calculated using the position of $q_{100}$ peak and inter-planar distance $d_{hkl}$ given by

$$d_{hkl} = \frac{1}{\sqrt{\frac{4}{3a_H^2}(h^2 + hk + k^2) + \frac{l^2}{c_H^2}}} \tag{2.32}$$

where $a_H$ and $c_H$ are lattice constants of HCP structure. The structure of PNIPAM microgel crystals is identified to be FCC/HCP or FCC-HCP coexistence by calculating all the Bragg peak positions for the structure and matching with that

measured experimentally. The first peak position, $q_{111}$ of FCC structure is related to the number density, $n_p$by,

$$n_p = \frac{4}{3\sqrt{3}}\left(\frac{q_{111}}{2\pi}\right)^3 \tag{2.33}$$

and to the nearest-neighbour distance, $d_{nn}$ by,

$$d_{nn} = \left(\frac{\sqrt{2}}{n_p}\right)^{\frac{1}{3}} \tag{2.34}$$

Similarly, the first peak position, $q_{100}$ of HCP structure is related to number density, $n_p$by,

$$n_p = \frac{3}{2}\left(\frac{q_{100}}{2\pi}\right)^3 \tag{2.35}$$

The $n_p$ value determined using SLS and the *d* value determined using DLS were used to determine the volume fraction using the relation,

$$\phi = n_p \frac{\pi d^3}{6} \tag{2.36}$$

**c) Light scattering set-up**

Static and dynamic light scattering measurements have carried out using light scattering set up (M/s Malvern, UK, model 4700). Schematic of the light scattering set-up (top view) is shown in Fig. 2.6. The light scattering set-up is equipped with a linearly polarized He-Ne laser operating at a wavelength, $\lambda = 632$ nm, lenses, neutral density filter, vat, analyser, detector and a multi tau correlator. The set-up consists of a goniometer with an arm to mount the detector (Photo multiplier tube, (PMT)), to collect the scattered light at different angles (between 10° to 150°) with an angular

resolution of 0.1°. A pin hole with an adjustable aperture placed before the PMT is used for varying the detector exposed to the scattered light. In order to enhance the coherence factor, β scattering volume is reduced by focusing the incident light at the centre of the vat and by decreasing the pinhole size placed before the detector.

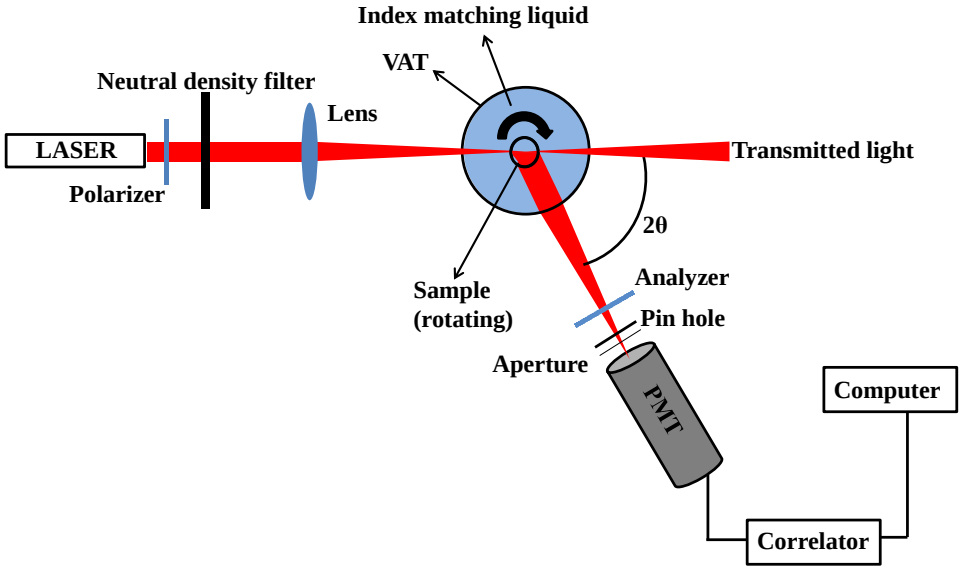


**Figure 2.6** Schematic diagram of light scattering set up.

Vat contains index matching liquid (toluene) which also serves as temperature bath. Temperature of the vat, hence the sample temperature is varied from 10 °C to 60 °C with temperature stability of ± 0.1 °C, using a heating coil attached to it. *XY* plane is the scattering plane in which laser is placed along *x*-direction and the detector in *y*-direction. Vertical polarization of the incident light is achieved by aligning the polarization of the laser parallel to *z*-direction. The analyser is used to select the scattering geometries i.e., V-V (vertical-vertical) or V-H (vertical-horizontal). In V-V geometry, vertically polarized light is incident on sample and the analyser is aligned in such an orientation that only vertical component of the scattered light is allowed to reach the detector. In V-H geometry, vertically polarized light is incident on sample and horizontal component of the scattered light is detected. This geometry is also

known as depolarized light scattering geometry. Digital correlator processes the signal from PMT to compute the correlation function using multi-tau correlator. The correlator signal is then passed on to the computer for determining the correlation function and for further analysis. Correlator of model 7132 is used in our set-up for computing the correlation function.

**d) Alignment procedure**

a) Laser beam is made to pass through the crosswire placed on the goniometer using the translational, horizontal and vertical screws. The laser is ensured to be parallel to the plane of the table.

b) The beam is made to pass through the centre of the flat portion of the VAT, which is placed in the ring and exits out through the other end. Finally the three levelling screws are tightened.

c) The vat is covered on the top with its cover lid and tightened. The vat is filled with toluene from top and simultaneously ensured that the beam should pass through the pinhole, crosswire as in the first step.

d) The focusing lens is tightened in its position. Using the fine screw on the focusing lens assembly, the lens is adjusted to a position such that the beam is passing through the pinhole and crosswire.

e) To ensure complete alignment, a thin platinum wire is inserted at the sample position perpendicular to the beam and the diffraction fringes are verified. The diffraction fringes will be symmetric on both sides of the centre if the beam is in a straight line. With this, the alignment gets completed. Then the cross wire in the goniometer meter is replaced with PMT and tightened.

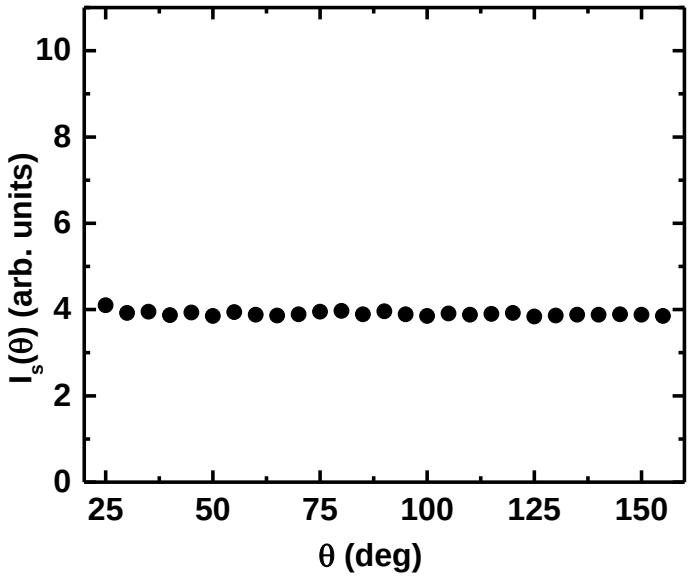


**Figure 2.7** Scattered intensity, $I_s(\theta)$ as a function of scattering angle, $\theta$ measured for toluene.

The alignment of the instrument is cross checked by measuring the scattered intensity at different angles with toluene placed at the sample position. The count rate from the toluene sample at scattering angles of $30^o$, $90^o$ and $150^o$ are compared with each other. The scattering volume is different at oblique scattering angles, which means the observed count rate is expected to go proportional to $\sin(\theta)$ where $\theta$ is the scattering angle. A correction for this effect is automatically made in angular scan measurement provided the alignment is made to satisfy, Count rate at 30° = Count rate at 150° = 2(Count rate at 90°). This relation holds well within 5% for a good alignment. Figure 2.7 shows the scattered intensity as a function of scattering angle for toluene in 10 mm cell. The scattered intensity corrected for its angle dependence remains constant from 20° to 150° which represent good alignment for the instrument.

**e) 3D dynamic light scattering technique**

The light scattering theory mentioned above is valid only for single scattering events. Single scattering of light refers to the light scattered by the particles once and

reaches the detector without getting scattered from other particles. Light scattered many times by particles before reaching the detector is termed as multiple scattering of light [97]. Multiple scattering of light occurs in dense suspensions or suspension with high refractive index contrast. In the event of multiple scattering of light, all the formalisms discussed in the previous section doesn't hold good.

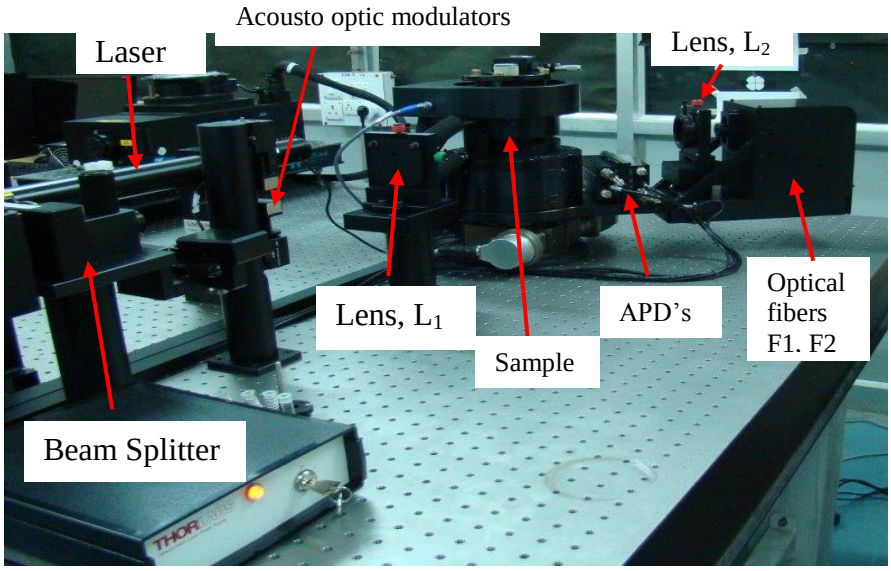


**Figure 2.8** Photograph of cross-correlation light scattering setup.

Singly scattered light amidst multiply scattered light can be measured using cross-correlation technique and used to characterize turbid colloidal suspensions [102,105]. Cross-correlation light scattering technique is also known as 3D light scattering (3D DLS and 3D SLS) (Fig. 2.8). In 3D light scattering technique, two light scattering experiments are performed, simultaneously, using two laser beams having wave vectors $\bar{k}_{i1}, \bar{k}_{i2}$ which cross each other at an angle, $\psi$ at the centre of the vat and scattered light from corresponding beams is detected at wave vectors $\bar{k}_{s1}, \bar{k}_{s2}$, respectively using two detectors, at two different planes. To facilitate this, two detectors are placed on the goniometer such that both detectors see same scattering wave vector with respect to the singly scattered light, $|\bar{q}| = |\bar{k}_{i1} - \bar{k}_{s1}| =$

$\left|\bar{k}_{i2} - \bar{k}_{s2}\right|$ (Fig. 2.9).Normalized intensity cross-correlation function, $g_{12}^{(2)}(q,\tau)$ is calculated using the intensities obtained through two detectors, $I_1(q,t')$ and $I_2(q,t'+\tau)$ is given by

$$g_{12}^{(2)}(q,\tau) = \frac{\langle I_1(q,t')I_2(q,t'+\tau)\rangle}{\langle I_1(q)\rangle\langle I_2(q)\rangle} \tag{2.37}$$

Both detectors detect both singly scattered and multiply scattered light. Light scattered upon many times will reach the detector with different $\vec{q}$. Intensity of light scattered at same $\vec{q}$ is temporally correlated, whereas that for different $\vec{q}$ is temporally uncorrelated. Hence, upon cross-correlating the intensities from two detectors, multiple scattered component of light gives rise to constant background and single scattered component of light contributes to the correlation. Using Siegert's relation, $f(q,t)$ is obtained from $g_{12}^{(2)}(q,\tau) = 1 + |\beta f(q,t)|^2$, with $\beta = \beta_m\beta_{12}\beta_c$ where $\beta_m$, $\beta_{12}$ and $\beta_c$ are factors due to multiple scattering, commonality to two laser beams and alignment of the instrument. Time averaged intensity due to singly scattered light alone from turbid suspension is given by $I(q) = \sqrt{I_1^M I_2^M\, \beta^{conc}/\beta^{dilute}}$ where $I_1^M$ and $I_2^M$ are the intensity detected by two detectors, respectively.

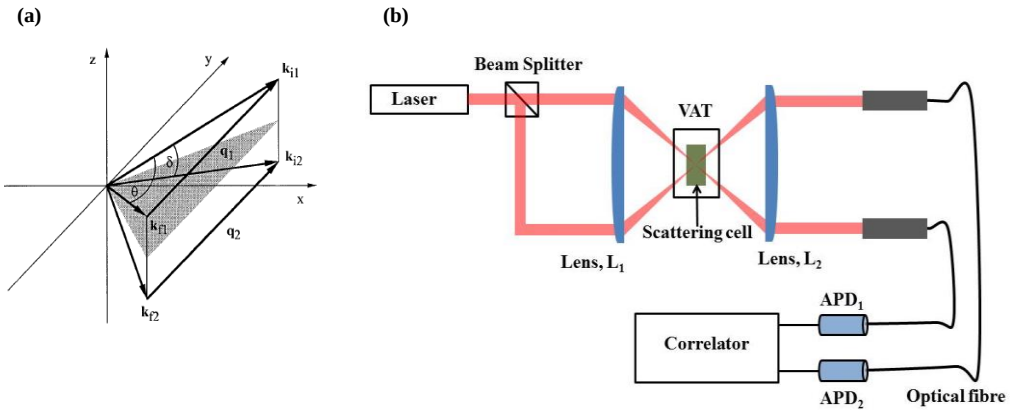


**Figure 2.9** (a) Ray diagram showing scattering geometry of 3D light scattering setup, (b) Schematic of the cross-correlation light scattering setup

For probing turbid suspension, we have used 3D DLS setup (LS Instruments AG, Fribourg, Switzerland) which is equipped with He-Ne laser (632 nm), vat (with decalin as index matching liquid), two Avalanche photo diodes (APD) as detectors, and multi tau correlator. Sample temperature is controlled to accuracy of ± 0.1 °C by circulating heat exchanger fluid around the VAT. The scattered intensity $I_s(\theta)$ observed for toluene in 10 mm cell is constant over the scattering wave vector range from $q$ = 0.68 x $10^5$ $cm^{-1}$ to 2.54 x $10^5$ $cm^{-1}$ indicating the alignment of the system (Fig. 2.10(a)). Due to overlap of two laser beams at the centre of the scattering cell, the intensity cross-correlation function's intercept decreases to 0.25 from its ideal value of 1. In order to increase the intercept of intensity cross-correlation function, acousto-optic modulators (AOMs) are used, which periodically allows one of the two beams by diffracting the other beam out of the scattering cell. By this way, overlap of two beams is avoided. The time period of this switching of beams is 3 µs. With AOMs, $g_{12}^{(2)}(q,0)$ is observed to increase up to 0.74. Fig. 2.10(b) shows the Intensity correlations measured in auto and cross-correlation mode for dilute suspension of polystyrene particles of size 70 nm.

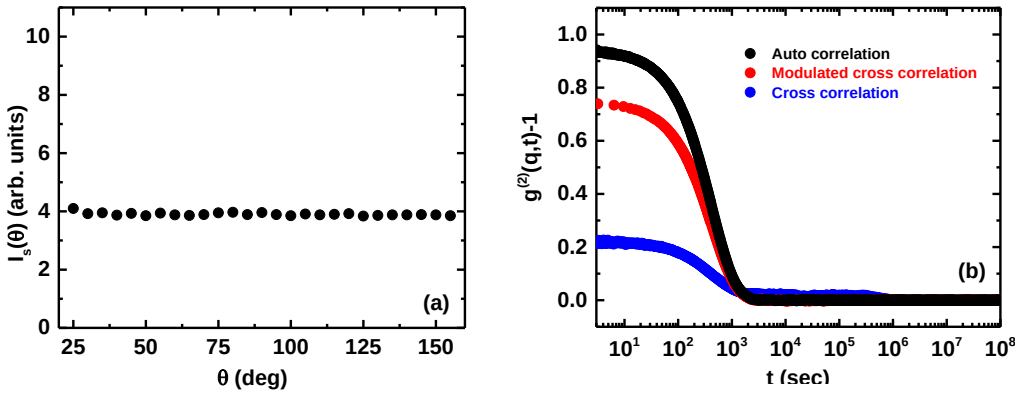


**Figure 2.10** (a) Scattered intensity, $I_s(\theta)$ as a function of scattering angle, $\theta$ measured for toluene, (b) Intensity cross-correlation functions measured in auto and cross-correlation mode on dilute polystyrene (70 nm diameter) suspension.

**f) Non-ergodic analysis**

A dynamical system is termed as non-ergodic when the time averaged property is different as that averaged over all the phase space of the system. In non-ergodic colloidal suspensions, time averaged, $g^{(2)}(q,t)$ measured at different sample locations are different and true ensemble average of $g^{(2)}(q,t)$ is obtained by averaging the correlation function at different sample locations, in order to obtain $f(q,t)$. A simple method was proposed by Pusey and Van magen [106] and Furukawa [107] to get $f(q,t)$ for non-ergodic samples. Just by measuring time averaged $g^{(2)}(q,t)$ at single sample location, $f(q,t)$ using their method. According to their method,

$$f(q,t) = \frac{Y-1}{Y} + \frac{\sqrt{g^{(2)}(q,t) - \sigma_I^2}}{Y} \tag{2.38}$$

By measuring, ensemble averaged scattered intensity, $\langle I(q)\rangle_E$ and time averaged scattered intensity, $\langle I(q)\rangle_t$ and the ratio of them gives the non-ergodicity factor, *Y*.

$$Y = \frac{\langle I(q)\rangle_E}{\langle I(q)\rangle_t} \; ; \qquad and \qquad \sigma_I^2 = \frac{\langle I^2(q)\rangle - \langle I(q)\rangle^2}{\langle I(q)\rangle^2} = \; g^{(2)}(q,0) - 1$$

where $\sigma_I^2$ is mean square fluctuation of the scattered intensity. The average of the scattered intensity obtained by rotating the sample or translating the sample which exposed different locations in the sample will give $\langle I(q)\rangle_E$ and time averaged measurement of scattered intensity at one location in sample will give $\langle I(q)\rangle_t$. $f(q,t)$ for turbid non-ergodic samples using cross-correlation technique is given by

$$f(q,t) = 1 + \frac{1}{Y}\left\{\left[\frac{g_{12}^{(2)}(q,t) - g_{12}^{(2)}(q,0)}{\beta^{dilute}} + 1\right]^{1/2} - 1\right\} \tag{2.39}$$

where $Y = \sqrt{\left(\frac{\langle I_1(q)\rangle_E \langle I_2(q)\rangle_E}{\langle I_1(q)\rangle_t \langle I_2(q)\rangle_t}\right)}$ and the sub-script $E$ denotes ensemble averaged and sub-script $t$ denotes the time averaged scattered intensities and 1and 2 refers to the detector 1 and detector 2.

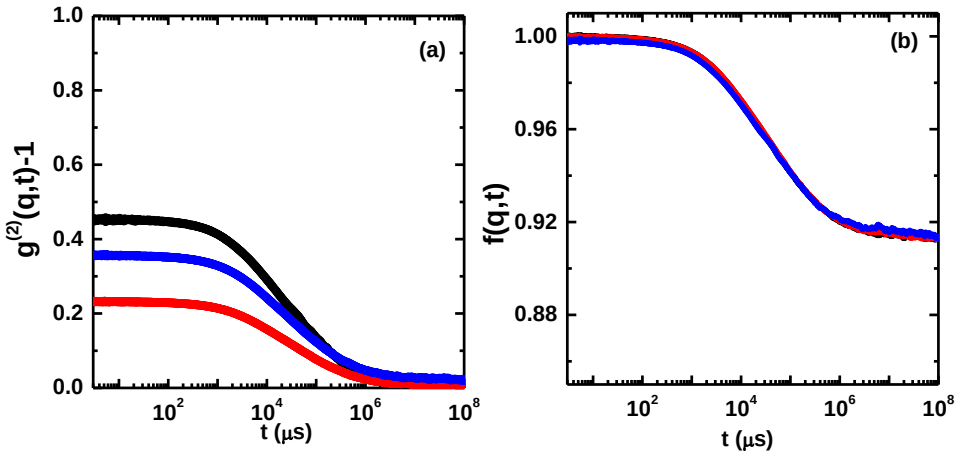


**Figure 2.11** (a) Intensity auto correlation function at different sample position of a non-ergodic system (b) Field auto correlation function obtained through the method mentioned in [106] from intensity auto correlation function.

### 2.5.2 UV-Visible spectroscopy

The structural ordering in dense microgel crystals is recorded using JASCO 650 UV-Visible spectrophotometer. Figure 2.12 shows the schematic of UV-Visible spectrophotometer. The light incident on the sample is attenuated due to scattering and absorption, a part is reflected and the remaining gets transmitted. For a medium of uniform absorption,

$$\%\mathrm{T} = \frac{I_\mathrm{T}}{I_0} \times 100 \tag{2.17}$$

where $I_\mathrm{T}$ is transmitted intensity and $I_0$ is incident intensity and absorbance in the sample, $abs$ is given by,

$$abs = 2 - log(\%T) \tag{2.41}$$

Beer-Lambert law says that, absorption is proportional to the concentration and

$$abs = \vartheta Cl \tag{2.42}$$

where $\vartheta$ is molar extinction co-efficient for the absorbing material at wavelength in units of $(mol \times cm)^{-1}$, $C$ is the molar concentration of the absorbing molecules and $l$ is the optical path length in the material. Beer-Lambert's law is valid between the absorbance values of 0.05 to 0.70. Combing Eqn. 2.40, 2.41 & 2.42, we get

$$log\left(\frac{I_0}{I}\right) = \vartheta Cl \tag{2.43}$$

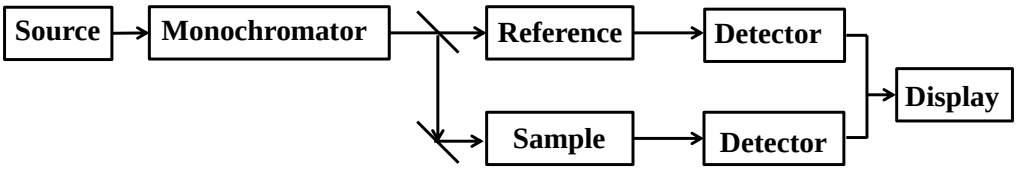


**Figure 2.12** Schematic diagram of UV-Vis Spectrometer.

The spectrophotometer used was having double beam setup with a wavelength range between 900 nm to 200 nm, which is achieved using deuterium lamp and a halogen lamp as the sources covering ultraviolet region and visible region respectively. The minimum wavelength resolution attainable in our setup is 0.1 nm. A double monochromator is used to disperse the composite light into different component of wavelengths. The incident beam is split into two beams, *viz.*, reference and sample beam using a chopper mirror. The reference beam is used to neutralize the effect of sample cell and solvent. Two PMT's are employed for detecting beam through reference cell and sample cell. All spectra reported in thesis are recorded in normal incidence mode with the sample being sandwiched between two quartz plates with a groove of 100 μm.

UV-Visible spectroscopy is known to be useful tool to characterize structural ordering [56,108,109] and for studying crystallization and melting kinetics [110,111] in colloidal crystals. Peaks observed in absorption spectrum of PNIPAM microgel crystals are due to Bragg diffraction of λ that satisfy Bragg condition, $n\lambda = 2d_{hkl}\mu_m \sin(\theta_g)$. Here $\theta_g$ is the glancing angle which is 90º, $d_{hkl}$ is the interplanar distance between crystal planes with (*hkl*) miller indices and *n* is the order of diffraction [112]. Under normal incidence, the Bragg's condition reduces to,

$$n\lambda_{hkl} = 2d_{hkl}\mu_m \tag{2.44}$$

and subsequent peaks occur at λ values satisfying the condition,

$$\lambda_{h_2k_2l_2} = \frac{\sqrt{h_1^2 + k_1^2 + l_1^2}}{\sqrt{h_2^2 + k_2^2 + l_2^2}}\lambda_{h_1k_1l_1} \tag{2.45}$$

The dense plane, (111) of the FCC structure and (002) of HCP structure are known to grow parallel to the walls of the sample cell [70,113]. Prominent peaks in absorption spectra correspond to (111) peak of FCC structure or (002) peak of HCP structure.

### 2.5.3 Optical tweezers

Volume phase transition (VPT) of microgels is a property of polymer. Investigation on a single particle should enable us in identifying the VPT. Optical tweezers (OT) is a non-invasive technique which allows trapping a single microgel particle and identifies the VPT with respect to external stimuli. The trap stiffness $\kappa$ is used to identify the transition precisely. Light has energy, linear momentum and angular momentum which are used to heat or cut materials, to move or trap the particles and to rotate or twist the particles, respectively. A highly focused laser beam,

capable of holding microscopic objects stable in three dimensions, is known as optical trap (Fig. 2.13) [94].

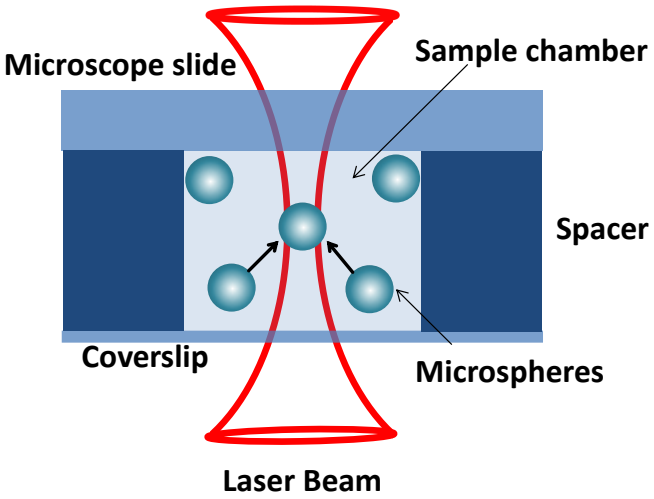


**Figure 2.13** Schematic of optical trap and sample cell containing colloidal particles suspended in a medium.

Optical tweezers (OT) uses linear momentum and angular momentum of light to exert force and torque on microscopic objects, respectively to manipulate them. Using a high numerical aperture (NA) microscopic objective lens, the laser beam is focused down to a diffraction limited spot which is capable of trapping microscopic particles in its focus. Lower NA objectives will confine the particles on the optic axis of the beam but will not trap the particle at the focus because of intensity gradient being low [114]. At the focus, laser beam creates a potential well strong enough to trap a particle with refractive index greater than that of the surrounding medium. OT is a non-invasive tool to generate Pico-Newton force to manipulate and track microscopic objects with nanometer and microsecond resolution [115,116]. Because of its versatile nature, OT has found application in physics, biology and material science [117]. With the advent of OT, investigation of a single particle has become a reality and has been used in investigating the refractive index [118], rigidity [119],

electrophoretic forces [120] and local pH measurement in a microchip [121]. The basic principle of optical tweezers can be explained using Newton's third law. The change in momentum of light due to refraction, reflection or absorption is imparted onto the particle. Rate of change of momentum suffered by laser light generates force on the particle. The forces acting on the trapped particle can be decomposed into (a) "scattering force" and (b) "gradient force". (a) Scattering force arises as a consequence of the momentum delivered to the particle by the scattered photons. It is proportional to the intensity of the laser beam and it pushes the particle in the direction of propagation of light. (b) Gradient force is due to the spatial gradient in light intensity and acts in the direction of that gradient. It is responsible for three dimensional trapping of particles. The particle gets trapped at a point where scattering force and gradient force balances each other and capable of overcoming the thermal fluctuations of the particle. The action of these forces on the particles in three different regimes which is classified based on the diameter of the trapped particle ($d$) and the wavelength of the trapping laser ($\lambda$) are discussed in the subsequent section.

**a) Ray optics regime** ($\boldsymbol{d \gg \lambda}$)

In ray optics regime, behaviour of the light incident on the particle is understood using laws of reflection, scattering and Snell's law [122]. Light upon incident on a particle, a fraction of light gets reflected, a fraction gets absorbed and a fraction of light gets refracted. In these processes, there is a change in the momentum of incident light and this net change in the momentum of light is imparted onto the particle, to conserve the momentum of the incident light. The change in momentum generates a force at the interface between particle and solvent. To simplify the calculation of the total optical force acting on the particle, effect of individual ray on

the particle is calculated and then summed up with a weightage according to the intensity.

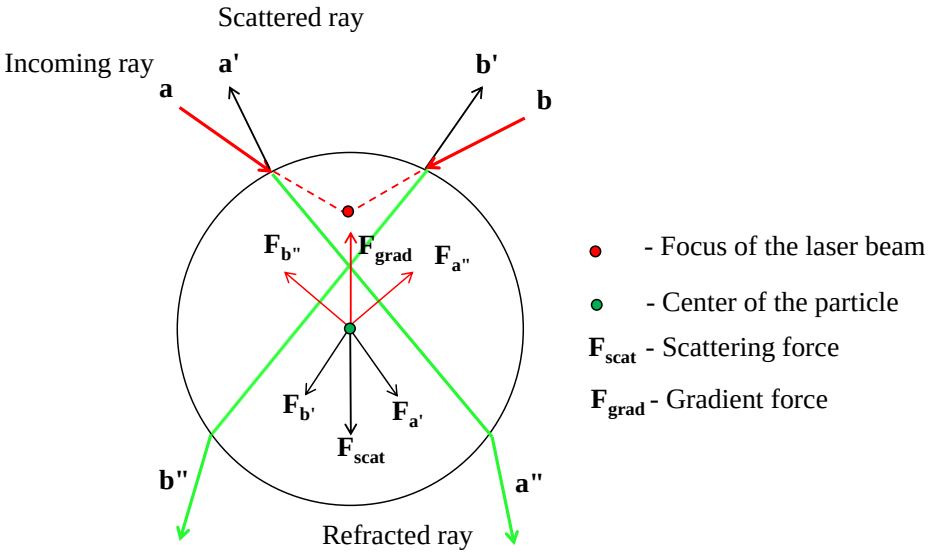


**Figure 2.14** Illustration of scattering and gradient forces acting on the trapped particle in an optical trap.

Let us consider a particle of refractive index, $\mu_p$ immersed in a medium of refractive index, $\mu_m$ is illuminated by a pair of rays "*a*" and "*b*" which are focused inside the particle (Fig. 2.11). The momentum change suffered by the ray of light which is reflected from the interface, generates scattering force. The scattered ray, *a'* gives rise to a force $F_{a'}$ and *b'* gives rise to $F_{b'}$ and their sum is denoted as scattering force, $F_{scat}$ which acts along the direction of the incident light. The momentum change between incident and refracted beam gives rise to gradient force. Refracted ray, *a"* and *b"* generates force $F_{a"}$ and $F_{b"}$ respectively and their vector summation is gradient force, $F_{grad}$, which is acting towards the focus of the laser beam (Fig. 2.14).

The gradient force should be greater than or equal to scattering force for the particle to get trapped. The maximum of gradient force is at the point where the intensity gradient is maximum (at the focus of the objective). For generating such a

gradient in the intensity, cone angle of the focused light should be more, hence the need of high numerical aperture (NA) microscope objective lens. Also note that, gradient force always takes the particle to the focus of the laser beam as shown in Fig. 2.15. The magnitude of scattering force, $F_{scat}$ and gradient force, $F_{grad}$ are given by [122],

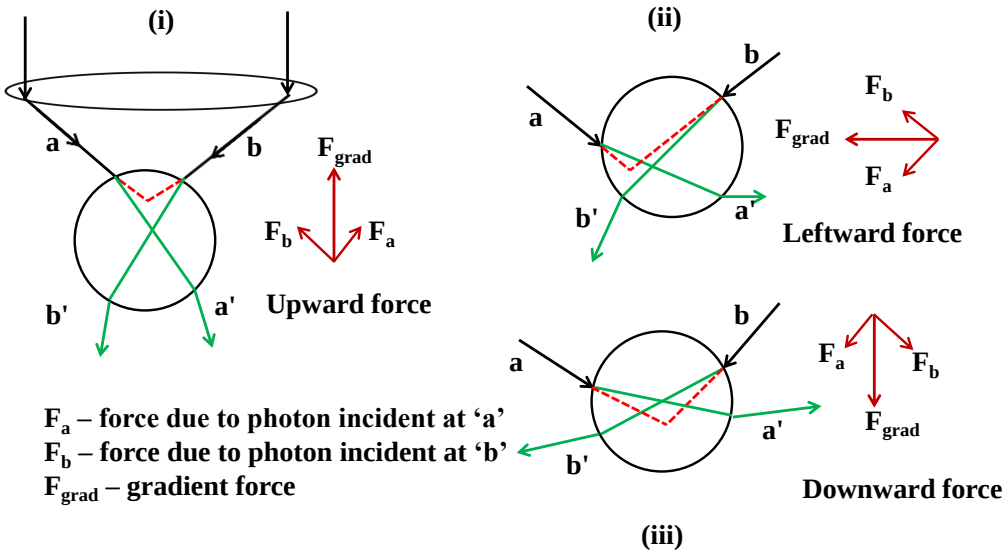


**Figure 2.15** Illustration showing gradient force always drives the trapped particle towards the focus of laser. Only refracted ray has been taken into account as it is the only component contributing for the gradient force. (i) shows particle trapped downstream of the laser focus and gradient force, $F_{grad}$ pulls the particle towards laser focus, (ii) shows particle trapped to right side of the laser focus and $F_{grad}$ pulls the particle towards left (laser focus), (iii) shows particle trapped above laser focus and $F_{grad}$ pulls the particle downwards towards laser focus.

$$F_{scat} = \frac{\mu_m P}{c}\left(1 + R\cos 2\theta_1 - \mathrm{T}^2\frac{\cos 2(\theta_1 - \theta_2) + R\cos 2\theta_1}{1 + 2R\cos 2\theta_2 + R^2}\right) \quad (2.46)$$

$$F_{grad} = \frac{\mu_m P}{c}\left(R\cos 2\theta_1 - \mathrm{T}^2\frac{\sin 2(\theta_1 - \theta_2) + R\cos 2\,\theta_1}{1 + 2R\cos 2\theta_2 + R^2}\right) \quad (2.47)$$

where the reflection coefficient, *R* is given by

$$R = \left( \frac{cos\,\theta_1 - \sqrt{\mu^2 - sin^2\,\theta_1}}{cos\,\theta_1 + \sqrt{\mu^2 - sin^2\,\theta_1}} \right)^2 \tag{2.48}$$

and the transmission coefficient, $T = 1 - R$. Here, $\mu$ is the relative refractive index defined as $\mu = \frac{\mu_p}{\mu_m}$ and $\mu_p$ is the refractive index of the particle and $\mu_m$ is the refractive index of the medium. *P* is the laser power, *c* is the velocity of light in vacuum, $\theta_1$ is the angle of incidence, $\theta_2$ is the angle of refraction as shown in Fig. 2.16. Note that in ray optics limit ($d \gg \lambda$), the forces acting on the particle do not depend on particle diameter, *d*.

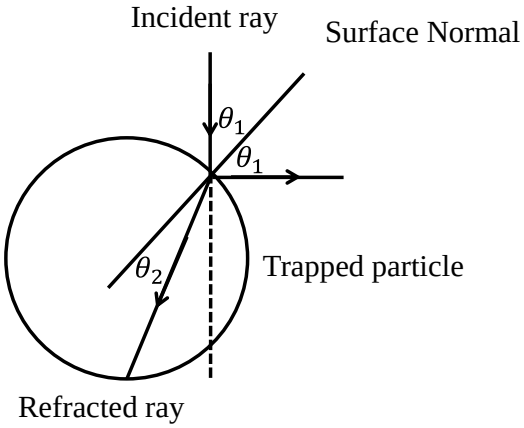


**Figure 2.16** Illustration showing the angle of incidence, $\theta_1$ and angle of refraction, $\theta_2$ with respect to the surface normal of the particle in the optical trap.

### b) Rayleigh regime ($d \ll \lambda$)

In the Rayleigh limit ($d \ll \lambda$), the optical forces on the particle are calculated by treating the particle as an induced dipole and the forces arise from dipole-field interactions [94]. The scattering force exerted on the particle is given by,

$$\vec{F}_{scat} = \frac{I_0}{c}\frac{2\pi^5 d^6 \mu_m}{3\lambda^4}\left(\frac{\mu^2-1}{\mu^2+2}\right)^2 \hat{z} \tag{2.49}$$

where $I_0$ is the intensity of the field, $\hat{z}$ is the unit vector along the propagation direction. The scattering force tends to push the particle along the optic axis. It depends on the diameter of the particle ($d$) and wavelength of the trapping laser ($\lambda$). The induced dipole experiences a force (Lorentz force) upon exposed to inhomogeneous electric field termed as gradient force and is given by,

$$\vec{F}_{grad} = -\frac{\mu_m^3 d^3}{16}\left(\frac{\mu^2-1}{\mu^2-2}\right)\vec{\nabla} I_0 \tag{2.50}$$

Since, gradient force is conservative in nature; the trapping potential, $U$ is given by,

$$Trapping\ potential, U = \frac{\mu_m^3 d^3}{16}\left(\frac{\mu^2-1}{\mu^2-2}\right) I_0 \tag{2.51}$$

The gradient force is proportional to the gradient of intensity and is responsible for the lateral and axial trapping of the particle. In Rayleigh limit, scattering force, $F_{scat}$ is proportional to $d^6$ whereas the gradient force, $F_{grad}$ is proportional to $d^3$, which implies that $F_{scat}$ decreases faster than $F_{grad}$ as size decreases. For smaller particles, the velocity distribution is Maxwellian in nature. At any point of time, there exists a non-zero probability for the particle to have instant velocity greater than average velocity. Hence, it's important to create a potential well depth roughly 10 times more than the kinetic energy of the particle. Since the well depth decreases with decrease in *d*, it is difficult to trap a particle which is too small in size and sets the lower limit for the particle diameter that can be trapped using optical tweezers.

**c) Intermediate regime ($d \approx \lambda$)**

In the intermediate regime ($d \approx \lambda$), optical forces experienced by the particle is calculted using Mie theory [123]. Under dipole approximation for a spherical particle under highly localized beam, the phase of the field doesn't vary significantly over the spot size, $\omega$ of the focussed laser beam. Hence the interference effects can be neglected. Under this approximation, the expression for the gradient force is with $\omega$ as the relevant parameter than the diameter of the particle, $d$ [123].

$$F_{grad}(r) = \varepsilon I_0 \omega^2 A(\epsilon) e^{-(1/2)u^2} sinh(a_c u) \tag{2.52}$$

with $\varepsilon$ is the relative difference of the dielectric constants of the particle, $\varepsilon_p$ and the medium, $\varepsilon_m$ and given by $\varepsilon = \frac{\varepsilon_p}{\varepsilon_m} - 1$, $I_0$ is the intensity of the laser beam, ω is the dimensions of the beam waist in the transverse direction and $A(\epsilon) = 4\pi\varepsilon \operatorname{erf}\left(\frac{a}{\sqrt{2}}\right) \operatorname{erf}\left(\frac{a}{\sqrt{2}\epsilon}\right) e^{-(1/2)u^2}$ where $a_c = \frac{R}{\omega}\left(\frac{\pi}{6}\right)^{(1/3)}$ and $u = \frac{r}{\omega}$ and $\epsilon$ being the eccentricity.

### 2.5.4 Trap stiffness measurement

Optical tweezers are ideally suited to exert forces of the order of picoNewton in the system and for that accurate calibration of the the system is essential. Instead of measuring forces in optical traps directly, trap stiffness is first determined, which is a quantitative measure of trap strength. Trap stiffness is used to determine the force exerted on the trapped particle. For small displacements from the equilibrium position of the trap, the restoring force along $x$ direction, $F_x$ and the displacement, $x$ is related through Hooke's law, $F_x = -\kappa_x x$, where $\kappa_x$ is the trap stiffness along $x$ direction. There are different methods to measure trap stiffness, $\kappa$ [124]. Here, equipartition method and optical potential analysis methods are described in detail.

### a) Equipartition method

A particle suspended in a fluid undergoes random motion by virtue of the momentum transferred by the surrounding fluid molecules, known as Brownian motion. Its significance in calibrating optical tweezers is well known, as it drives the particle to explore the optical potential landscape created by an optical trap. Equipartition theorem states that the energy associated with each degree of freedom is $^1/_2\, k_B T$. For a particle bound in a harmonic trap with stiffness, $\kappa_x$ along *x* direction is related by [124],

$$\frac{1}{2} k_B T = \frac{1}{2} \kappa_x \langle x^2 \rangle \tag{2.53}$$

where $k_B$ is the Boltzmann constant, $T$ is the absolute temperatuare and $\langle x^2 \rangle$ is the variance in displacement of the particle from its equilibrium position.

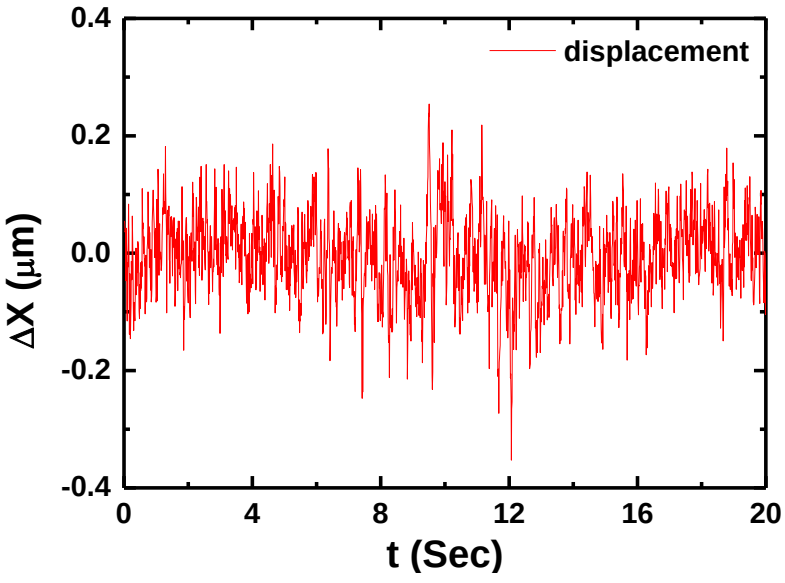


**Figure 2.17** Displacement of the trapped particle as a function of time extracted from the position of the particle in the optical trap.

Similarly, the trap stiffness along *y*-direction, $\kappa_y$ can be obtained from the variance in displacement of the particle along *y* direction. Thus, measuring the positional variance of the trapped particle will enable us to determine the trap stiffness. Advantages of this method are fast determination of trap stiffness and apriori knowledge of the viscosity of the medium is not required. It requires well calibrated position detection system. Any error in determining the position of the trapped particle will only increase $\langle x^2 \rangle$ artificially and underestimate the trap stiffness. The position of trapped particle as a function of time is recorded as video using a CCD camera. Using the position of the trapped particle as a function of time, displacement of the trapped particle from the trap center is calculated (Fig. 2.17). From the displacement data, the variance in the position is obtained and using Eqn. (2.53), the trap stiffness, $\kappa_x$ was obtained.

**b) Optical potential analysis method**

Optical potential analysis method rests on the Boltzmann statistics of position fluctuations of optically trapped particle. The position histogram of the particle trapped by a Gaussian laser beam is assumed to have normal distribution. The probability density function, $P(x)$ of the displacement of a trapped particle in a potential *U(x)* under thermal equilibrium along *x* is given by Boltzmann statistics[125],

$$P(x) = C\ exp\left(-\frac{U(x)}{k_B T}\right) \tag{2.54}$$

where $C$ is normalization constant. Inverting Eqn. 2.54 yields the expression for optical potential, *U(x)* experienced by the trapped particle.

$$\frac{U(x)}{k_B T} = -ln\left(\frac{P(x)}{C}\right) \tag{2.55}$$

*U(x)* is harmonic at the vicinity of the minima of the potential well [125,126], hence can be fitted with harmonic oscillator potential given by,

$$\frac{U(x)}{k_B T} = \frac{\kappa_x x^2}{2k_B T} \tag{2.56}$$

The trap stiffness along *y* direction is also calculated in the same way. The advantage of this method is, it requires only temperature as input for stiffness calculation and allows to measure energy landscapes with high spatial and temporal resolution. The accuracy of this method is better than equipartition theorem [125]. The spatial resolution is restricted by the sensitivity of the position detectors. Combined with other methods, it can be used in measuring local viscosity, pH etc.

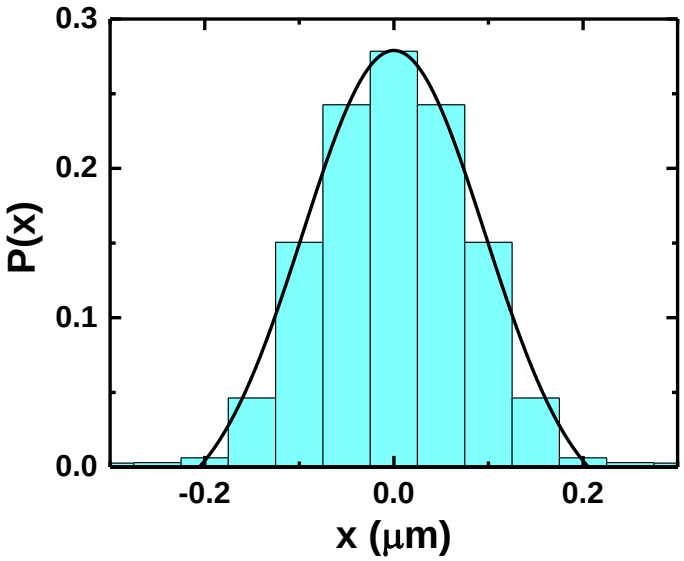


**Figure 2.18** Probability distribution, *P(x)* constructed using position coordinates of the trapped particles as a function of displacement *x*.

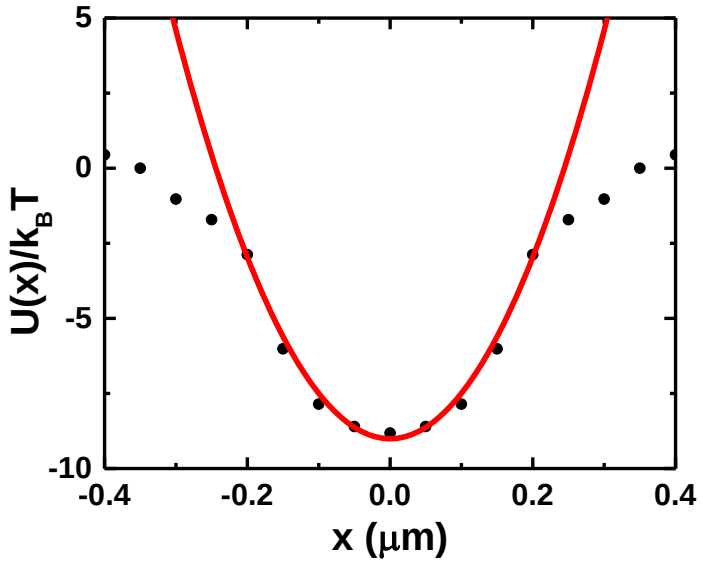


**Figure 2.19** *U(x)/$k_B$T* versus displacement *x* from the mean position of the trap. Continuous line is fit to Eqn. 2.56.

Using the displacement data of the trapped particle, position histogram as a function of displacement, *x* from the centre of the trap is constructed, which is analogous to probability distribution, *P(x)* as shown in Fig. 2.18. The displacement of the trapped particle is expected to have normal distribution resulting from the Gaussian nature of the intensity distribution in the laser beam. The probability of locating the particle is maximum at the trap center where the potential energy is minimum. From the probability distribution function, *P(x)* optical potential experienced by the trapped particle, *U(x)* is obtained using Eqn. (2.55). Potential created by optical tweezers is harmonic near the center of the trap [126] as shown in Fig. 2.19. The optical potential data is fitted with Eqn. 2.56 to extract the trap stiffness, $\kappa_x$.

### 2.5.5 Factors influencing trap stiffness

There are many factors influencing the trap stiffness and are to be taken care during experiments.

### i. Laser power

Laser power at the focal spot will determine the trap stiffness and force exerted on the particle. Laser, typically with Gaussian $TEM_{00}$ mode which can be focussed to smallest beam waist is preferred as it produces the most efficient harmonic trap. The trap stiffness increases linearly with the laser power [124].

### ii. Polarization of the laser

For systems with high numerical aperture objectives, the lateral trap stiffness along two orthogonal directions (*x* and *y*) in the trapping plane are different [127] if linearly polarized laser is used for trapping experiment. The difference between the lateral trap stiffness value in two orthogonal directions depends on the size of the particle [128]. In presence of spherical abberations in the system, the difference between them decreases [129]. This problem is avoided by employing circularly polarized laser for trapping experiment.

### iii. Axial trapping distance

The effect of spherical aberration increases with distance from the glass-water interface, due to the refractive index mismatch between the immersion oil and cover slip. It greatly influences the trap stiffness and decreases it roughly to half of its maximum value without spherical aberrations. It is overcome by using immersion oil with different refractive index to reduce the mismatch [130]. It improves the trapping efficiency and with less laser power, efficient trapping is feasible.

### 2.5.6 Optical tweezers set-up

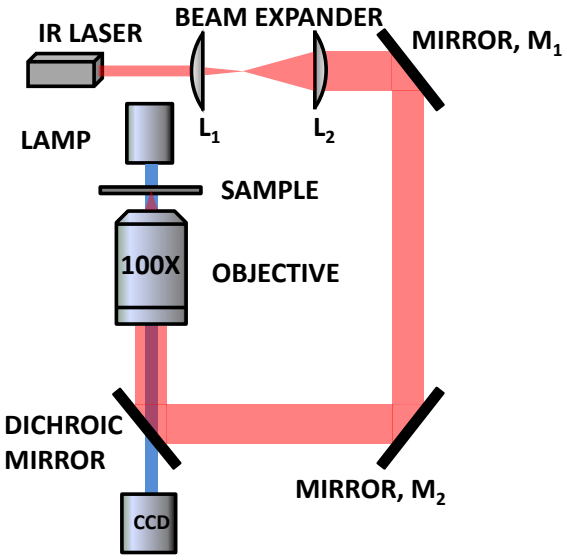


**Figure 2.20** Schematic of optical lay out of the optical tweezers set-up.

We have designed and assembled an optical tweezers set-up for trapping experiments using a linearly polarized, $TEM_{00}$ mode, 1064 nm wavelength Nd-YAG fibre coupled laser. The schematic of the indigenously developed OT set-up is shown in Fig. 2.20. The laser beam of 1mm diameter is expanded to a beam of diameter of 6 mm ( ~ 1.2 times the diameter of the back aperture of 100X / 1.4 oil immersion microscope objective lens used for trapping experiments) using a beam expander which consists of a set of Plano convex lens, $L_1$ (f = 75 mm) and $L_2$ (f = 500 mm). The expanded beam is coupled to an Olympus IX-81 inverted microscope through a set of steering mirrors, $M_1$ and $M_2$ and a 850 short pass dichroic mirror which reflects radiations with wavelength greater than 850 nm and transmits radiations of wavelength below 850 nm. This optical alignment produces a tightly focused laser beam at the focal point of the objective in the sample plane, capable of trapping dielectric colloidal particles in three dimensions. The polarization axis of the laser is

made to coincide with the *x*-axis of the trapping plane. The trapped particles are imaged using a white light illumination source and a CCD camera placed at the trinocular port of the microscope.

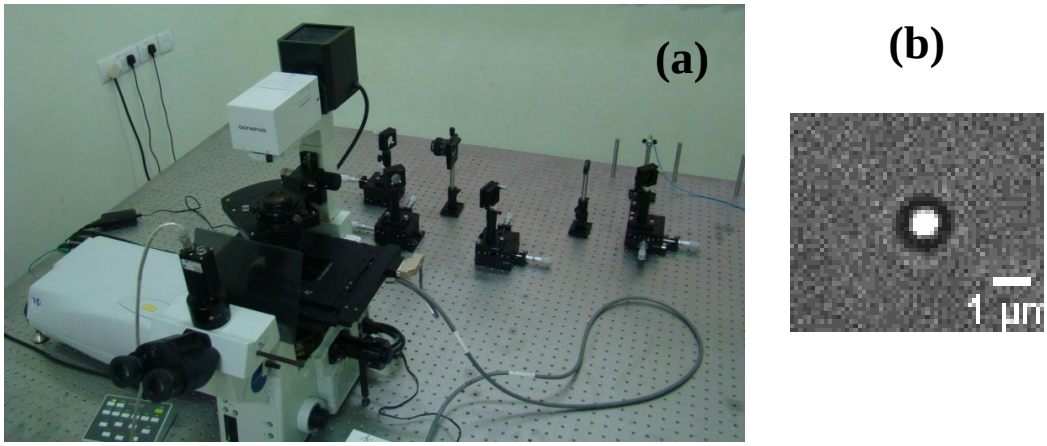


**Figure 2.21** (a) Photograph of home built optical tweezers set-up. (b) Image of the trapped polystyrene particle with $d$ = 600 nm.

The dichroic mirror placed between microscope objective lens and CCD camera (Basler scout, scA640-120fm) transmits the white light while reflects the laser beam which prevents the CCD camera from being exposed to the laser. Fig. 2.21(a) shows the designed and home built optical tweezers set up and Fig. 2.21(b) shows the image of 600 nm polystyrene particles trapped in optical trap.

### 2.5.7 Calibration of optical tweezers set-up

Optical tweezers set-up described above is calibrated by trapping polystyrene particles of size 600 nm dispersed in water at different laser power. The laser power is measured in the sample plane without the sample cell in place. The detector head of the laser power meter being larger than the thickness of the sample cell prevents us to make measurement of the laser power in the trapping plane. The position of trapped particle as a function of time, has been recorded as a video using CCD camera at 100

fps. The CCD camera was calibrated by imaging standard TEM grid (M/s. PELCO, US, 500 mesh grids) and 1 pixel is calibrated to be equal to 0.123 μm. The integration time (exposure time) of our CCD camera is 16 μs which is two orders less than the characteristic time scale or trap relaxation time of the trapped particle. This ensures measurement of position of the trapped particle is unbiased [131]. The mismatch of refractive index between the immersion oil and the cover slip while using oil immersion microscope objective was known to introduce spherical aberration in the system which affects trapping efficiency as a function of axial distance [130]. Hence all the measurements are performed at a distance of 20 μm from the glass water interface so as to keep the trapping efficiency constant throughout the measurements. The recorded videos are processed using image processing software and particle tracking algorithm is used to get the co-ordinates of the particle positions in the trap. Having the position data of a trapped particle, there are several ways to characterize the optical potential well, *U(x)* and deduce the optical trap stiffness, $\kappa_x$ [124]. The trap stiffness, $\kappa_x$ is determined using (a) equipartition method and (b) optical potential analysis.

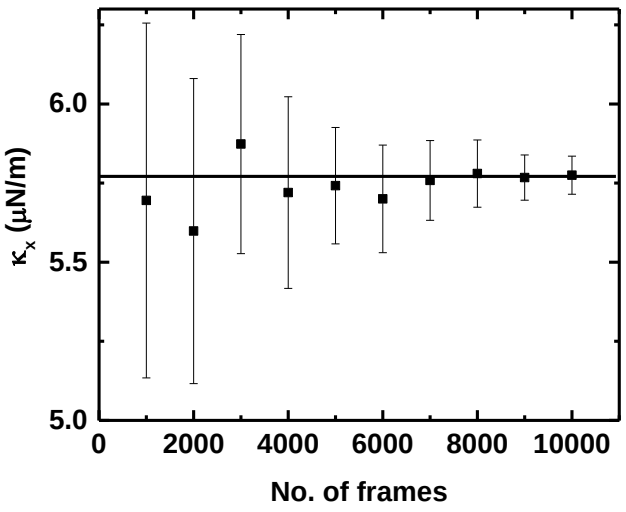


**Figure 2.22** Variation of trap stiffness, $\kappa_x$ with number of frames. Solid line indicates the value of trap stiffness determined using the particle positions detected over 10000 frames.

The number of frames that to be required to determine trap stiffness, $\kappa$ was determined by trapping polystyrene particle of 600 nm and recording different number of frames at the rate of 100 fps at constant laser power (9 mW) at the same trapping plane. The experiment is repeated 10 times for obtaining each data point and trap stiffness is determined using the position data of a trapped particles using optical potential analysis method and is shown in Fig. 2.22. Notice that error in determining $\kappa_x$ decreases with increasing the number of frames and beyond 8000 frames the error in determining the $\kappa_x$ does not reduce the error significantly. The trap stiffness, $\kappa_x$ values reported in this thesis corresponds to the data analyzed from 10000 frames. The trap stiffness for different laser powers determined using equipartition and optical potential analysis methods are given in Table 2.4. It can be seen form table 2.4 that trap stiffness increases with increase in the laser power.

**Table 2.4** Trap stiffness values for polystyrene particle of size 600 nm suspended in water and trapped using 1064 nm laser for different laser power.

| **Laser power (mW)** | **Trap stiffness (μN/m)** | |
|---|---|---|
| | **Equipartition method** | **Optical potential analysis method** |
| 5.5 | 4.5 ± 0.14 | 4.50 ± 0.07 |
| 9 | 5.8 ± 0.18 | 5.75 ± 0.05 |
| 11.25 | 7.5 ± 0.12 | 7.65 ± 0.05 |
| 13.5 | 9.1 ± 0.15 | 9.15 ± 0.08 |
| 15.75 | 10.9 ± 0.19 | 11.05 ± 0.05 |
| 22.5 | 15.4 ± 0.13 | 15.45 ± 0.05 |

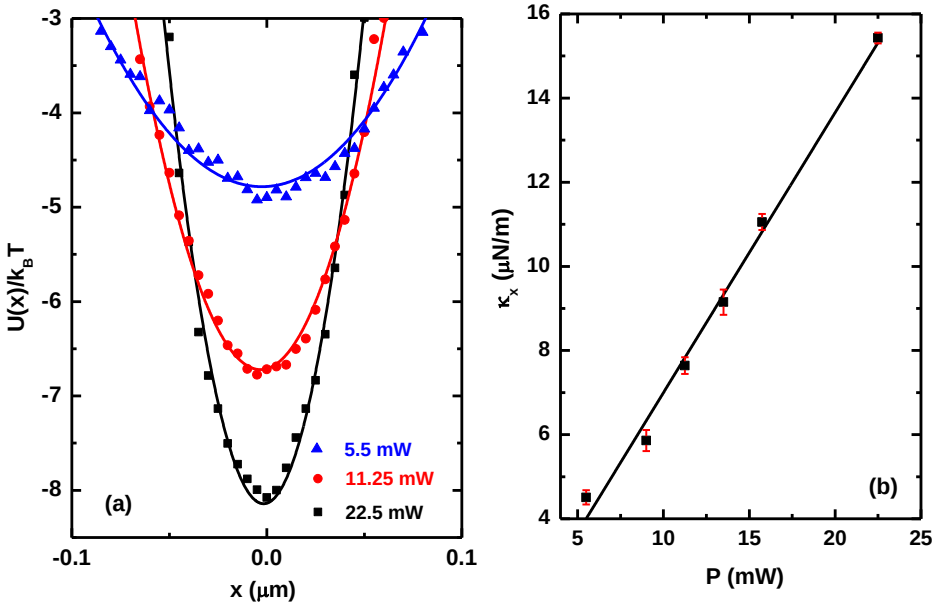


**Figure 2.23** (a) Optical potential $U(x)/k_BT$ versus displacement, $x$ at various laser powers for 600 nm polystyrene particle dispersed in water. Continuous lines are fit to Eqn. (2.56). (b) Variation of trap stiffness, $\kappa_x$ with laser power, $P$.

The optical potential, $U(x)$ traced by the trapped particles obtained using optical potential analysis method is shown in Fig. 2.23(a). The potential well becomes steeper and deeper with increase in the laser power used for trapping the particle. The trap stiffness increases linearly with laser power (Fig. 2.23(b)). Data presented in Table 2.4 and Fig. 2.23 summarizes that the optical alignment of the tweezers set-up is proper and its functioning is normal.

# CHAPTER 3

# IDENTIFICATION OF VOLUME PHASE TRANSITION OF A SINGLE MICROGEL PARTICLE USING OPTICAL TWEEZERS

This chapter deals with the identification of volume phase transition in PNIPAM microgels using DLS and successful implementation of optical tweezers (OT) in the identification of VPT on a single microgel particle. Trap stiffness as an order parameter was used to the identify VPT on a single microgel particle. The numerical computation of trap stiffness with respect to the factors responsible for the identification of VPT using OT is discussed in the second part of the chapter.

## 3.1 Introduction

PNIPAM microgel particles undergo sudden change in size upon varying the temperature is known as volume phase transition (VPT). These microgel particles become pH responsive upon functionalization with acrylic acids (Aac) during synthesis and are referred to as poly (N-isopropyl acrylamide-co-acrylic acid) (PNIPAM-co-Aac) microgel particles. The disassociation constant, $pK_a$ of acrylic acid group (Aac) is ~ 4.25 [48]. At pH > 4.25, acrylic acid groups are in deprotonated condition and the residual carboxylate ion gives negative charge to PNIPAM-co-Aac particles. At pH < 4.25, Aac groups are in protonated state and particles are neutral (initiator added during synthesis gives microgel a slight negative charge). As a result, PNIPAM-co-Aac microgels are not completely thermo responsive at pH > 4.25, due to electrostatic repulsion between the deprotonated acrylic acid groups in the microgel structure. At pH < 4.25, these particles are fully thermo responsive. Because of their unique reversible thermo responsive property, PNIPAM microgel particles have

emerged as an important building blocks for studying basic phenomena like crystallization, glass transition [132], sensing [52], chemical separation and drug delivery [53]. Monodisperse PNIPAM microgel particles self-assemble into ordered structures and are popularly known as tunable photonic crystals as their lattice constant is tunable using stimuli such as temperature and pH [24].

Many of the above mentioned applications require knowledge about VPT induced either by varying temperature (*T*) or pH. Dynamic light scattering (DLS) is the conventional technique to determine VPT of the microgel particles [54,88]. Using DLS, particle diameter (also known as hydrodynamic diameter), *d* as a function of *T* or pH is measured and the large change in *d* occurring due to sudden deswelling of microgel particles at a critical *T* or pH is identified as VPT. However the identification of VPT using DLS requires dilute (non-interacting) suspensions with particle concentrations ~ $10^7$ particles/$cm^3$ to satisfy the Gaussian approximation underlying the Siegert's relation [86]. Using Siegert's relation, electric field autocorrelation function is obtained from the measured intensity autocorrelation function in a DLS experiment [92]. Further, DLS measurement and its analysis become complicated if samples are highly polydisperse in size [93]. The limitation in identifying the VPT accurately using DLS can be eliminated by employing optical tweezers (OT) [94,117]. It allows trapping of a single microgel particle. Optical tweezers employs tightly focused laser beam to hold microscopic particles stable in three dimensions. OT have become an indispensable tool in investigating single particle's property like refractive index [118], rigidity [119], electrophoretic forces [120] and local pH measurement in a microchip [121]. It is a non-contact and non-invasive technique and has found applications in biology [133,134] and material science. In this chapter, we report the identification of VPT of pH responsive

PNIPAM-co-Aac microgel particles using indigenously developed optical tweezers set-up, equipped with 1064 nm wavelength laser.

### 3.2. Experimental Methods

#### 3.2.1. Sample preparation

Purified suspension of PNIPAM-co-Aac microgel particles is concentrated using stirred cell and allowed to crystallize. The Bragg reflection from microgel crystals is recorded using static light scattering (SLS) technique. The first Bragg peak position $q_{111}$is used to estimate the particle concentration, $n_p$ and volume fraction, $\phi$ of the microgel crystals as described in section 2.5.1 [88]. The concentrated sample is diluted to a concentration of 2.8 $\times 10^7$ particles/cm$^3$ by adding required amount of deionized water. From DLS, the hydrodynamic diameter, $d$ and polydispersity of these microgel particles suspended in deionized water is measured to be 930 nm and 4% at 23 °C respectively. For trapping experiments, the concentrated suspension is diluted to a concentration of 3 $\times 10^6$ particles/cm$^3$ by adding required amount of pH buffers of ionic strength 15 mM.

#### 3.2.2 Optical trapping and trap stiffness analysis of PNIPAM-co-Aac microgel particles

The home built optical tweezers set-up is calibrated and tested for its functioning as described in section 2.5.7. After calibration, optical tweezers is employed to identify the VPT of a single pH responsive microgel particle as a function of pH. PNIPAM-co-Aac microgel suspension of very low concentration (~ 3 x $10^6$ particles/cm$^3$) is prepared in solutions of different pH values with constant ionic strength, is placed in a thin sample cell made up of a standard microscope glass slide

and a cover slip with a spacer of thickness about 100 μm. Synthesis and characterization of PNIPAM-co-Aac microgel particles for their average size and size distribution is described in section 2.1. The laser power used for trapping the PNIPAM-co-Aac particles of size 930 nm is kept constant at 22.5 mW at the trapping plane. The laser power is optimized such that the minimum laser power at which microgel particles in swollen state can get trapped. A single PNIPAM-co-Aac microgel particle is trapped at the focus of the laser beam and position of the trapped particle as a function of time is recorded. The trap stiffness value along *x*-direction was determined using equipartition theorem from the position data of the trapped microgel particle at pH values ranging from 3.00 to 5.00. The $\kappa_x$ value, thus determined using Eqn. (2.53), for microgel particles dispersed in pH = 3.00 solution is 1.1 ± 0.1 μN/m and that dispersed in pH = 5.00 solution is 0.5 ± 0.1 μN/m at temperature, $T$ = 23 °C.

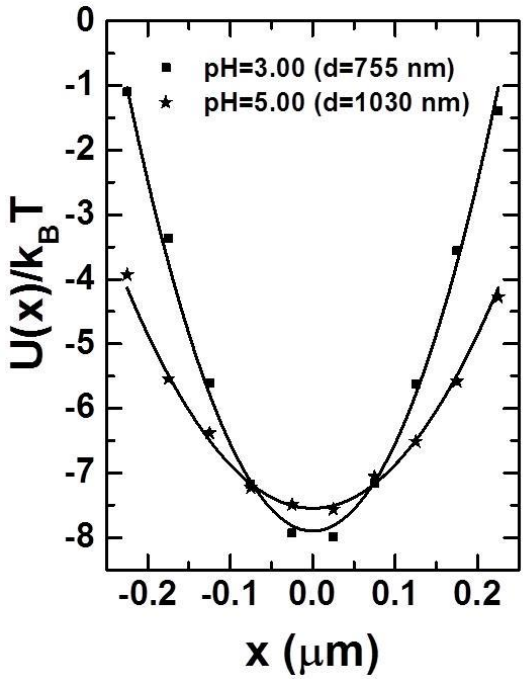


**Figure 3.1** $U(x)/k_BT$ versus displacement *x* from the mean position of the microgel particle in the optical trap at pH 3.00 and pH 5.00 at $T$ = 23 °C. Continuous lines are fit to Eqn. (2.56) for the microgel particle suspended in pH buffer solution.

The potential data $U(x)$ obtained using Eqn. (2.55) from the position data is found to fit well to Eqn. (2.56) for the range of *x* from -0.25 μm to 0.25 μm. The fit of *U(x)* data to Eqn. (2.56) is shown in Fig. 3.1, for two extreme values of pH. This implied that the potential is harmonic within the *x*-range. The stiffness constant, $\kappa_x$ determined from the fit is 1.14 ± 0.08 μN/m for the particle dispersed in buffer pH 3.00. At pH 5.00, $\kappa_x$ is determined to be 0.51 ± 0 .05 μN/m. Notice that the $\kappa_x$ values determined using optical potential analysis method agrees well with that obtained using equipartition method. At a given pH, the experiment is repeated five times, by trapping each time another microgel particle of same size (i.e., same pixel area) from the same sample and the standard deviation in $\kappa_x$ is denoted as error bars.

### 3.2.3 Computation of trap stiffness

The trap stiffness constant, $\kappa_x$ was computed using the "Optical tweezers computational toolbox (OTCT)" software developed by Nieminen *et. al.*, [135]. OTCT is used for computing optical forces and torques for both spherical and non-spherical particles. OTCT software computes optical trapping efficiency, *Q* based on T-matrix method. T-matrix relates the incident and scattered fields and it depends only on the properties of the particle and the wavelength of the laser. Here, we assume the microgel particle to be homogeneous with refractive index, $\mu_p$ which is expected to vary with particle size. This assumption is reasonable for PNIPAM-co-Aac particles, as the hairy shell is much smaller (< 3%) than the size of the core [59]. The computation of $\kappa_x$ using OTCT requires inputs such as refractive index of the particle, $\mu_p$ size of the particle, *d* refractive index of the medium, $\mu_m$ wavelength of incident radiation, $\lambda$ and laser power, *P*. The refractive index, $\mu_p$ of the microgel particles has been determined by measuring the refractive index of the suspension, $\mu_s$ and the

refractive index of the medium, $\mu_m$ at each value of pH using Abbe's refractometer at a fixed temperature, 23 °C. Since the volume fraction, $\phi$ (Eqn. 2.36) is known at each value of pH, we could estimate $\mu_p$ using the relation**,**

$$\mu_s = \mu_m + \phi(\mu_p - \mu_m)F \tag{3.1}$$

and *F* is related to van de Hulst [136] complex forward scattering amplitude $S(0)$ and can be approximated to the empirical expression of the form $\sin x / x$ [137]. Here, *x* is the size parameter and is given by $x = (4.5 \times (\mu_p - \mu_m) \times d)/\lambda$. Refractive index contrast $(\mu_p - \mu_m)$ for PNIPAM-co-Aac microgel dispersions in their swollen as well as in their deswollen state is smaller than 0.025. The value of size parameter, *x* is at most 0.09 for the particle sizes reported here and hence sin *x*/*x* can be approximated to 1. Hence equation (3.1) reduces to

$$\mu_s = \mu_m + \phi(\mu_p - \mu_m) \tag{3.2}$$

and has been used to calculate the refractive index of the particle, $\mu_p$.

### 3.3 Results and Discussion

#### 3.3.1 VPT using DLS

In order to study the pH response of PNIPAM-co-Aac particles, we carried out DLS studies on these particles in dilute conditions ($n_p$~$10^7$ particles/cm$^3$) and measured hydrodynamic diameter, *d* as a function of pH, is shown in Fig. 3.2. Figure 3.2 shows increase of *d* below and above pH ~ 4.25 with a sudden increase in *d* at pH ≈ 4.25. The sudden rise in *d* at pH ~ 4.25 is identified as VPT. PNIPAM-co-Aac microgel particles will be in their deswollen state at low pH due to complete protonation of acrylic acid groups on the polymer chains. At high pH, acrylic acid

groups get deprotonated and it leads to the electrostatic repulsion between polymer chains in the microgel particles [48]. The electrostatic repulsion between charged polymer chains leads to swelling (*i.e.*, increase in size) of the particles. Most of the Aac groups on the polymer chains undergoes deprotonation at pH ≥ 4.25, leading to increased electrostatic repulsion between negatively charged polymer chains. The increased repulsion results in sudden increase in particle swelling. The pH response of these microgel particles (reported in Fig. 3.2) is consistent with the results reported in the literature [3].

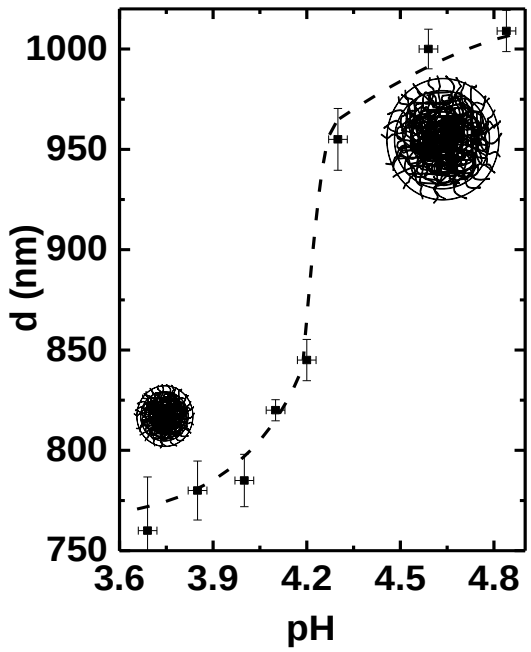


**Figure 3.2** Hydrodynamic diameter, *d* of microgel particles versus pH measured using DLS. Inset shows schematic of de-swollen and swollen microgel particles at pH below and above VPT, respectively. Dashed line is the guide to the eye.

Refractive index of the particle, $\mu_p$ is estimated as a function of pH using Eqn. (3.2). Figure 3.3 shows the variation of $\mu_p$ as a function of pH. Notice that, $\mu_p$ shows a sudden decrease at VPT, where particle undergoes sudden swelling at pH ≥ 4.25. In the swollen state, PNIPAM-co-Aac microgel particles contain more than 97% water [59,62]. Hence the refractive index of the particle, $\mu_p$ is close to that of water.

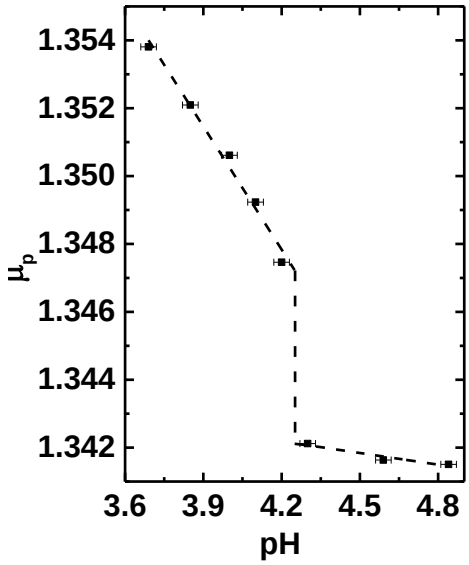


**Figure 3.3** Measured microgel particle refractive index, $\mu_p$ as a function of pH. Dashed line is guide to the eye.

### 3.3.2 Trap stiffness: Experiment and computation

We employed the following methodology, to ensure a single particle alone was there in the trap. We have taken suspension with very low concentration of microgel particles (i.e. particle concentration of ~ 3 x $10^6$ particles/$cm^3$). After completing the experiment at a given pH, we de-trap the particle(s) by blocking trapping beam and monitored carefully the particles diffusing from the trap is single or not. In measurements reported here we never observed more than one particle diffusing out from the trap. We numerically computed (using OTCT software) trap stiffness value for a single particle and compare with that measured using optical tweezers. This is described in the later part of this chapter.

Notice in Fig. 3.4, $\kappa_x$ showing a sharp change at pH ~ 4.25, as compared to DLS data (Fig. 3.2), suggesting that the VPT in pH responsive microgel particle is a first order transition, in accordance with predictions of extended Flory-Huggins swelling theory [138].

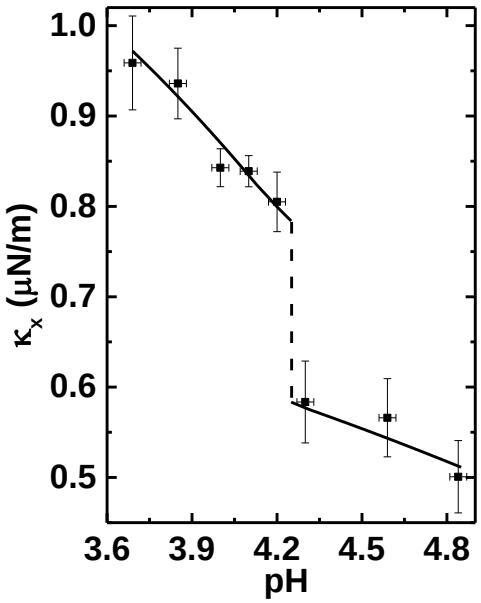


**Figure 3.4** Trap stiffness, $\kappa_x$ measured as a function of pH on a single microgel particle using optical tweezers. Continuous line denotes the numerically computed, $\kappa_x$ using OTCT. Dashed line represents sudden change in $\kappa_x$ occurring at VPT.

Though DLS also shows sudden change in particle size at VPT ~ pH = 4.25 (Fig. 3.2), there exists smearing in DLS data and is attributed to large number of particles with different sizes (size polydispersity 4%) involved in the measurement [138]. Since optical tweezers facilitate the measurement of $\kappa_x$ on a single trapped particle, identification of VPT is unambiguous even if suspensions are highly polydisperse in size. With an aim to understand the observed $\kappa_x$ dependence on pH and to identify the particle parameters that are responsible for a sharp change in $\kappa_x$ at VPT, we have numerically computed optical trap stiffness constant, $\kappa_x$ for different values of pH. Particle diameter, $d$ (Fig. 3.2) and refractive index of the particle, $\mu_p$ (Fig. 3.3) measured as a function of pH are given as inputs for computing $\kappa_x$. The continuous line in Fig. 3.4 shows the computed $\kappa_x$ as a function of pH. There is an excellent agreement between computed $\kappa_x$ and that measured using optical tweezers. The agreement is obtained by scaling the computed $\kappa_x$ by a factor of 0.65 to match

with the experiment. OTCT computes trapping efficiency, $Q$ and when multiplied with $\mu_m P/c$ ($\mu_m$ denotes the refractive index of the medium and $c$ is velocity of light) gives trap stiffness $\kappa_x$ in units of N/m [135]. Here the difficulty to measure the laser power, $P$ at the focal spot with the sample in place, necessitates scaling of computed data to match with the experimental data [124].

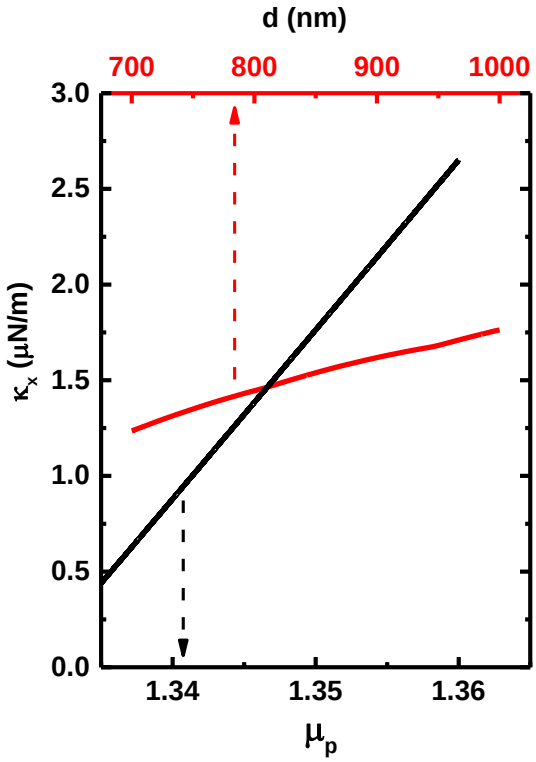


**Figure 3.5** Computed $\kappa_x$ as a function of refractive index of the particle, $\mu_p$ with $d$ = 1 μm (black line) and size of the particle, $d$ with $\mu_p$ = 1.35 (red line).

We have computed $\kappa_x$ by varying particle diameter, $d$ keeping the refractive index, $\mu_p$ fixed and vice versa, and it is shown in Fig. 3.5. Notice that $\kappa_x$ shows a linear increase with $d$ as well as $\mu_p$. The OTCT software developed by Niemann *et. al.*, for computing the trapping forces is mainly for the sizes lying within the gap between region of applicability of small particle approximation (Rayleigh limit, EM model) and large particle approximation (RO limit). Thus, the linear dependence of

trap stiffness with size is in accordance with expected scaling [123]. We have calculated (using OTCT software), change in $\Delta\kappa_x$ due to change (increase) in size $\Delta d = 118\,nm$ (occurring at VPT) (keeping refractive index fixed) and change in $\Delta\kappa_x$ due to change in (decrease) refractive index, $\Delta\mu_p = 5.54 \times 10^{-3}$ (keeping size fixed) and found to be $\Delta\kappa_x = 0.15\,\mu N/m$ (increases) and $0.49\,\mu N/m$ (decreases) respectively.

The variation in $\kappa_x$ with $\mu_p$ is much steeper than with $d$ (Fig. 3.5). It is clear that the changes in trap stiffness due to changes in size and refractive index are not compensated by each other. In fact the change in trap stiffness occurring due to change in refractive index is ~ 3.3 times more than that occurring due to change in size. Upon increasing pH, at VPT PNIPAM-co-Aac particles not only undergo size increase (swelling) $\Delta d = 118\,\text{nm}$ (Fig. 3.2) but also sudden change in refractive index ($\Delta\mu_p = 5.54 \times 10^{-3}$ (Fig. 3.3). As a consequence of these changes, trap stiffness shows a sudden change of $\Delta k_x = 0.22\,\mu N/m$ (Fig. 3.4). The numerically computed change $\Delta k_x = 0.34\,\mu N/m$ across VPT is found to exactly 0.65 times than that of measured experimentally. Thus, calculations reproduce the observed jump in trap stiffness at VPT. The reason for scaling factor is essentially due to lack of direct measurement of laser power of the tightly focused beam at the focal point of the objective. Numerically computed trap stiffness, $\kappa_x$ as a function of pH is found to show linear dependence on $d$ and $\mu_p$ (Fig. 3.5) whereas experimentally measured $\kappa_x$ shows sharp decrease (Fig. 3.4) at pH = 4.25 and is understood to arise from the sudden increase in the particle diameter (Fig. 3.2) with a concomitant decrease in refractive index of the particle. When pH is varied, PNIPAM-co-Aac microgel particles not only undergo sudden swelling in size at VPT but also undergo sudden

decrease in refractive index at VPT (Fig. 3.3). This concomitant change results in sudden change in $\kappa_x$ at VPT.

### 3.4 Conclusion

In conclusion, we have designed and developed an optical tweezers set-up and successfully trapped pH responsive PNIPAM-co-Aac microgel particles. The synthesized microgel particles were characterized for their VPT induced by pH using a DLS set-up which requires particle concentration of the order of $10^7$ particles/cm$^3$. It is also shown for the first time that VPT of a single PNIPAM-co-Aac particle can be identified unambiguously by using optical tweezers. Measured optical trap stiffness constant $\kappa_x$ showed a sharp change at VPT (pH = 4.25) as compared to size change measured by DLS. Optical tweezers measurements are in accordance with the model predictions [138]. Thus, optical tweezers serves as an appropriate research tool to study phase transitions in stimuli responsive microgels and also offer additional advantage of using samples of particles even with wide size distribution. We have also shown a good agreement between numerically computed trap stiffness constant with that measured by optical tweezers. By analyzing the computed optical trap stiffness data for particles of varying size and refractive index, we concluded that the sharp change in lateral trap stiffness at VPT is due to the sudden swelling of microgel particle with concomitant sharp decrease in refractive index occurring at pH = 4.25.

# CHAPTER 4

# FCC-HCP COEXISTENCE IN DENSE THERMO-RESPONSIVE MICROGEL CRYSTALS

This chapter deals with the determination of crystal structure of osmotically compressed microgel crystals using SLS and UV-Vis spectroscopy. The influence of entanglement of dangling polymer chains on the structure of microgel crystals is discussed. The effect of cooling rate on the structure of microgel crystals is studied and reported here.

## 4.1 Introduction

Colloidal crystals of hard spheres often co-exist in closely related polymorphs (FCC and HCP structures) due to free energy difference between these structures being less than thermal energy [35,36,139], $k_BT$. FCC-HCP coexistence in hard sphere colloidal crystals at a volume fraction, $\phi$ greater than 0.5 has been reported and well-studied [38]. Computer simulations have predicted that these coexisting structures transform to their equilibrium structure, *i.e*., FCC structure on time scales of months [39]. Crystal growth rate [37,140] and slow dynamics [141] are also known to influence the structure formation in colloidal crystals. Unlike hard spheres, stimuli responsive microgels are soft and respond to external stimuli like temperature, pH, ionic strength, etc., by undergoing swelling/de-swelling. This results in not only size change but also change in the interaction potential [56,57], hence their phase behaviour [54]. Among several stimuli responsive microgel systems, poly(N-isopropyl acrylamide) (PNIPAM) microgel particles in aqueous medium is well-studied for its phase behaviour as a function of temperature (*T*) and volume fraction

($\phi$) [92]. PNIPAM microgel particles are known to have dense core and a thin shell (~ 20 to 30 nm) in the form of dangling chains (hairs) [59,62]. Upon increasing the temperature, core undergoes more de-swelling than the shell [59] and exhibit a sudden collapse in size at 34 °C, which is known as volume phase transition (VPT) [54,92]. This variation in size and associated change in the interparticle interaction are responsible for the rich phase behaviour of PNIPAM microgel suspension [57].

Soft and deformable nature of PNIPAM microgels enable them to pack to a volume fraction greater than cubic closed packed limit ($\phi = 0.74$) [56]. Upon packing them beyond 0.74, these particles are known to undergo de-swelling due to osmotic pressure exerted by surrounding particles in an ordered state [78,142]. Hereafter, these PNIPAM microgel crystals with de-swollen particles due to osmotic compression by surrounding particles are referred as osmotically compressed crystals. Dense suspensions of PNIPAM microgel particles with low cross-linker density are known to freeze into an FCC structure at $\phi < 0.74$, [54,57,110,113,143] analogous to that of hard spheres. However, crystal structure of PNIPAM microgels with volume fraction, $\phi > 0.74$ has not been well studied.

Here, we report the structure of dense microgel crystals with PNIPAM particles in their swollen state ($\phi < 0.74$, referred to as low volume fraction sample) and osmotically compressed state ($\phi > 0.74$, referred to as high volume fraction sample), as probed by light scattering and UV-Visible spectroscopy technique. Under as prepared conditions, low volume fraction samples showed FCC-HCP coexistence whereas the high volume fraction sample showed glass-like disorder. In order to find the equilibrium structure of these PNIPAM samples, detailed annealing studies with different cooling rates have been carried out and the results are reported in this

chapter. Upon annealing, recrystallized sample with $\phi < 0.74$ showed FCC structure, whereas sample with $\phi > 0.74$ showed stable FCC-HCP co-existence. FCC-HCP coexistence in PNIPAM microgel crystal with $\phi > 0.74$ is due to the overlap (entanglement) of dangling chains between shells of neighbouring PNIPAM microgel particles and is confirmed through the analysis of dynamic light scattering data and annealing studies.

## 4.2 Experimental methods

### 4.2.1 Sample preparation

PNIPAM microgel suspensions of particle size 235 nm (small size) and 633 nm (large size) synthesized as described in section 2.1 are used for the current study. Purified PNIPAM microgel suspensions are concentrated using a stirred cell. During the course of concentration, samples with different concentrations have been collected. For the present investigations, four samples of PNIPAM microgel suspensions with different volume fractions (two samples of small sized particle and two samples of large sized particle) have been used. Low volume fraction sample of large size particles is labeled as 'LB' and high volume fraction sample of large size particles is labeled as 'HB'. Similarly, low volume fraction suspension of small particles is labeled as 'LS' and that with high volume fraction as 'HS'. The crystallization procedure for the four samples is described in the later part of this chapter and further details about these samples are listed in Table 4.1.

### 4.2.2 Dynamic light scattering

Particle size measurement in dilute suspension and dynamics of particles in dense suspension are measured using dynamic light scattering technique. In turbid

samples, 3D-DLS is used to measure dynamics of particles to avoid the influence of multiple scattering of light. Dynamics in glass-like sample is measured by non-ergodic analysis method as proposed by Pusey and Van megan [106]. The variation of hydrodynamic diameter, $d$ as a function of temperature, $T$ for both PNIPAM suspensions is shown in Fig. 4.1. Both samples showed sudden collapse in particle size at 34 °C and is identified as volume phase transition (VPT) [92].

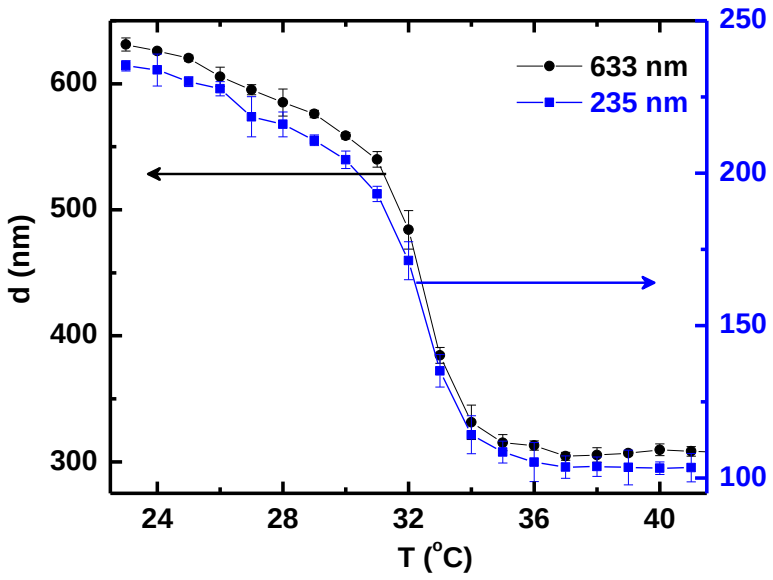


**Figure 4.1** Hydrodynamic diameter ($d$) versus temperature ($T$) measured on dilute PNIPAM microgel suspension of two different sizes using DLS. Continuous lines are guide to eye.

### 4.2.3 Static light scattering

In order to characterize structural ordering in PNIPAM microgel suspensions, SLS has been used to measure the scattered intensity $I_s(q)$ as a function of $q$. To record Bragg peaks from crystallites with different orientations in the sample, the cylindrical sample cell is rotated about its vertical axis at a slow speed (0.6 rotations per minute) [103]. The recorded diffraction pattern is analyzed to identify the crystal structure of PNIPAM microgel crystals which are known to exhibit FCC or HCP or RHCP structure [70]. For an FCC structure, the first Bragg peak in the diffraction

pattern is from (111) planes and other allowed Bragg peak positions for FCC structure have been calculated using the position of $q_{111}$ peak as described in section 2.5.1. Similarly, for HCP structure the first peak corresponds to Bragg reflection from (100) planes and other allowed peak positions for the HCP structure are calculated using the position of $q_{100}$ peak. The structure of PNIPAM microgel crystal is identified to be FCC/HCP or FCC-HCP coexistence by calculating all the Bragg peak position for the structure and matching with that measured experimentally.

### 4.2.4 UV-Visible spectroscopy

Concentration (*i.e.*, particle number density, $n_p$) of sample LS and HS are more as compared to that of sample LB and HB. The first diffraction peak from sample LS and HS lies outside the scattering wave vector range, *i.e.*, $q$-range of our static light scattering (SLS) setup. Hence, the diffraction pattern of these crystals could not be recorded using SLS. However, UV-Visible spectroscopy has been used to identify the crystal structure of sample LS and HS by recording the absorption spectra and the details are given below. All UV-Visible measurements have been carried out in transmission geometry under normal incidence mode. Sample is heated to required temperature with an accuracy of ± 0.1 °C using a peltier element attached to the sample. The dense plane, (111) of the FCC structure and (002) of HCP structure are known to grow parallel to the walls of the sample cell [70,113]. Prominent peaks in absorption spectra correspond to (111) peak of FCC structure or (002) peak of HCP structure. Volume fraction, $\phi$ and nearest-neighbour separation, $d_{nn}$ values of sample LS and HS have been determined using the λ values correspond to Bragg peaks in the absorption spectra. Table 4.1 summarizes sample details, equilibrium structure of

PNIPAM microgel suspension determined using UV-Visible and SLS techniques before and after annealing.

**Table 4.1** Sample details and the crystal structure of PNIPAM microgel crystals before and after annealing.

| **Sample label** | ***d*(nm) at 22 $^{o}$C** | $\boldsymbol{\phi}$ | $\frac{d_{nn}}{d}$ | **Structure at 22 $^{o}$C (As prepared)** | **Cooling rate ($^{o}$C/hour)** | **Stable structure at 22 $^{o}$C** |
|---|---|---|---|---|---|---|
| LS | 235 | 0.54 | 1.10 | FCC-HCP | 0.5 | FCC |
| HS | 235 | 0.89 | 0.93 | Disordered (glass like) | 1 | FCC-HCP |
| | | | | | 0.3 | FCC-HCP |
| | | | | | 0.1 | FCC-HCP |
| LB | 633 | 0.47 | 1.16 | FCC-HCP | 0.5 | FCC |
| HB | 633 | 0.79 | 0.97 | Disordered (glass like) | 0.5 | FCC-HCP |
| | | | | | 0.3 | FCC-HCP |
| | | | | | 0.1 | FCC-HCP |

## 4.3 Results and discussion

### 4.3.1 Structural ordering of low volume fraction sample

Two samples with volume fraction close to 0.5 using large (*d* = 633 nm) and small (*d* = 235 nm) size PNIPAM microgel particles, by loading the suspensions into cylindrical light scattering cell of diameter 5 mm and into a thin UV-Vis cuvette with 100 µm groove, respectively were prepared for investigating the structural ordering. The samples were left undisturbed for over 24 hours. These samples are referred to, as prepared samples and showed iridescence suggesting the crystallization of PNIPAM microgel spheres in the sample cells. Bragg diffraction from these PNIPAM microgel

crystals were recorded using light scattering and UV-Vis spectrometer and are shown in Fig. 4.2(a) and Fig. 4.3(a), respectively. Notice in Fig. 4.2(a), that the measured diffraction pattern for sample LB agree well with that calculated for an FCC and HCP coexisting structure. Sheer presence of peaks which are inherent to FCC ((200)) and HCP ((100), (101), (103)) structures confirm that the structure is FCC-HCP coexistence [144,145]. The volume fraction, $\phi$ and nearest-neighbour distance, $d_{nn}$ determined using the first peak position for sample LB are 0.47 and 737 nm respectively. Note that $d_{nn}/d$ is greater than 1 (see Table 4.1) which suggests that PNIPAM microgel particles are in their swollen state at $\phi = 0.47$.

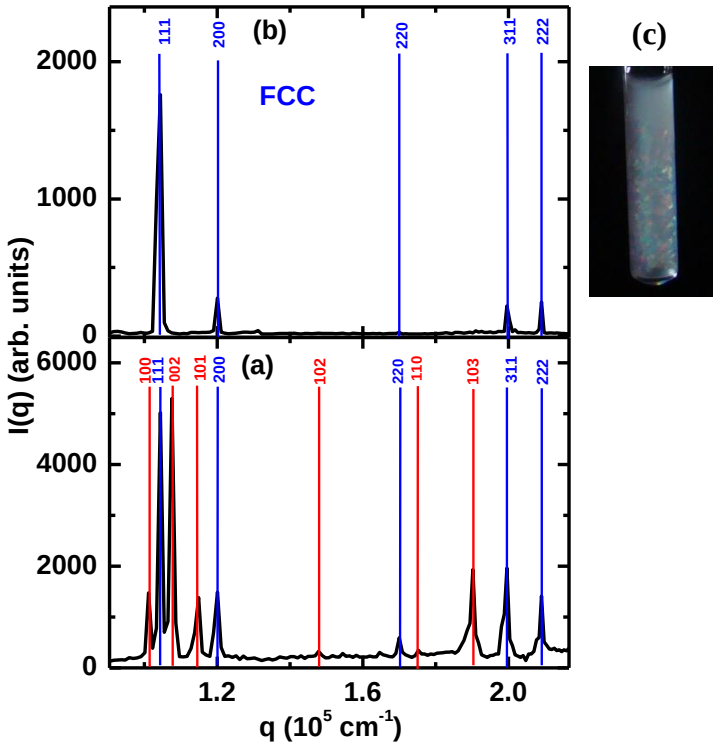


**Figure 4.2** Bragg diffraction pattern of sample LB (a) as prepared (b) recrystallized (upon annealing with a cooling rate of 0.5 °C/hour) recorded using SLS at 22 °C. Vertical lines indicate the Bragg peak positions corresponding to ideal FCC and HCP structure with $\phi = 0.47$ (c) photograph showing iridescence in sample LB after annealing.

FCC-HCP coexistence observed in sample LB is consistent with earlier report by Brijitta *et. al.*, [70] using confocal microscopy. As prepared sample was annealed

by raising the sample temperature to 35 ºC (above VPT) and keeping it at that temperature for 1 hour and then slowly cooling it to room temperature (22 ºC) with a cooling rate of 0.5 ºC/hour. The sample was recrystallized and exhibited iridescence. Bragg diffraction pattern of the re-crystallized sample is shown in Fig. 4.2(b). Notice the absence of prominent diffraction peaks ((100), (002), (101), (103)) of HCP. The presence of ((111), (200), (311)) peaks of FCC (Fig. 4.2(b)), confirm that FCC-HCP coexistence observed under as prepared conditions has transformed to FCC structure upon annealing.

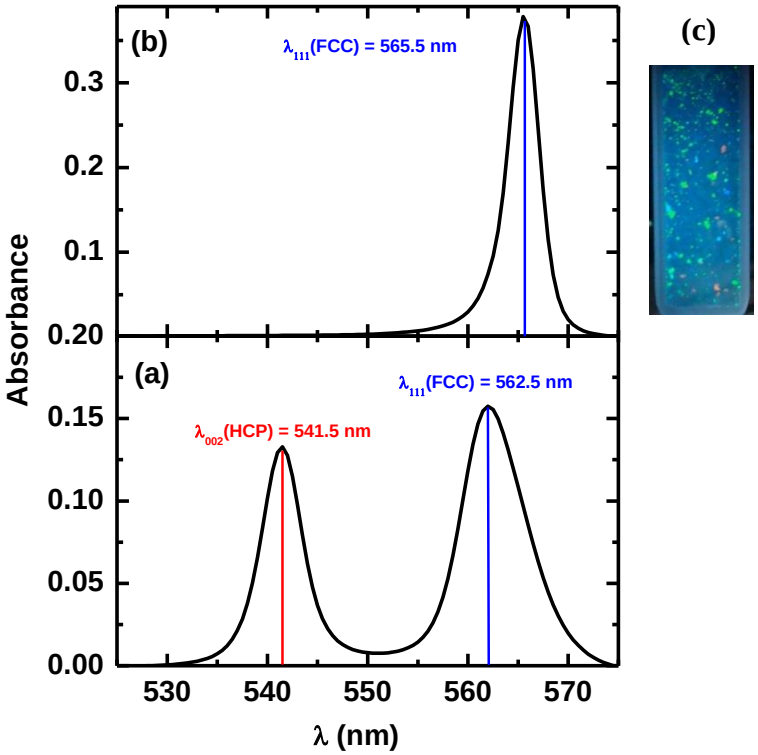


**Figure 4.3** Absorbance spectra of (a) as prepared and (b) recrystallized (upon annealing with a cooling rate 0.5 °C/hour) sample LS recorded at 22 °C. Vertical lines indicate Bragg peak positions corresponding to (002) and (111) reflection from HCP and FCC structure respectively (c) photograph of crystallized sample of LS showing iridescence after annealing.

UV-Visible spectrometer, where we sweep λ, keeping the glancing angle fixed at $\theta = 90^{\circ}$, have been used to record the absorption spectra from sample LS and are shown in Fig. 4.3. Absorption peaks at 514.5 nm and 562.5 nm (Fig. 4.3(a)) are

identified as (002) and (111) Bragg reflections from PNIPAM microgel crystals with HCP and FCC structures respectively. The volume fraction, $\phi$ determined from these peak positions is found to be $0.54$. The sample upon annealing at 35 ºC and cooled to 22 ºC with a cooling rate of 0.5 ºC/hour showed a single Bragg peak correspond to (111) peak of FCC structure. Thus, PNIPAM microgel crystals with volume fraction, $\phi = 0.54$, exist in FCC-HCP coexistence structure under as prepared condition and transformed to FCC structure upon annealing. Thus, equilibrium structure of PNIPAM microgel crystals with volume fraction, $\phi < 0.74$ is observed to be FCC and is consistent with results reported earlier [70] and also similar to that reported on hard sphere colloidal crystals [37].

### 4.3.2 Melting of low volume fraction sample

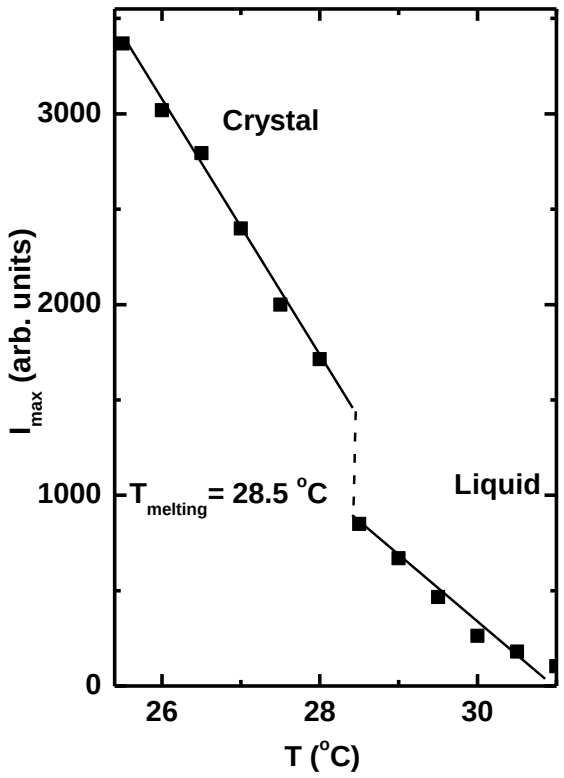


**Figure 4.4** Bragg peak intensity, $I_{max}$ of sample LB as a function of *T*. Continuous lines are guide to the eye. Dotted line indicates the melting temperature of microgel crystals.

Melting of PNIPAM microgel crystals was identified by monitoring Bragg peak intensity, $I_{max}$ at $q$ = 1.04 × $10^5$ $cm^{-1}$ as a function of temperature as shown in Fig. 4.4 using SLS. Bragg peak intensity, $I_{max}$ decreased as the temperature was increased. At each temperature, the sample was equilibrated for 10 mins and the Bragg peak intensity, $I_{max}$ was measured. At $T$= 28.5 °C sudden decrease in $I_{max}$ is identified to be the melting temperature, $T_m$ of sample LB [54]. Beyond this temperature, measured I($q$) as a function of $q$ showed a broad peak indicating the liquid like ordering in the sample. The peak position shifts by 0.4 degree upon melting which is negligible.

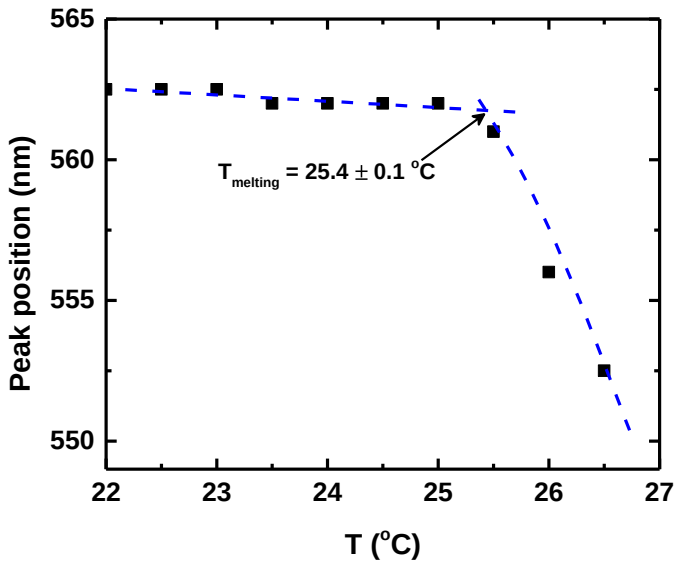


**Figure 4.5** Bragg peak position as a function of *T* recorded for sample LS. Dotted lines are guide to the eye.

In order to identify the melting temperature of sample LS, absorbance spectra of sample LS as a function of temperature, $T$ was measured. Wavelength of peak position as a function of $T$ was shown in Fig. 4.5. Notice at $T$ = 25.4 °C, large deviation in the peak position is identified as the melting point, $T_m$ of sample LS [109]. The change in the peak position is ascribed to the fact that as the temperature of

the suspension is increased, size of the PNIPAM particles decreases and in order to maintain the osmotic pressure of the crystallites, interplanar distance decreases which results in change in the peak position [109].

### 4.3.3 Structural ordering of high volume fraction sample

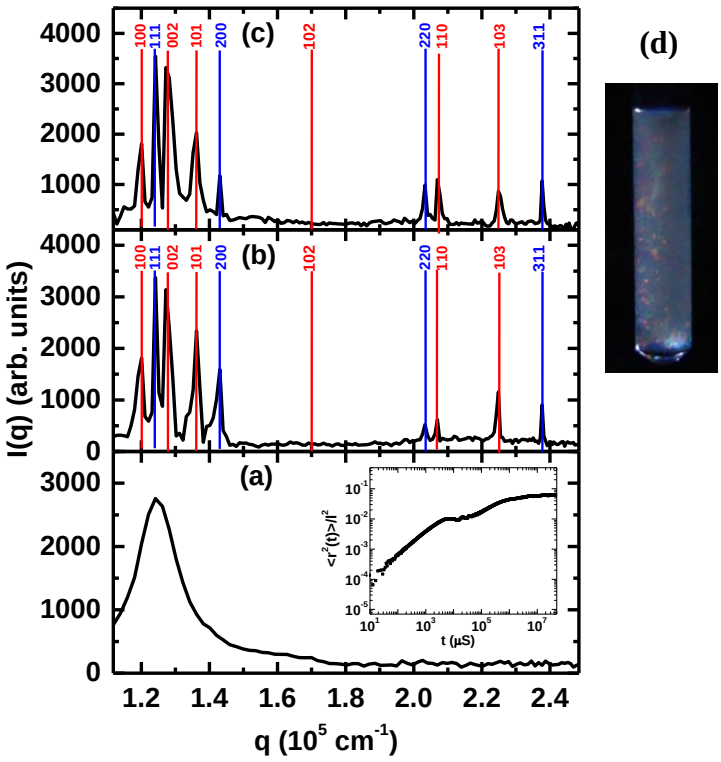


**Figure 4.6** Bragg diffraction pattern of sample HB recorded using SLS. (a) As prepared, and recrystallized sample cooled at the rate of (b) 0.5°C/hour (c) 0.1°C/hour. Inset in (a) is the mean square displacement of these particles as a function of time. (Vertical lines indicate the Bragg peak positions corresponding to ideal FCC and HCP structures) (d) Photograph recrystallized of sample HB showing iridescence.

Unlike hard spheres, PNIPAM microgel particles are soft and deformable. Hence, the suspension can be concentrated to a volume fraction greater than 0.74 [56]. Light scattering [3], small angle neutron scattering [73] and UV-visible spectroscopy [56] techniques have been used in the past to study the structure of dense microgel suspensions, which are concentrated to a volume fraction beyond 0.74. These studies

have provided evidence that PNIPAM particles undergo de-swelling (compression) due to osmotic pressure exerted by surrounding PNIPAM spheres [78,142].The nearest-neighbour separation, ($d_{nn}$) measured in the crystalline state is reported to be less than the hydrodynamic diameter, ($d$) measured using DLS under dilute conditions [146]. Further, from our own group, Joshi & co-workers have reported existence of overlap of dangling polymer chains between neighbouring particles leading to sub-diffusive behavior at short times [88] in osmotically compressed microgel crystals (*i.e.*, $\phi > 0.74$). Thus, there exists enough evidence in the literature, for deswelling of PNIPAM microgel spheres under osmotic compression and for existence of entanglement (overlap) of dangling polymer chains between neighbouring spheres. However, the equilibrium structure of osmotically compressed PNIPAM microgel crystals with $\phi > 0.74$ has not been well studied.

Here, we report light scattering and UV-Visible spectroscopy studies on osmotically compressed PNIPAM microgel crystals and show that FCC-HCP coexistence is their stable structure. Towards that two samples, HB and HS with $\phi > 0.74$ were prepared in light scattering cell and UV-Vis cuvette, respectively. As prepared sample HB showed no iridescence. Scattering profile measured using SLS showed a broad peak which is shown in Fig. 4.6(a). These observations suggest that structural ordering of PNIPAM spheres in sample HB is disordered (i.e., liquid-like or glass-like). The mean squared displacement (MSD vs $t$) obtained from ensemble averaged $f(q,t)$ showed saturation at long times (inset Fig. 4(a)) which confirms that the disorder is glass-like. Thus, sample HB under as prepared conditions exists in a glassy state. Upon annealing at 35 °C and cooled to room temperature (22 °C) with a cooling rate of 0.5 °C/hour, sample showed iridescence under white light illumination which suggest that sample HB has transformed from glass-like to crystalline upon

annealing. Diffraction pattern measured using SLS is shown in Fig. 4.6(b). It can be seen from Fig. 4.6(b) that measured diffraction peaks match well with that calculated for a FCC-HCP coexistence with volume fraction, $\phi = 0.79$. The corresponding nearest-neighbour separation, $d_{nn}$ is found to be 620 nm which is smaller than the hydrodynamic diameter $d$ = 633 nm. This clearly shows PNIPAM particles undergo osmotic compression upon concentrating the sample beyond cubic closed pack limit, $\phi = 0.74$. The sample was annealed further with slow cooling rate of 0.1 °C/hour and found that the sample remain in FCC-HCP coexistence (Fig. 4.6(c)).

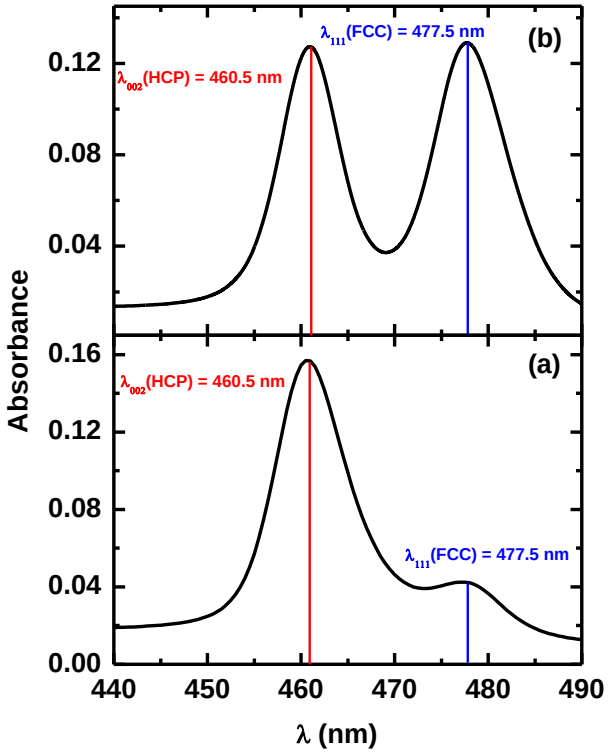


**Figure 4.7** Absorbance spectra of high volume fraction sample HS cooled at (a) 0.5°C/ hour (b) 0.1°C/hour. Vertical lines indicate Bragg peak positions corresponding to (002) and (111) reflection from HCP and FCC structure respectively.

As prepared sample, HS also showed glass-like disorder similar to that of sample HB. When annealed with a cooling rate of 0.5 °C/hour, the recrystallized sample at 22 °C showed iridescence. Absorption spectra of recrystallized sample

showed Bragg peaks at λ = 460.5 nm and 477.5 nm (Fig. 4.7(a)) correspond to (002) and (111) Bragg reflections of HCP and FCC structure, respectively. The volume fraction, $\phi$ and nearest-neighbour distance, $d_{nn}$ determined using these Bragg peak positions are given in Table 4.1. Notice that $d_{nn}/d < 1$, suggesting that particles have undergone osmotic compression when concentrated to $\phi = 0.93$. The melting point of these crystals is found to be 31 ºC [109]. The sample when annealed once again with a cooling rate of 0.1 °C/hour was found to recrystallize into an FCC-HCP co-existence with increased intensity of (111) peak (Fig. 4.7(b)) as compared to that corresponding to a cooing rate 0.5 °C/hour. Hence, we conclude that osmotically compressed PNIPAM microgel crystals with $\phi > 0.74$ crystallizes into a stable FCC-HCP coexistence state.

### 4.3.4 Melting of high volume fraction sample

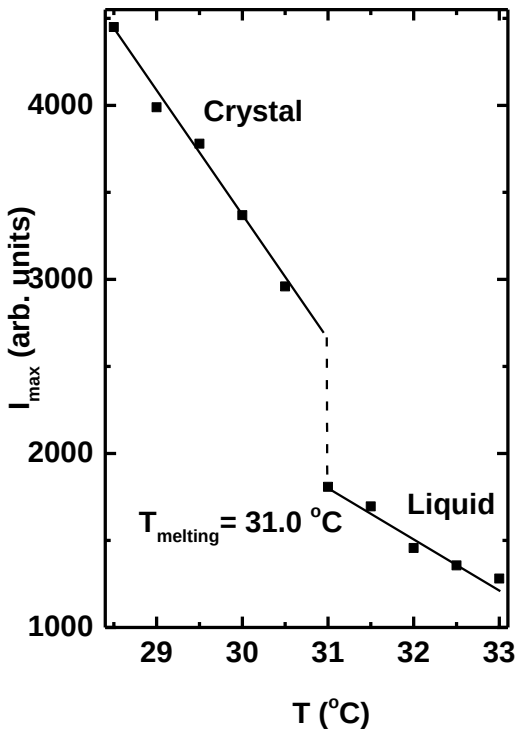


**Figure 4.8** Bragg peak intensity, $I_{max}$ of sample HB as a function of *T*. Continuous lines are guide to the eye. Dotted line indicates the melting temperature of microgel crystals.

The melting temperature, $T_m$ of sample HB is identified by monitoring Bragg peak intensity at $q$ = 1.24 × $10^5$ $cm^{-1}$ as a function of temperature, $T$. At $T$ = 31 °C, sudden decrease in $I_{max}$ is identified as melting temperature of HB sample as shown in Fig. 4.8. Melting of sample HS is identified by monitoring the absorbance spectra as a function of $T$.

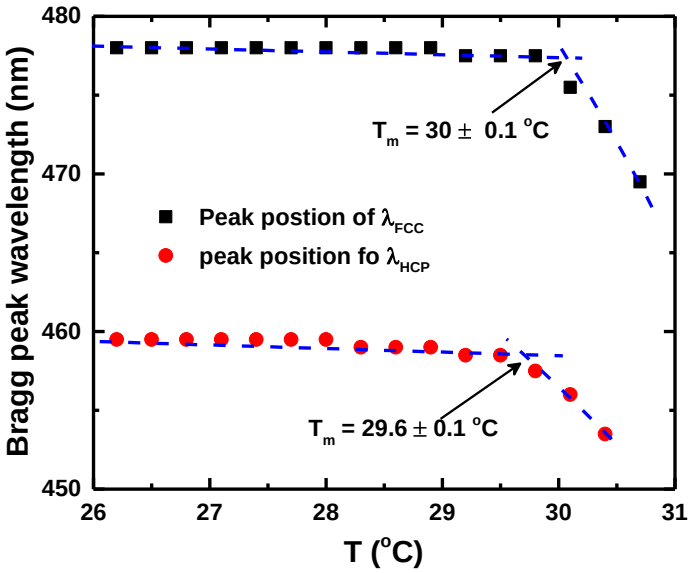


**Figure 4.9** Bragg peak position as a function of $T$ recorded for sample, HS. Dotted lines are guide to the eye.

Bragg peak position as a function of $T$ is plotted and the temperature where large deviation in peak position was observed is identified as the melting temperature, $T_m$ of sample HS (Fig. 4.9). Notice in Fig. 4.9, the peak corresponding to HCP structure started to melt at 29.6 °C whereas the peak corresponding to FCC structure started to melt at 30 °C suggesting that FCC structure is more stable compared to that of HCP structure, consistent with literature [35,36,139].

### 4.3.5 Sub-diffusive behaviour and role of entanglement

In order to understand the reason for the observed FCC-HCP coexistence in osmotically compressed PNIPAM microgel crystals with $\phi > 0.74$, we carried out

detailed DLS studies at room temperature (22 ºC) as well as at temperatures elevated above the melting point, $T_m$. Joshi *et. al.*,[88] have shown that dynamics in osmotically compressed PNIPAM microgel crystals ($\phi > 0.74$) is sub-diffusive at short times and arises due to entanglement of dangling polymer chains between the shells of neighbouring microgel spheres. The entanglement is absent in microgel crystals with nearest-neighbour separation ($d_{nn}$) being greater than the hydrodynamic diameter (*i.e.*, $d_{nn}/d > 1$).

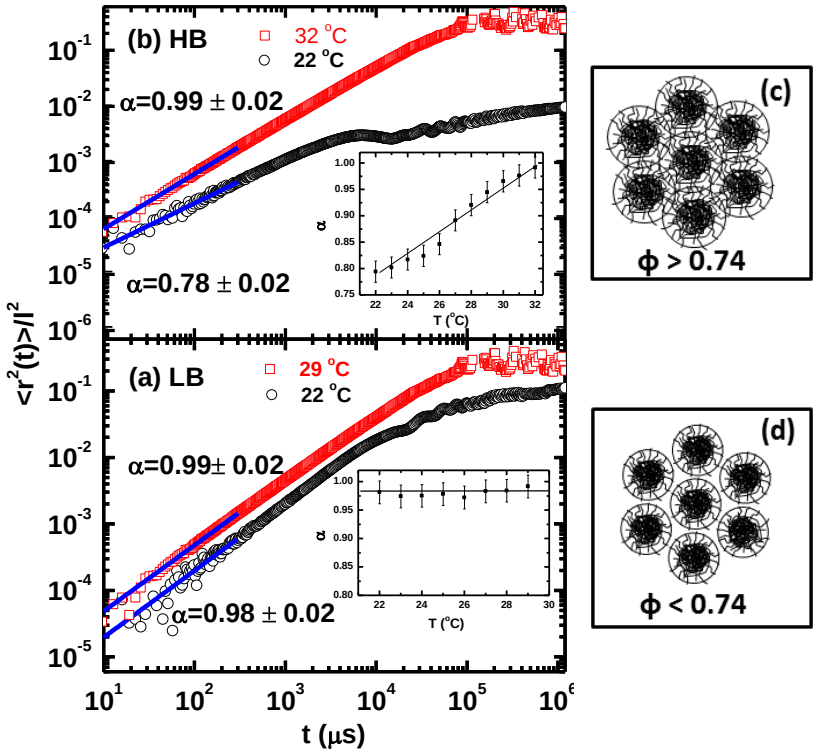


**Figure 4.10** Mean square displacement in units of average inter-particle separation, $l = n_p^{-1/3}$ versus time in PNIPAM microgel (a) sample LB (b) sample HB before and after melting. Lines represent the fit to Eqn. (2.28) at short time regime. Insets in (a) & (b) correspond to variation of α as a function of T. Continuous lines drawn in the inset are guide to eye. Schematic picture depicting core-shell nature of PNIPAM spheres with entanglement of dangling chains between neighbouring spheres (c) and with no entanglement (overlap) (d).

In order to verify the presence of entanglement in the samples, we carried out DLS studies on sample LB as well as on sample HB at two different temperatures and

mean square displacement (MSD) as a function of time obtained from DLS measurement using Eqn. (2.28) are shown in Fig. 4.10. Notice that dynamics at short times [88] is diffusive ($\alpha \approx 1$) in sample LB both in the crystalline regime (i.e., before melting at $T$ = 22 ºC) as well as in the liquid regime (i.e., after melting, $T$ = 29 ºC). The melting temperature of PNIPAM microgel crystal of sample LB and HB are identified to be $T_m$ = 28.5 ºC and 31 ºC respectively, by monitoring the Bragg peak as a function of temperature [92]. Time exponent, $\alpha$ obtained by fitting the short time MSD data to Eqn. (2.28) at different temperatures is shown in inset of Fig. 4.10(a). Short time of MSD have been identified using $\tau_R$ (cage rearrangement time) as a reference point. $\tau_R$, determined from $d_h^2/D_0$, with $D_0$ is the free diffusion coefficient. For sample LB and HB, $\tau_R$ is found to be ~ 550 $\mu$s. It can be seen that short time dynamics in sample LB is diffusive ($\alpha \approx 1$) at all temperature (i.e., crystalline as well as in the liquid regime). In the case of sample HB, which exhibited FCC-HCP coexistence after annealing, the dynamics is found to be sub-diffusive ($\alpha < 1$) at short times (Fig. 4.10(b), T = 22 ºC). The observation of sub-diffusive behavior at short times in sample HB, confirms the presence of entanglement of dangling polymer chains between the shells of neighbouring PNIPAM microgel particles. Thus, the entanglement between the neighboring PNIPAM spheres is responsible for FCC-HCP coexistence in osmotically compressed PNIPAM microgel crystals.

With an aim to provide evidence that in crystals, entanglement leads to formation of HCP structures, we monitored the evolution of HCP and FCC structures upon cooling the liquid like ordered sample from above its melting temperature to different temperatures below the melting point of microgel crystals and the results are shown in Fig. 4.11. Notice that FCC structure grows in sample LS upon cooling to temperature below its $T_m$ (Fig. 4.11(a)) whereas HCP structure grows relative to FCC

in the case of HS sample (Fig. 4.11(b)). This suggests that HCP structure competes with FCC in the presence of entanglement of dangling polymer chains between shells of neighbouring particles. Mahynski *et. al*.,[147-149] have recently showed that HCP structure can be stabilized over FCC in hard sphere colloidal crystals by adding interacting polymeric chains. The free energy calculations by Edison *et. al*.,[150] also confirm that HCP phase stabilizes over FCC with the addition of polymers to hard sphere colloidal crystals.

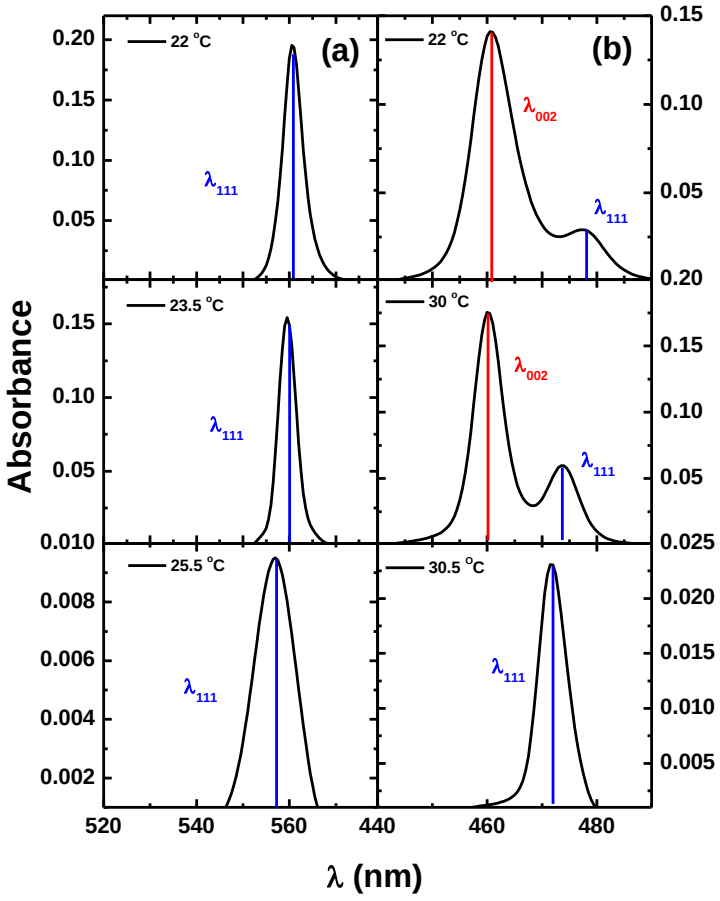


**Figure 4.11** Absorbance spectra of sample (a) LS and (b) HS recorded at different temperature while cooling at the rate of 0.5 °C per hour. Vertical lines indicate Bragg peak positions.

In the case of PNIPAM microgel spheres, dangling polymer chains (hairs) in the shell region and their entanglement with hairs of neighbouring spheres, mimic the role of added interacting polymers to hard sphere colloidal crystals. Hence we believe

that entanglement of hairs is responsible for stabilizing FCC-HCP coexistence in osmotically compressed PNIPAM microgel crystals. Thus, observation of stable FCC-HCP coexistence in microgel crystals with $\phi > 0.74$ is understandable. Though the analogy presented here is qualitative, we believe that present studies pave the way for future experiments and numerical studies for understanding the phase behaviour of dense PNIPAM microgel spheres with tailored core and hairs.

### 4.3.6 Influence of rate of cooling on the fractions of FCC and HCP phases

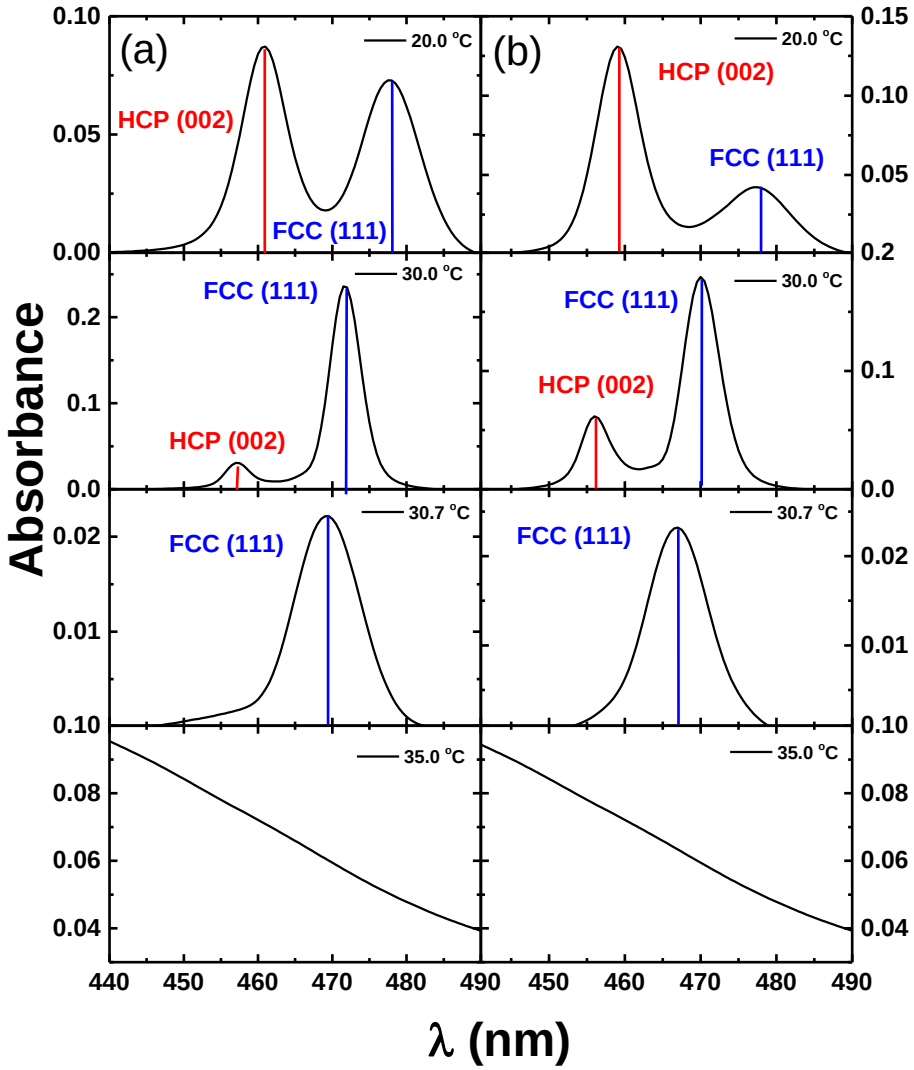


**Figure 4.12** Absorbance spectra of sample HS recorded at different temperature while cooling at the rate of (a) 0.1 °C per hour (b) 0.3 °C per hour. Vertical lines indicate Bragg peak positions.

In order to determine the role of cooling rate on the fraction of FCC and HCP phases in FCC-HCP coexisting state, sample HS was cooled at different cooling rates. The Bragg diffraction spectra of sample HS, annealed and cooled at 0.1 °C/hour and 0.3 °C /hour are recorded continuously from 35 °C to 20 °C and spectra recorded at 35 °C, 30.7 °C, 30 °C and 20 °C, for each rate, are shown in the Fig. 4.12(a) and 4.12(b). At 35 °C, no peak is observed in the absorption spectra for both samples, indicating the absence of structural ordering in the samples. A low intensity peak around 470 nm in the spectra recorded at 30.7 °C is observed for both rates. It indicates the structural ordering in the sample and the sample is found to be FCC. At 30.0 °C, a low intensity peak at 456 nm is observed along with a prominent peak around 470 nm. The peak around 455 nm corresponds to the reflection from the (002) plane of HCP structure and the peak around 470 nm is the reflection from the (111) plane of FCC structure. The peak corresponding to HCP structure becomes more prominent than FCC structure. Notice that, the peak corresponding to FCC structure is more prominent in the sample cooled at 0.1 °C per hour than in the sample cooled at 0.3 °C whereas the HCP peak is more prominent in the sample cooled at 0.3 °C per hour than in the sample cooled at 0.1 °C per hour.

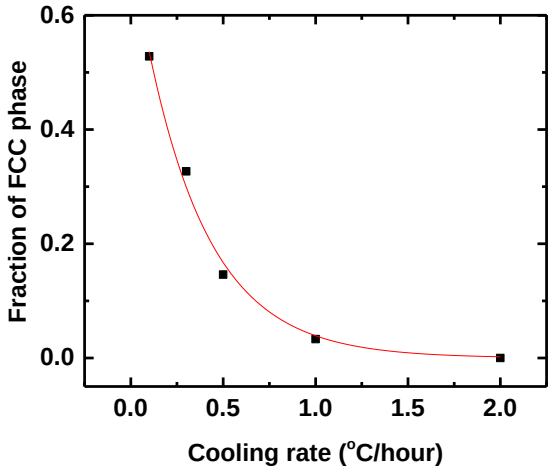


**Figure 4.13** Fraction of FCC component as a function of cooling rate in sample, HS. Continuous lines are guide to the eye.

Though the sample initially crystallized in FCC, HCP emerges as the temperature is further reduced. The fraction of FCC and HCP components in the suspension is found to depend on the cooling rate (Fig. 4.13). Note that the fraction of FCC in the suspension decreases exponentially with the cooling rate. Thus, it shows that changes in cooling rates alter only the relative fractions of FCC and HCP phases in the coexistence state in sample, HS.

### 4.4 Conclusion

PNIPAM microgel spheres are known to have a dense core and thin shell of dangling polymer chains. These chains are expected to overlap/entangle upon close packing to volume fraction $\geq 0.74$. With an aim to investigate the influence of these dangling polymer chains on the structure of PNIPAM microgel crystals, we prepared four samples with two different size microgel particles. Out of the four samples, two samples have been prepared with volume fraction less than 0.74 and other two with volume fraction, $\phi > 0.74$. In sample with volume fraction < 0.74, PNIPAM particles are observed to be in swollen state (*i.e.*, having same diameter as that measured under dilute condition). Particles showed reduction in size in the case of samples with $\phi > 0.74$. Sample with $\phi < 0.74$, FCC-HCP coexistence is observed under as prepared conditions which transforms to stable FCC state upon annealing. This behaviour is consistent with results reported on PNIPAM microgel crystals [70] and also analogous to that of hard sphere colloidal crystals [37].

Unlike samples of $\phi < 0.74$, sample of $\phi > 0.74$ showed glass-like order under as prepared condition which transformed to FCC-HCP co-existence upon annealing. Even upon annealing with very slow cooling rate (0.1 °C/hour), recrystallized sample showed FCC-HCP coexistence suggesting FCC-HCP

coexistence is the stable equilibrium state of osmotically compressed PNIPAM microgel crystals. Sub-diffusive behaviour at short times in osmotically compressed PNIPAM crystals suggests the presence of entanglement of dangling polymer chains between the shells of neighbouring PNIPAM microgel spheres. We believe that the entanglement of hairs stabilize HCP over competing FCC structure. Sample HS when cooled from liquid state to different temperatures below its melting temperature ($T_m$) showed that the sample crystallized with FCC structure grow just below $T_m$. Upon cooling to lower temperatures, crystallites with HCP structure are found to be predominant than FCC. From the above mentioned observation, we conclude that entanglement between dangling polymer chains (hairs) is responsible for stabilizing FCC-HCP coexistence as stable structure in osmotically compressed dense PNIPAM microgel crystals. We believe that present work paves way for future experiments and simulations on the dynamic stability of colloidal crystal structure of on stimuli responsive microgel particles and other soft spheres synthesized with tailored core and hairs.

# CHAPTER 5

# STRUCTURE AND DYNAMICS OF DENSE PNIPAM-CO-AAC MICROGEL CRYSTALS

This chapter deals with the determination of crystal structure of dense PNIPAM-co-Aac microgel crystals as a function of pH at a constant number density, using SLS. Dynamics of microgel particles in the dense suspension is studied using 3D DLS and its implication on the structure of these microgel crystals is discussed.

## 5.1 Introduction

In the previous chapter, it is shown that dense suspensions of neutral PNIPAM microgel suspension crystallize into FCC-HCP coexistence structure for volume fraction, $\phi > 0.74$ and FCC structure for $\phi > 0.5$ but less than 0.74 [70]. The crystal structure of pH responsive PNIPAM microgel suspensions with electrostatic interactions at high volume fractions have not been well-studied. Incorporation of co-monomer like acrylic acid into neutral PNIPAM microgels during synthesis makes them charged and hence are known as ionic microgels due to the presence of carboxylate ions [55]. In addition to its thermo responsive nature, PNIPAM-co-Aac microgels also exhibit pH response, due to the presence of acrylic acid moieties [48]. The dissociation constant, $pK_a$ of acrylic acid groups is 4.25. Hence, for pH < 4.25, carboxylic acid groups are in protonated state leaving the microgel particle in a neutral state with a slight negative charge due to the initiator added during polymerization. For pH > 4.25, carboxylic acid groups are in deprotonated state making microgel particles negatively charged due to the presence of carboxylate ion residues in the polymer chains. Diameter of the microgel particles vary as the pH of

the suspension is varied. Sudden increase in the particle size at pH ≈ 4.25, when the pH of the suspension is increased from 3.00 to 5.00, is identified as VPT. It is also known as neutral to charged transition [48]. At pH ≈ 4.25, most of the acrylic acid group dissociates into carboxylate ion and hydrogen ion. The electrostatic repulsion between the polymer chains, due to the presence of carboxylate ions, leads to sudden swelling of microgel particle. PNIPAM-co-Aac microgel suspensions are expected to show interesting phase behaviour as a function of pH [51], and the interparticle interaction of PNIPAM-co-Aac microgel particles changes from weekly attractive to repulsive when pH is varied from pH 3.00 to pH 5.00 [151].

Unlike neutral PNIPAM microgel particles, monodisperse PNIPAM-co-Aac microgel particles crystallize at low volume fraction, less than 0.5 and remain in disordered (glassy) state above the close-packed limit [51]. Ionic microgels deswell due to steric compression and ion-induced deswelling. In PNIPAM-co-Aac microgel suspensions, steric compression happens much below $\phi = 0.64$ whereas ion-induced deswelling becomes significant only for sample $\phi \geq 0.8$ which is well above the close-packed limit [77] and these particles swell in size to occupy the available free volume upon aging [51]. All these properties along with the core-shell nature of PNIPAM-co-Aac microgel particles make the study of phase behaviour of PNIPAM-co-Aac microgel suspensions interesting as a function of temperature, pH and salt concentration. Dense PNIPAM-co-Aac microgels at volume fraction, $\phi < 0.74$, have been reported to crystallize in random hexagonal close packed (RHCP) structure initially and transform into an FCC structure upon annealing [3,71] and such transformation is in accordance with theoretical calculations [5,72]. Theoretical calculations for very soft charged particles have predicted non-cubic structures at high concentrations. SANS [73] and SAXS [74] measurements on charged microgel

suspensions with $\phi > 0.8$ have shown that the suspension has crystallized with RHCP structure. In this chapter, we report the crystal structure and dynamics of dense PNIPAM-co-Aac microgel suspension as a function of pH using static and dynamic light scattering techniques. As prepared suspensions has crystallized into FCC-HCP coexistence structure. At low pH, microgel suspension after recrystallization exhibited transformation from FCC-HCP coexistence to FCC structure whereas samples at higher pH values remained in FCC-HCP coexisting structure. The dynamics of these particles is found to be diffusive at short times at low pH and sub-diffusive at higher pH values. The reason for the observed sub-diffusive behaviour and its implication on the structure of microgel crystals is discussed in this chapter.

## 5.2 Experimental methods

### 5.2.1 Sample preparation

PNIPAM-co-Aac microgel particles of size 1100 nm with size polydispersity 5.5 % synthesized through free radical precipitation polymerization method as described in section 2.1 have been used for the present investigation [3]. These suspensions are purified by dialyzing against Millipore water for two weeks to remove ionic impurities and unreacted species. Purified suspension is concentrated using stirred cell. The concentration, $n_p$ of the suspension is determined using the position of $q_{111}$ peak in the Bragg diffraction spectrum of the sample [88]. pH buffers ranging from pH 3.00 to 5.00 with constant ionic strength of 15 mM was prepared to avoid deswelling of microgel particles across pH due to variation in ionic strength [99]. The uncertainty in the pH measurement is about ± 0.03. Microgel crystals at each pH are prepared by adding 300 µl of buffer with 700 µl of the suspension. pH of each suspension was measured using pH meter. At each pH, required amount of

sample is loaded into the light scattering cells and used for the investigation of structure and dynamics.

### 5.2.2 Dynamic light scattering

Hydrodynamic diameter, *d* and size polydispersity of PNIPAM-co-Aac microgel particles as a function of pH is measured using DLS. All the measurement has been carried out at temperature 22 °C ± 0.1 °C. The variation of *d* as a function of pH is shown in Fig. 5.1.

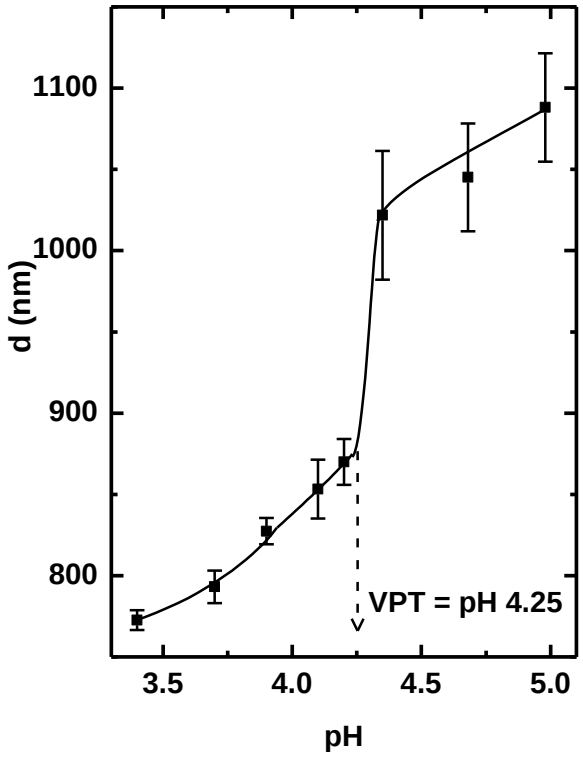


**Figure 5.1** Hydrodynamic diameter, *d* of PNIPAM-co-Aac microgel particles as a function of pH. Continuous line is guide to the eye.

Notice that the particle size increases with increase in pH of the suspension from pH 3.00 to 5.00. The sudden increase in particle size at pH = 4.25 is identified as VPT of microgels with respect to pH. At low pH, microgel particles are in protonated state and upon increasing the pH, acrylic acid moieties deprotonate gradually. At pH

≈ 4.25, most of the acrylic acid groups deprotonate resulting in sudden swelling of microgel particles due to electrostatic repulsion between the polymer chains.

### 5.2.3 Static light scattering

Dense microgel suspensions at different pH with constant number density, $n_p$ = 2.37 × $10^{12}$ particles/$cm^3$ are prepared. The structure of microgel crystals at each pH was determined by measuring scattered intensity, $I_s(q)$ as a function of scattering vector, $q$. With an aim to record Bragg reflection from different crystallites in the sample, the sample was rotated at a slow speed (0.6 rotations/minute) [103]. All the measurements are performed at 22 °C. The diffraction pattern thus recorded using SLS is analysed for possible crystal structures as described in section 2.5.1 [70]. Using the first peak position, all the other allowed Bragg peak positions for the structure is calculated. The structure of PNIPAM-co-Aac microgel crystals is identified to be FCC/HCP or FCC-HCP coexistence by matching the calculated peak positions with that measured experimentally.

**Table 5.1** Sample details and the crystal structure of PNIPAM-co-Aac microgel crystals before and after annealing.

| **pH** | **Diameter, $d$ (nm)** | **$\frac{d_{nn}}{d}$** | **Volume fraction, $\phi$** | **Structure at 22 °C (As prepared)** | **Structure of recrystallized sample at 22 °C** |
|---|---|---|---|---|---|
| 3.40 | 772.6 | 1.09 | 0.58 | FCC-HCP | FCC |
| 3.70 | 801.3 | 1.05 | 0.64 | FCC-HCP | FCC-HCP |
| 4.10 | 853.2 | 0.99 | 0.77 | FCC-HCP | FCC-HCP |
| 4.35 | 1021.7 | 0.82 | 1.32 | FCC-HCP | FCC-HCP |
| 4.7 | 1045.1 | 0.80 | 1.41 | FCC-HCP | FCC-HCP |
| 5.00 | 1088.2 | 0.78 | 1.60 | FCC-HCP | FCC-HCP |

Sample details and crystal structure under as prepared condition and recrystallized samples for different values of pH is given in Table 5.1. As prepared samples are recrystallized by increasing the temperature of the sample to 35 °C and maintained at that temperature for 1 hour and cooled back to room temperature (22 °C) at the rate of 0.1 °C/hour.

## 5.3 Results and discussion

### 5.3.1 Structure of PNIPAM-co-Aac microgel crystals

PNIPAM-co-Aac microgel suspensions prepared at pH 3.40, 3.70, 4.10, 4.35, 4.7, 5.00 are loaded into separate cylindrical glass cells of diameter 5 mm and left undisturbed for 24 hours. These samples are referred to "as prepared" samples. Undisturbed "as prepared" samples exhibited iridescence indicating the crystalline order in the samples. Bragg diffraction pattern of these samples is measured using SLS. Fig. 5.2(a) shows the Bragg diffraction pattern of the PNIPAM-co-Aac microgel crystals at pH 3.40. The sharp peaks in the Bragg diffraction pattern indicate the crystalline nature of the sample. Upon analysis, the experimentally recorded Bragg diffraction pattern is found to match well with that of FCC-HCP coexisting structure. FCC and HCP structures differ only in the stacking sequence. The Bragg peaks of (111), (220), (311) and (222) of FCC structure and (002), (110), (112), (004) of HCP structure occur at the same position as they are common to both the structures [145]. However (200) and (400) reflections are inherent to FCC structure differ with (100), (101) and (103) peaks which are inherent to HCP structure [144]. In crystals with stacking faults, the Bragg peaks which are common to both the structures overlap with each other [144].

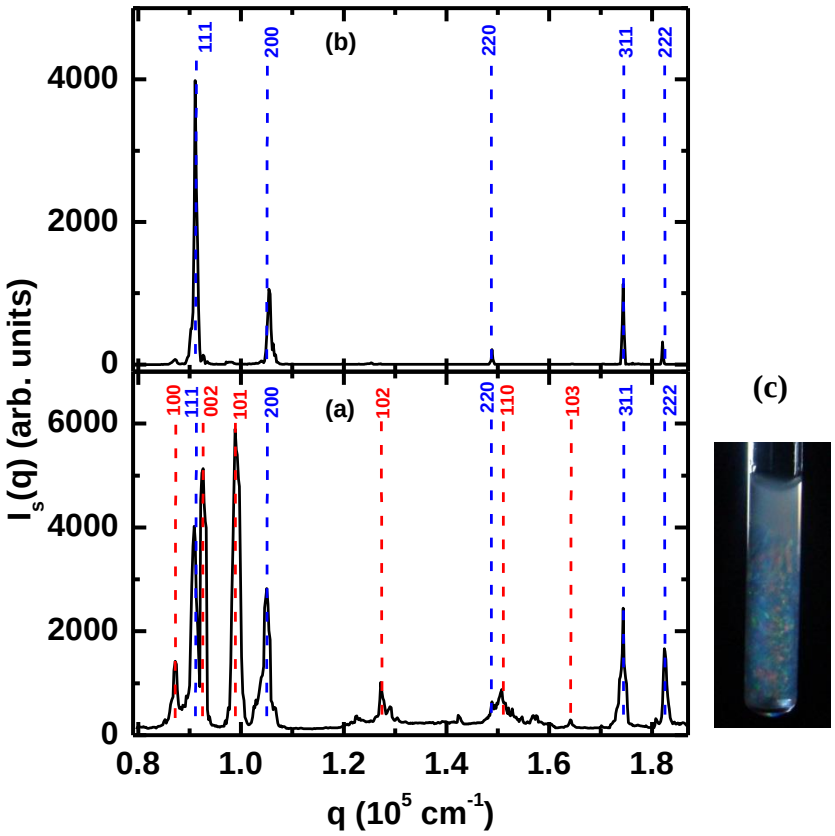


**Figure 5.2** Bragg diffraction pattern of PNIPAM-co-Aac microgel sample at pH 3.40 (a) as prepared (b) recrystallized (upon annealing with a cooling rate of 0.1 °C/hour) recorded using SLS at 22 °C. Vertical lines indicate the Bragg peak positions corresponding to ideal FCC and HCP structure (c) photograph showing iridescence in the as prepared sample of PNIPAM-co-Aac microgel crystals at pH 3.40.

Notice that in Fig. 5.2(a) peaks corresponding to both FCC and HCP structures are clearly resolved and indexed. Observation of multiple peaks which are inherent to both the structures confirm FCC-HCP coexistence in the sample at pH 3.40. Volume fraction, $\phi$ and nearest-neighbour distance, $d_{nn}$ of microgel crystals are determined (as described in section 2.5.1) to be 0.58 and 844.7 nm respectively and are given in Table 5.1. The ratio $\frac{d_{nn}}{d} > 1$ indicated that the particles haven't undergone any compression due to osmotic pressure exerted by the neighbouring particles at this volume fraction [78].

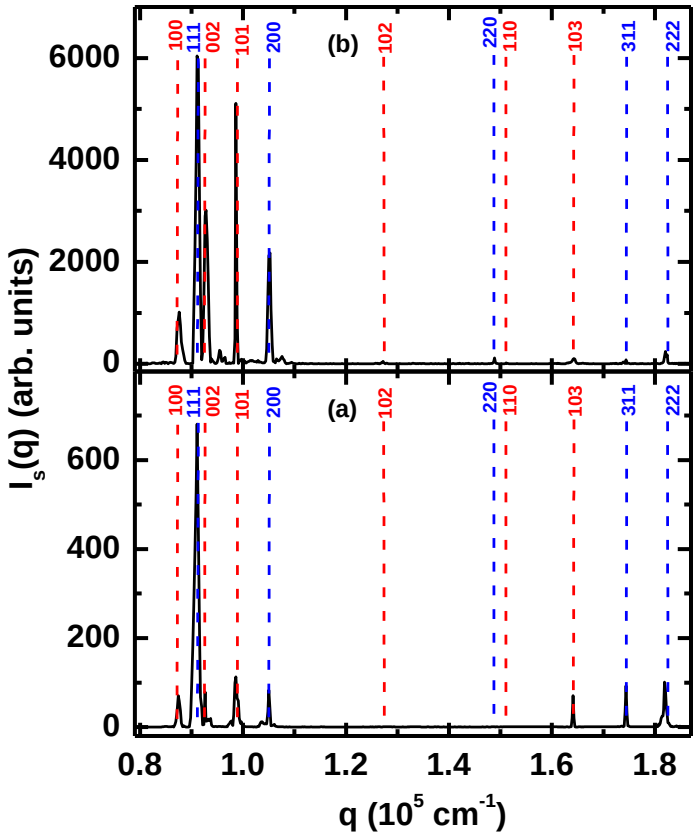


**Figure 5.3** Bragg diffraction pattern of PNIPAM-co-Aac microgel sample at pH 3.70 (a) as prepared (b) recrystallized (upon annealing with a cooling rate of 0.1 °C/hour) recorded using SLS at 22 °C. Vertical lines indicate the Bragg peak positions corresponding to ideal FCC and HCP structure.

At pH 3.40, PNIPAM-co-Aac microgel particles are almost neutral and hence, the equilibrium crystal structure is expected to be FCC analogous to that of Hard-sphere crystals [65]. In order to know whether FCC-HCP coexistence structure is stable or FCC structure is stable, the sample is subjected to recrystallization by increasing the temperature of the sample to 35 °C. The heated sample was maintained at that temperature for one hour and then cooled to room temperature (22 °C) with a cooling rate of 0.1 °C /hour. The recrystallized sample showed iridescence. Bragg diffraction pattern of the recrystallized sample recorded using SLS was shown in Fig. 5.2(b). Notice that peaks corresponding to HCP structure i.e., (100), (002), (102), (110), etc., were completely absent and peaks corresponding to FCC structure only

were present in the Bragg diffraction pattern (Fig. 5.2(b)). This suggests that PNIPAM-co-Aac microgel crystals at pH 3.40 with volume fraction, $\phi = 0.58$ has transform to its equilibrium FCC structure. These observations are consistent with recent report on PNIPAM-co-Aac microgel crystals studied using SAXS [71] and PNIPAM-co-Aac microgel particles behave like neutral PNIPAM microgels [65].

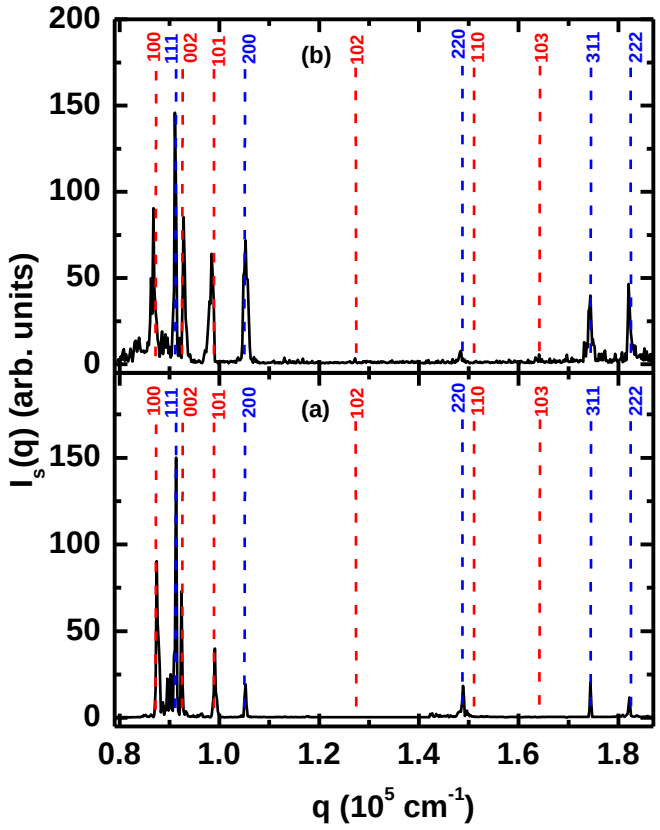


**Figure 5.4** Bragg diffraction pattern of PNIPAM-co-Aac microgel sample at pH 4.10 (a) as prepared (b) recrystallized (upon annealing with a cooling rate of 0.1 °C/hour) recorded using SLS at 22 °C. Vertical lines indicate the Bragg peak positions corresponding to ideal FCC and HCP structure.

Bragg diffraction spectrum of PNIPAM-co-Aac microgel crystals at pH 3.70 in "as prepared" condition is shown in Fig. 5.3(a). Analysis of Bragg diffraction pattern shows that the crystal structure of the sample is FCC-HCP coexistence. The sample is recrystallized as mentioned earlier. Bragg diffraction spectrum of the

recrystallized sample shows FCC-HCP coexisting structure (Fig. 5.3(b)) identical to that observed in the "as prepared sample". The position of peaks observed in the Bragg diffraction spectrum was found to agree well with that of calculated one. Volume fraction, $\phi$ of the suspension is calculated using first peak position and found to be 0.64 which is less than that of cubic close packed limit ($\phi = 0.74$).

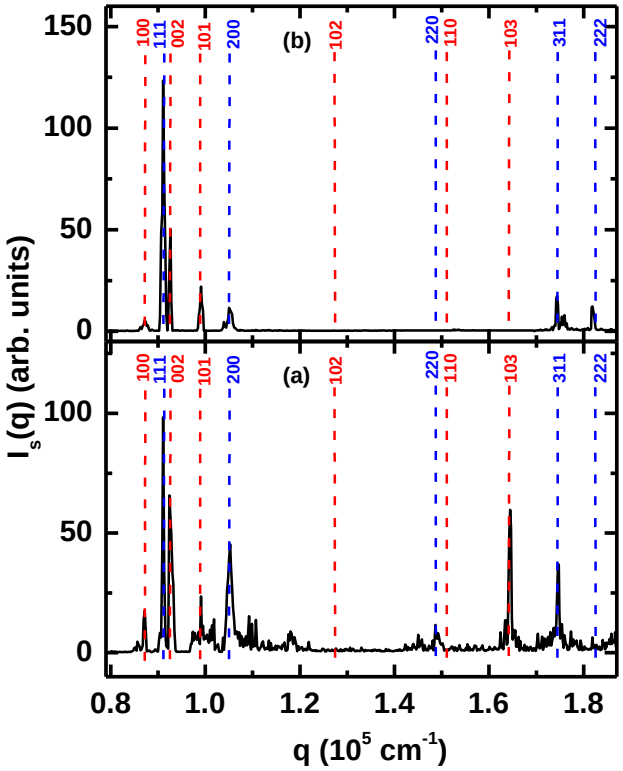


**Figure 5.5** Bragg diffraction pattern of PNIPAM-co-Aac microgel sample at pH 4.35 (a) as prepared (b) recrystallized sample. Vertical lines indicate the Bragg peak positions corresponding to ideal FCC and HCP structure.

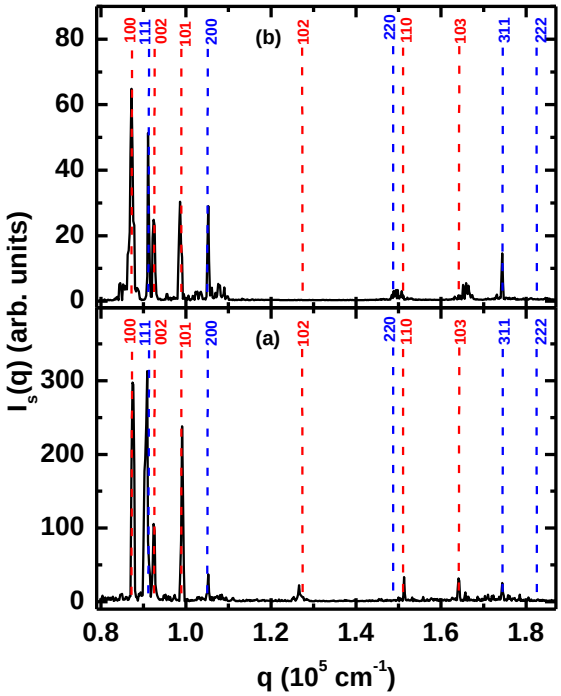


**Figure 5.6** Bragg diffraction pattern of PNIPAM-co-Aac microgel sample at pH 4.70 (a) as prepared (b) recrystallized sample. Vertical lines indicate the Bragg peak positions corresponding to ideal FCC and HCP structure.

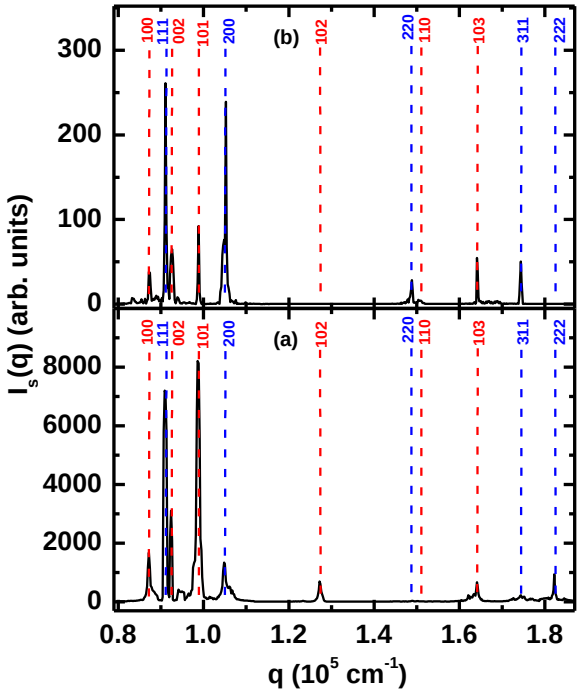


**Figure 5.7** Bragg diffraction pattern of PNIPAM-co-Aac microgel sample at pH 5.00 (a) as prepared (b) recrystallized sample. Vertical lines indicate the Bragg peak positions corresponding to ideal FCC and HCP structure.

Bragg diffraction pattern of PNIPAM-co-Aac microgel crystals prepared at pH 4.10, 4.35, 4.70, 5.00 under "as prepared" conditions are shown in Fig. 5.4(a), 5.5(a), 5.6(a), 5.7(a) respectively. These samples exhibited FCC-HCP coexistence. Volume fraction, $\phi$ and nearest-neighbour distance, $d_{nn}$ of microgel crystals at each pH are determined and listed in Table 5.1. Notice that $d_{nn} < d$ and the corresponding volume fraction of microgel crystals at pH 4.1, 4.35, 4.70 and 5.00 are greater than 0.74. The observation that $d_{nn} < d$ ($\frac{d_{nn}}{d} < 1$) suggests that microgel particles in dense suspensions ($\phi > 0.74$) gets compressed due to osmotic pressure exerted by the surrounding particles [78,142]. The number density, $n_p$ in all the samples discussed in the chapter was kept constant. The volume fraction, $\phi > 0.74$ which is unphysical is due to the swollen diameter, *d* measured under dilute conditions using DLS is used for its calculation.

With an objective to identify the equilibrium crystal structure, the samples were recrystallized by increasing and maintaining the temperature of the sample at 35 °C for 1 hour and cooling at 0.1 °C/hour to room temperature (22 °C). Bragg diffraction pattern of these recrystallized samples were shown in Fig. 5.4(b), 5.5(b), 5.6(b), 5.7(b) respectively. After analyzing the Bragg diffraction pattern, the structure of these recrystallized sample were found to be FCC-HCP coexistence structure. At concentration, $\phi > 0.74$ these change in interactions in microgel particles have negligible effect on the phase behaviour of microgel crystals and the crystal structure remained to be FCC-HCP coexistence.

### 5.3.2 Melting of PNIPAM-co-Aac microgel crystals

In order to study the effect of temperature on PNIPAM-co-Aac microgel crystals and to identify the melting point of these crystals, the samples are subjected

to heating. Upon increasing the temperature, iridescence in the sample is found to disappear beyond a certain temperature and suspensions also turned turbid. Melting temperature of these crystals is identified by monitoring the Bragg peak intensity, $I_{max}$ as a function of temperature [54]. Variation in $I_{max}$ measured at Bragg peak position at $q = 0.91 \times 10^5$ cm$^{-1}$ as a function of temperature, $T$ for sample with pH 3.40 and 5.00 were shown in Fig. 5.8 and 5.9 respectively. Bragg peak Intensity, $I_{max}$ decreased monotonically with temperature, $T$. For sample with pH 3.40 (Fig. 5.8), a sudden decrease at $T$ = 24 °C in Bragg peak intensity is observed and it is identified as the melting temperature, $T_m$. The sudden jump in the intensity, $I_{max}$ is due to the structural transition from crytalline state to liquid state. Beyond $T_m$ the intensity $I_{max}$ decreases continuously where the microgel suspension is identified to be in liquid state by observing broad peak in its scattering profile.

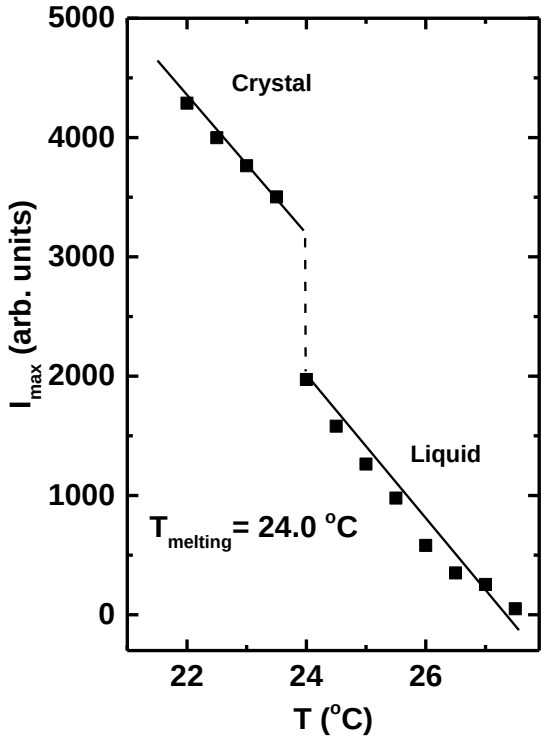


**Figure 5.8** Bragg peak intensity, $I_{max}$ as a function of $T$, for PNIPAM-co-Aac microgel crystals at pH 3.40. Continuous lines are guide to the eye. Dotted line indicates the melting temperature of microgel crystals.

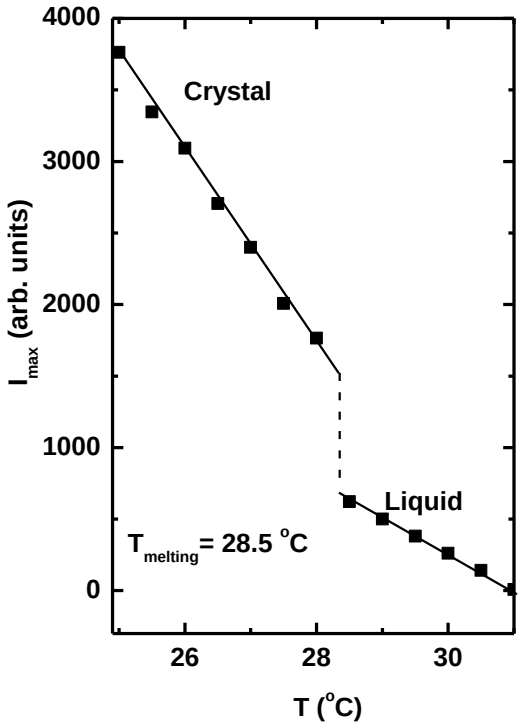


**Figure 5.9** Bragg peak intensity, $I_{max}$ as a function of $T$, for PNIPAM-co-Aac microgel crystals at pH 5.00. Continuous lines are guide to the eye. Dotted line indicates the melting temperature of microgel crystals.

Similarly, melting temperature of PNIPAM-co-Aac microgel crystals at pH 5.00 was identified to be 28.5 °C. Variation of $I_{max}$ ($q$ =0.91 X $10^5$ $cm^{-1}$) as a function of tempearture, $T$ for microgel crystals at pH 5.00 is shown in Fig. 5.9. At pH 5.00, microgel particles are in completely deprotonated state and negatively charged due to the presence of carboxylate ions in the polymer chains. Higher melting temperature, $T_m$ of microgel crystals at pH 5.00 than that of pH 3.40 is due to the repulsive interaction between these microgel particles at pH 5.00. Melting temperature of microgel suspension increased as the pH of the suspension was increased from 3.00 to 5.00.

### 5.3.3 Dynamics in dense PNIPAM-co-Aac microgel crystals

In order to understand the reason for observing FCC-HCP coexistence in dense PNIPAM-co-Aac microgel crystals, detailed 3D-DLS studies is carried out on these samples at room temperature (22 ºC). These particles upon concentration are known to undergo osmotic compression. Joshi *et. al.*,[88] have shown that dynamics in osmotically compressed PNIPAM microgel crystals ($\phi > 0.74$) is sub-diffusive at short times and arises due to entanglement of dangling polymer chains between the shells of neighbouring microgel spheres. The entanglement is absent microgel crytals with volume fraction, $\phi < 0.74$. In order to verify the presence of entanglement in the samples, we carried out DLS studies on all the samples. After equilibrating the sample at 22 °C, intensity auto-correlation function $g^{(2)}(q,t)$ was measured for 30 minutes at each pH and measurements have been repeated for five times. The field correlation, $f(q,t)$ obtained from $g^{(2)}(q,t)$ is used to determine mean square displacement (MSD) using Eq. (2.14). MSD was used to infer the kind of dynamics that these particles exhibit in the sample at short times. Short time regime in MSD data was identified using cage rearrangement time, $\tau_R$ as reference and given by

$$\tau_R = \frac{d^2}{4D_0} \tag{5.1}$$

where *d* is the size of the microgel particle and $D_0$ is the free diffusion co-efficient. For PNIPAM-co-Aac microgel samples used in the investigation of dynamics, $\tau_R$ is of the order of milli seconds. Fig. 5.10 shows MSD in units of average inter-particle separation of PNIPAM-co-Aac microgel particles in dense suspension as a function of time. Notice in Fig. 5.9, for all samples MSD at short times increases with time. The MSD data was fitted from 10 μs to 1000 μs with the Eqn. 2.18 to extract time

exponent, $\alpha$ which was used to classify the dynamics of the particles in the suspension [86].

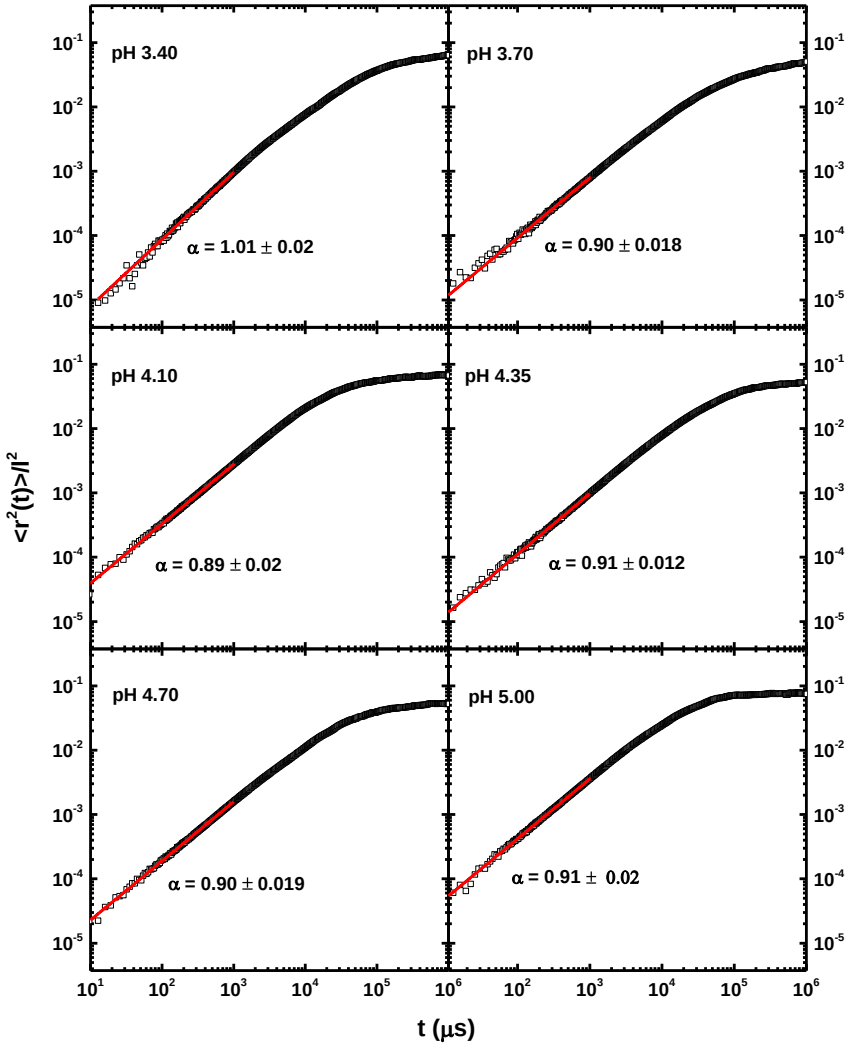


**Figure 5.10** Mean square displacement in units of average inter-particle separation, $l = n_p^{-1/3}$ versus time in PNIPAM-co-Aac microgel samples at pH 3.40, 3.70, 4.10, 4.35, 4.70 and 5.00. Lines represent the fit to Eqn. (2.14) at short times.

For sample prepared at pH 3.40, the time exponent, α is found to be 1 which suggests that the particle motion is diffusive at short times. For samples prepared at pH 3.70, 4.10, 4.35, 4.70, 5.00 the time exponent, α is found to be less than 1 suggests that the particle motion becomes sub-diffusive. PNIPAM microgel particles in dense suspensions with volume fraction greater than 0.74, were reported to exhibit sub-

diffusive motion at short times [88]. The sub-diffusive behaviour arises due to the overlap of dangling polymer chains between the shells of neighbouring particles in the surrounding as shown in Fig. 5.11.

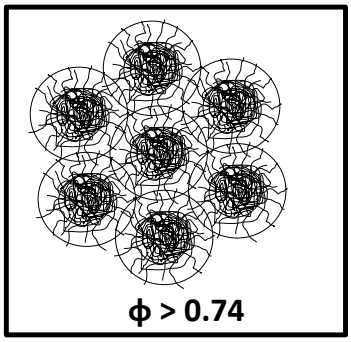


**Figure 5.11** Schematic picture depicting core-shell nature of PNIPAM spheres with entanglement of dangling chains between neighbouring spheres.

The volume fraction of the sample at pH 3.70 was 0.64 which is less than that of cubic close packed limit, $\alpha$ is found to be less than 1. At this volume fraction, the nearest-neighbour distance, $d_{nn}$ is greater than the diameter of microgel particles, $d$ hence the overlap of dangling polymer chains between the shells of neighbouring particles are not expected to happen. But these particles exhibit sub-diffusive motion at short times. Interestingly, PNIPAM-co-Aac microgel particles have been reported to swell in size with time to occupy available free volume [51] and experiences steric compression well below a volume fraction of 0.64 [77]. Hence, even at volume fraction less than 0.74, it is possible for entanglement between the dangling polymer chains in the shells of neighbouring particles, which is understood from the sub-diffusive dynamics of the microgel particles at short times. At pH 4.10, the volume fraction of the suspension is greater than 0.74 and the entanglement of dangling polymer chains of neighbouring particles leads to sub-diffusive behaviour of microgel particles. Though, microgel particles are in charged state with electrostatic repulsion between the polymer chains at pH 4.35, 4.70, 5.00, at volume fraction greater than 0.74, there exists entanglement between the dangling polymer chains in the shells of

neighbouring paricles which is evident from the observed sub-diffusive motion of the particles at short times. Thus, the entanglement between the neighbouring PNIPAM-co-Aac microgel spheres stabilizes FCC-HCP coexistence structure in samples similar to that observed in case of neutral PNIPAM microgel spheres in chapter 4.

## 5.4 Conclusion

Monodisperse PNIPAM-co-Aac microgel particles of size 1100 nm are synthesized using free radical polymerization. Structure of PNIPAM-co-Aac microgel crystals prepared at pH 3.40, 3.70, 4.10, 4.35, 4.70 and 5.00 in "as prepared" condition and after recrystallization was investigated using static light scattering technique. All the samples exhibited FCC-HCP coexistence in "as prepared" condition. These crystals are recrystallized by cooling all the samples at 0.1 °C/hour from 35 °C to 22 °C. Upon recrystallization, sample at pH 3.40 is found to crystallize in FCC structure consistent with the earlier reports [71]. Microgel crystals at pH 3.70, 4.10, 4.35, 4.70, 5.00 are found to exhibit FCC-HCP coexistence rather than RHCP structure [73,74] even after recrystallization. Clearly resolved peaks corresponding to both FCC and HCP structures argue well for FCC-HCP coexistence in the sample. The entanglement of dangling polymer chains between the shells of neighbouring spheres inferred through the sub-diffusive motion of particles at short times is responsible for stabilizing HCP structure in the sample and coexists along with FCC structure. The phase behaviour of ionic microgels in dense condition is found to be similar to that of neutral microgels at volume fraction greater than cubic close packed limit.

# CHAPTER 6

# LIGHT SCATTERING STUDIES ON GEL IMMOBILIZED STIMULI RESPONSIVE MICROGEL CRYSTALS

This chapter deals with the immobilization of PNIPAM-co-Aac microgel crystals in Poly-acrylamide (PAAm) hydrogels by photo polymerization. These microgel crystals are investigated for their structural ordering before and after immobilization using SLS. The effect of immobilization on the temperature response of microgel crystals is investigated and discussed here.

## 6.1 Introduction

Colloidal crystals have been used for several of its applications mentioned in chapter 1 such as filters [19], sensors [17], optical switches [24], templates for photonic band gap materials [7,152-154], Bragg diffraction devices [155], etc. Immobilized colloidal crystals have been used for controlled uptake and release of drugs [81,82], Bragg filters [83], tunable photonic crystals [26,84], non-linear optical switches [23,24], chemical sensors [85], etc. Colloidal crystals grown in aqueous medium are fragile and unstable against shear and hence are not widely used for the fabrication of devices [7,79]. This limitation has been overcome by immobilizing them in a polymer hydrogel matrix. Immobilization results in retaining periodic arrangement of colloidal crystals in a polymer hydrogel matrix, hence provides stability against shear, ionic impurity and temperature due to cross-linked network of polymer chains [79,95,96,156]. These immobilized colloidal crystals also serve as portable photonic crystals [7,157,158]. Hard spheres as well as charged colloidal crystals have been immobilized in normal and stimuli responsive hydrogels

[19,23,26,83,84,158,159]. Immobilized colloidal crystals are studied for their sensitivity and response to external stimuli [80]. Colloidal crystals of stimuli responsive microgel particles immobilized in polyacrylamide hydrogels (PAAm) have shown better sensitivity and response than immobilized hard sphere crystals. Though there have been reports of microgel crystals immobilized in hydrogels for their applications, there are no studies on the structure and dynamics of these crystals before and after immobilization. This chapter reports investigation on the structure and dynamics of microgel crystals before and after immobilization using light scattering technique. The thermal response of immobilized microgel crystal is investigated and the results are reported.

## 6.2 Experimental methods

### 6.2.1 Sample preparation

PNIPAM-co-Aac microgel suspensions of average size 1100 nm with size polydispersity 5.5 % was synthesized as described in section 2.1. These suspensions are purified as per the procedure described in section 2.2 and are concentrated to the desired volume fraction. The purified suspension is equilibrated for 24 hours in pH buffer 5.00 with ionic strength of 15 mM. The concentration of PNIPAM-co-Aac microgel suspension is determined to be $n_p = 3.38 \times 10^{12}$ particles/cm$^3$ using SLS as described in section 2.5.1. For immobilizing these microgel particles in PAAm hydrogels, 5M acrylamide (AAm) monomer solution at pH 5.00, 0.125 M Methelene-bis-acrylamide (BIS) cross-linker solution at pH 5.00 and photo initiator solution of 10% DEAP (v/v) in DMSO are prepared. For the present investigation, three samples *viz*., pure hydrogel (PAAm hydrogel without microgel particles), dilute PNIPAM-co-Aac microgel particles immobilized in PAAm hydrogels, dense PNIPAM-co-Aac

microgel crystals immobilized in PAAm hydrogels are prepared by photo-polymerization method as described in section 6.2.2. Details of chemicals used in preparing the samples are given in Table 6.1.

**Table 6.1** Details of chemicals and their quantities used for the preparation of 1 ml PAAm hydrogels with and without PNIPAM-co-Aac microgel particles.

| **Label** | **Acrylamide (5M) (µL)** | **BIS (0.125 M) (µL)** | **Photo initiator (µL)** | **Microgel particles (µL)** | **Buffer solution, pH 5.00 (µL)** |
|---|---|---|---|---|---|
| PAAm Hydrogel | 200 | 40 | 10 | - | 750 |
| Dilute sample | 200 | 40 | 10 | 5 | 745 |
| Dense sample | 200 | 40 | 10 | 700 | 50 |

### 6.2.2 Preparation of PAAm hydrogels

Poly-acrylamide (PAAm) hydrogel is prepared by polymerizing 3.5 wt% of acrylamide (AAM) solution and 2.1 wt% of BIS (BIS/ (AAM+BIS)) solution using photo initiator 2, 2-diethoxyacetophenone (DEAP). 10 µl of 10% DEAP in DMSO (dimethyl sulfoxide) is added to acrylamide and BIS solution as mentioned in Table 6.1. This pregel solution is loaded into a cylindrical glass cell of diameter 5mm which is used for light scattering measurement. Polymerization was initiated by irradiating the solution with UV light at room temperature (22 °C) and is continued for 2 hours to complete the polymerization which yielded poly acrylamide hydrogels (PAAm). Hydrogel, thus prepared, was allowed to equilibrate at room temperature for at least

24 hours before measurement. Hydrogel sample thus prepared is found to be without any air bubble and transparent.

### 6.2.3 Immobilization of PNIPAM-co-Aac microgel particles

1 ml of pregel solution is prepared by mixing acrylamide and BIS solution with photo initiator as mentioned in Table 6.1. 5 µl of concentrated PNIPAM-co-Aac microgel suspension is added to the pregel solution placed in 5mm diameter cylindrical glass cell, which corresponds to a number density, $n_p = 2.8 \times 10^7$ particles/cm$^3$. Pregel solution containing microgel particles is allowed to equilibrate for 24 hours before polymerization. PAAm hydrogel immobilized with PNIPAM-co-Aac microgel particles is prepared by photo polymerization of the mixture by irradiating with UV light. Hydrogel consisting of PNIPAM-co-Aac microgel particles with $n_p = 2.8 \times 10^7$ particles/cm$^3$ is labelled as "dilute sample". The sample is equilibrated for 24 hours at room temperature before making light scattering measurements.

### 6.2.4 Immobilization of PNIPAM-co-Aac microgel crystals in PAAm hydrogel

Pregel solution containing acrylamide, BIS and DEAP is added to 700 µl of dense PNIPAM-co-Aac microgel suspension (Table 6.1) which corresponds to a number density of $n_p = 2.37 \times 10^{12}$ particles/cm$^3$. This mixture is taken in a 5mm diameter cylindrical glass cell, and equilibrated for 24 hours at room temperature. Microgel suspension in the pregel solution exhibited crystallization and showed iridescence upon white light illumination. In order to homogenize the sample, it is heated to 35 °C, maintained at that temperature for 1 hour and then cooled back to room temperature (22 °C) at the rate of 0.1 °C/hour. Upon cooling, the sample once

again crystallized by exhibiting bright iridescence which is shown in Fig. 6.1(c). Immobilization of PNIPAM-co-Aac microgel crystals in poly acrylamide hydrogel is carried out in a controlled manner to retain the structural ordering in the sample as polymerization of acrylamide is an exothermic reaction [160]. As PNIPAM-co-Aac microgel particles are thermoresponsive in nature, heat released during polymerization of acrylamide decreases the effective volume fraction of the sample leading to melting of microgel crystals. Nayak *et. al*., have reported that microgel crystals upon immobilization in PAAm hydrogels, gets disordered [161]. This is overcome by photo polymerizing the sample at temperature less than 15 °C which facilitated the removal of heat from the sample and retaining the crystalline order in the sample.

## 6.3 Results and discussion

### 6.3.1 Structure of PNIPAM-co-Aac microgel crystals before and after immobilization

Since the immobilized particle in PAAm hydrogel does not span the configuration space due to arrested diffusion, the immobilized suspension is a non-ergodic system. Hence, instead of time averaged scattered intensity, $I_s(q)$ ensemble averaged scattered intensity, $\langle I_s(q) \rangle$ is measured at a given $q$ by rotating the sample at a constant speed of 0.6 rotations / minute. The structure of PNIPAM-co-Aac microgel crystals is determined using SLS. The ensemble averaged scattered intensity, $\langle I_s(q) \rangle$ from the microgel crystals as a function of scattering wave vector, $q$ is recorded at room temperature, 22 °C. The sharp peaks in the Bragg diffraction pattern shown in Fig. 6.1 confirm the crystalline nature of the sample. The diffraction pattern is

analysed for possible (FCC/ HCP/RHCP) crystal structures [70] as described in section 2.5.1.

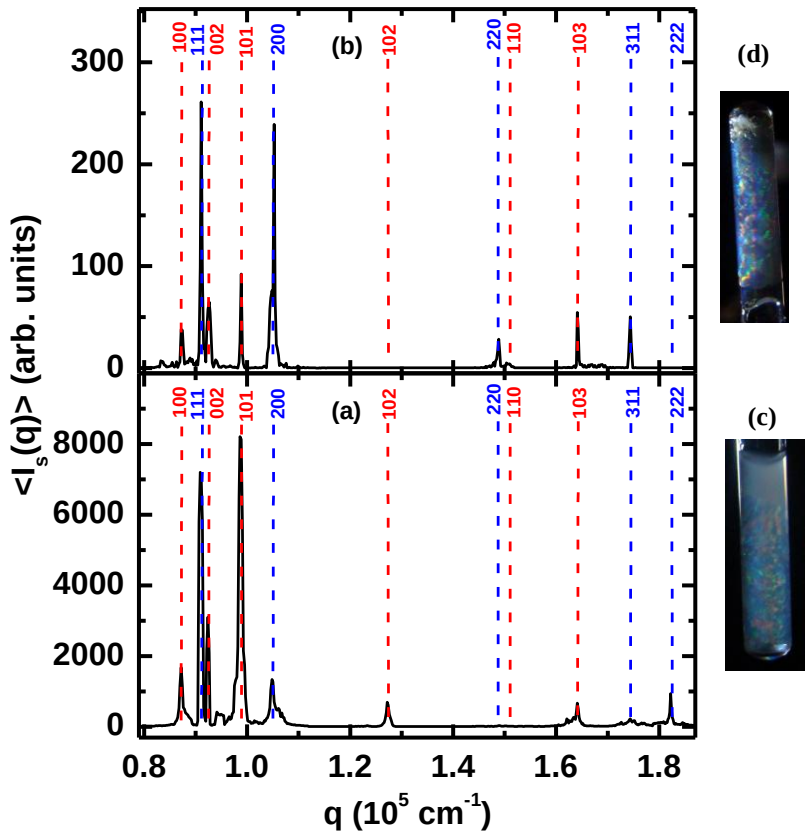


**Figure 6.1** Bragg diffraction pattern of PNIPAM-co-Aac microgel crystals at pH 5.00 (a) unimmobilized (b) immobilized recorded using SLS at 22 °C. Vertical lines indicate the Bragg peak positions corresponding to ideal FCC and HCP structure with $\phi = 1.6$ (c) photograph of unimmobilized PNIPAM-co-Aac microgel crystals with iridescence (d) photograph of gel immobilized PNIPAM-co-Aac microgel crystals with iridescence.

The Bragg diffraction pattern (Fig. 6.1) consists of peaks corresponding to both FCC and HCP structures. Calculated peak positions corresponding to FCC-HCP coexistence structure with $n_p$ = 2.37 × $10^{12}$ particles/cm$^3$, match well with that measured experimentally. The structure of PNIPAM-co-Aac microgel crystals in pregel solution at pH 5.00 is identified to be FCC-HCP coexistence (Fig. 6.1 (a)). Bragg diffraction pattern of PNIPAM-co-Aac microgel crystals immobilized in PAAm hydrogel is shown in Fig. 6.1(b). The sharp peaks in Fig. 6.1(b) suggest that

crystalline order is intact after the immobilization in PAAm hydrogel. The sample showed improved transparency after the immobilization and is due to matching of refractive index of microgel particles with that of PAAm hydrogel (Fig. 6.1 (c) & (d)). Further it can be seen that the structure remains unchanged (i.e., FCC-HCP co-existence structure) after immobilization (Fig. 6.1(b)). The structure of these microgel crystals before and after immobilization in PAAm hydrogels remained same. Each peak in the Bragg diffraction spectrum was identified and indexed.

### 6.3.2 Temperature response of microgel particles under immobilized conditions

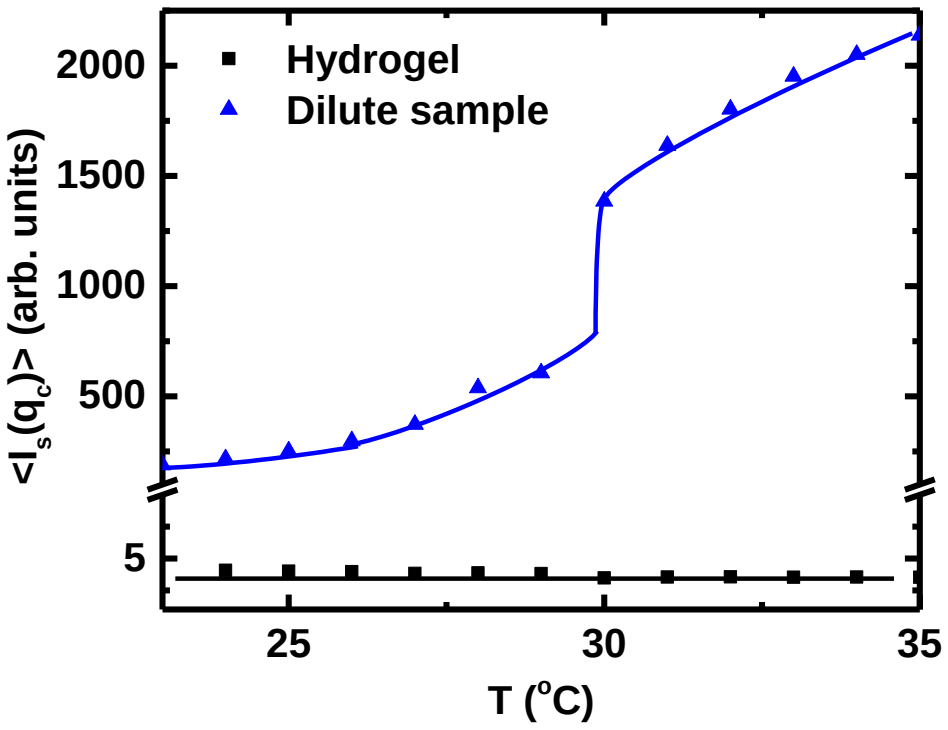


**Figure 6.2** Scattered intensity, $\langle I_s(q_c)\rangle$ at $q_c$ = 0.91 × $10^5$ $cm^{-1}$ as a function of temperature, $T$ for PAAm hydrogel, and dilute PNIPAM-co-Aac microgel particles ($n_p$ = 2.8 × $10^7$ particles/$cm^3$) immobilized in PAAm hydrogel. Laser power was kept constant during the measurement for all the samples. Lines are guide to the eye.

In order to understand the temperature response of PNIPAM-co-Aac microgel particles under immobilized condition, a dilute suspension of PNIPAM-co-Aac microgel particles with $n_p$ = 2.8 × $10^7$ particles/$cm^3$ is dispersed in the pregel solution

and immobilized in PAAm hydrogel. Temperature response of microgel particles immobilized in PAAm hydrogel is investigated using SLS and DLS by varying the temperature in the range of 22 ºC to 35 ºC. The ensemble averaged scattered intensity, $\langle I_s(q)\rangle$ at a scattering wave vector, $q_c$ = 0.91 × $10^5$ $cm^{-1}$ was monitored as a function of temperature and is shown in Fig. 6.2. The choice of scattering wave vector, $q_c$ = 0.91 × $10^5$ $cm^{-1}$ for monitoring the ensemble averaged scattering intensity, stems from our interest in the investigation of temperature response of PNIPAM-co-Aac microgel crystals, with (111) Bragg peak occurring at $q_c$ = 0.91 × $10^5$ $cm^{-1}$. The temperature response of microgel crystals have been investigated by monitoring the Bragg peak intensity at $q_c$ = 0.91 × $10^5$ $cm^{-1}$ which is the (111) peak of FCC structure as a function of temperature. Fig. 6.2 shows the variation of scattered intensity, $\langle I_s(q)\rangle$ as a function of temperature, *T* for PAAm hydrogel, dilute suspension of PNIPAM-co-Aac microgel particles immobilized in PAAm hydrogel. Since PAAm is a non-thermoresponsive polymer, one does not expect scattered intensity, $\langle I_s(q)\rangle$ to vary with *T* and Fig. 6.2 indeed shows $\langle I_s(q)\rangle$ being independent of T for PAAm hydrogel. Notice from Fig. 6.2 that the scattered intensity, $\langle I_s(q)\rangle$ as a function of temperature, *T* from microgel particles immobilized in PAAm hydrogel is higher than that from hydrogel without particles. This increase is mainly due to increase in the static inhomogeneities in the microgel particles immobilized sample [162]. The sudden jump in the scattered intensity observed at 30 °C is due to the VPT of the particle (Fig. 6.2). The scattered intensity being higher beyond 30 °C is explained as follows.

The scattered intensity, $\langle I_s(q)\rangle$ from a dilute suspension as a function of scattering wave vector is given by Eqn. 2.25 with $S(q) = 1$ and can be rewritten as

$$\langle I_s(q)\rangle = Ca^6\mu_e P(a) \tag{6.1}$$

where $C = \frac{16\,\pi^4 N}{\lambda^4}\frac{I_0}{L^2}$ a constant. Quantities that vary temperature are, $a^6$, $\mu_e = \left(\frac{\mu^2-1}{\mu^2+2}\right)^2$ and the particle form factor, $P(a)$. Since we are interested in the variation of particle form factor with respect to change in diameter at a fixed $q$ ($q = q_c$), the particle form factor, $P(a)$ for a sphere particle of radius, $a$ was given by,

$$P(a) = \left\{\frac{3[\sin(q_c a) - (q_c a)\cos(q_c a)]}{(q_c a)^3}\right\}^2 \tag{6.2}$$

We have calculated each of these factors seperately as a function of temperature to understand the variation of scattered intensity, $\langle I_s(q)\rangle$ with temperature, $T$ shown in Fig. 6.2.

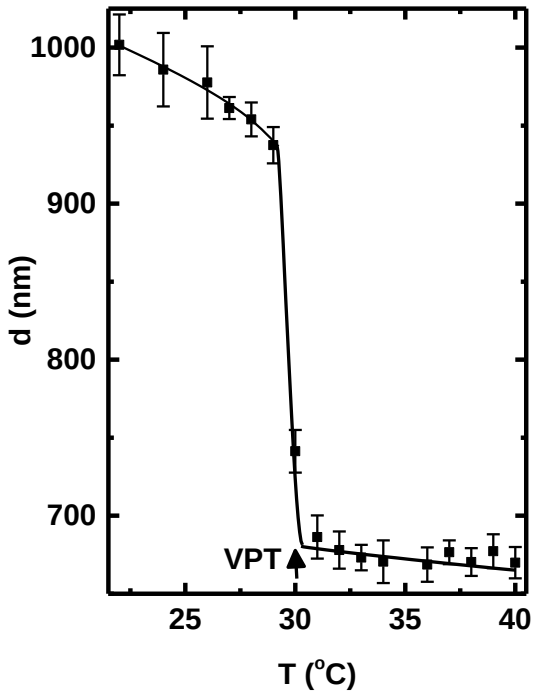


**Figure 6.3** Hydrodynamic diameter, *d* of PNIPAM-co-Aac microgel particles at pH 5.00 as a function of temperature, *T*. Continuous lines are guide to the eye.

For calculating the size dependence, $a^6$ and particle form factor $P(a)$ with respect to *T*, PNIPAM-co-Aac microgel particles size, *d* was measured at pH = 5.00 as a function of *T*

using DLS on a dilute suspension. The variation of $d$ with respect to $T$ is shown in Fig. 6.3. Sudden decrease in particle size at $T$ = 30 ºC due to VPT occuring at 30 ºC and is consistent with that reported in the literature [92]. Beyond VPT, the diameter remains almost constant (Fig. 6.3). Notice that VPT of microgel particle shifted to lower temperature at pH 5.00 as compared to that of PNIPAM microgel particles by ~ 4 ºC. The addition of acrylic acid during synthesis of PNIPAM-coAac not only makes the particle charged but also lowered the VPT. Using the measured diameter, $d$, $a^6$ is calculated in the temperature region 26 ºC to 34 ºC (around VPT) is shown in Fig. 6.4(a).

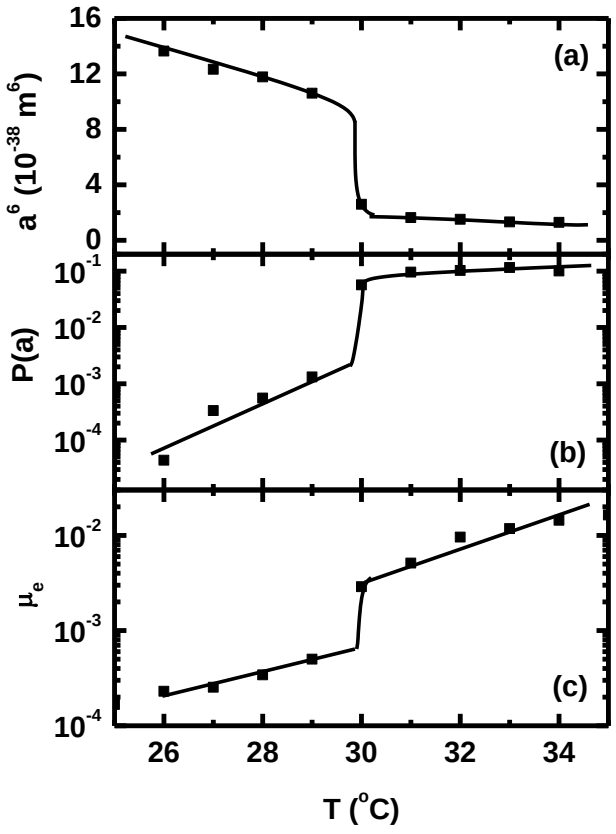


**Figure 6.4** Variation of $a^6$, $P(a)$ and $\mu_e$ as a function of temperature, $T$ calculated using diameter of the microgel particle, $d$ and refractive index of the particle, $\mu_p$ measured as a function of $T$. Continuous lines are guide to eye.

As expected with increase in $T$, $a^6$ also shows a sudden decrease at 30 ºC as a result of VPT. The variation in particle form factor, $P(a)$ due to the variation in $a$ at $q_c$ = 0.91 × $10^5$ $cm^{-1}$ is calculated as a function of $T$ using Eqn. 6.2 is shown in Fig.

6.4 (b). We assumed that PNIPAM-co-Aac microgel particles are homogeneous for calculating $P(a)$. Notice that $P(a)$ shows sudden increase at VPT (Fig. 6.4(b)) due to variation in particle size, *d*. Fig. 6.4(c) shows the variation of $\mu_e = \left(\frac{\mu^2-1}{\mu^2+2}\right)^2$ with respect to *T*. Here the refractive index of the particle, $\mu_p$ as a function of temperature, *T* was obtained by measuring the refractive index of the suspension, $\mu_s$ of known volume fraction, and refractive index of the buffer, $\mu_m$ as a function of temperature, *T* using Eqn. 3.2 given in chapter 3. The values of $\mu_s$ and $\mu_m$were measued using Abbe's refractometer as a function of *T*. Notice that (Fig. 6.4(c)) shows sudden increase due to sudden increase in the refractive index of the particle as a result of VPT. Though, with increase in *T*, $a^6$ decreases, sudden increase in $P(a)$ and $\mu_e$ at VPT compensates the decrease in $a^6$. Hence the observed sudden increase in the scattered intensity, $\langle I_s(q) \rangle$ at 30 ºC shown in Fig. 6.2 is essentially due to sudden decrease in the size of the particle and the confomitant increase in $P(a)$ and $\mu_e$. Thus, we conclude that immobilization of PNIPAM-co-Aac microgel particles in PAAm hydrogels does not alter significantly the VPT of pH responsive microgel particle.

### 6.3.3 Thermo response of dense stimuli responsive microgel crystals before and after immobilization

Having studied the temperature response of individual PNIPAM-co-Aac microgel particles immobilized in a PAAm hydrogel, it is of interest to know the collective behaviour of PNIPAM-co-Aac microgel particles in the ordered state under unimmobilized and immobilized conditions. Towards that we recorded Bragg peak intensity corresponding to (111) planes of FCC structure of PNIPAM-co-Aac microgel crystals as a function of temperature, *T* using SLS and is shown in Fig. 6.5(b). The Bragg peak intensity of the (111) peak is identified by recording the Bragg

peak as a function of $q$ which is shown in Fig. 6.5(a). Notice the Bragg peak corresponding to (111) peak of FCC structure in unimmobilized microgel crystals at T = 22 ºC, 29 ºC and 31 ºC. At T = 22 ºC, a sharp peak in the Bragg diffraction spectrum indicated the crystalline order in the sample. The intensity of the scattered light decreased with the increase in temperature. At T = 29 ºC, a broad peak was observed in the diffraction pattern which indicated the liquid like ordering in the sample. At T = 31 ºC, $\langle I_s(q) \rangle$ showed no peak as a function of $q$ indicates the structural ordering disappeared in the sample at T > 31 ºC.

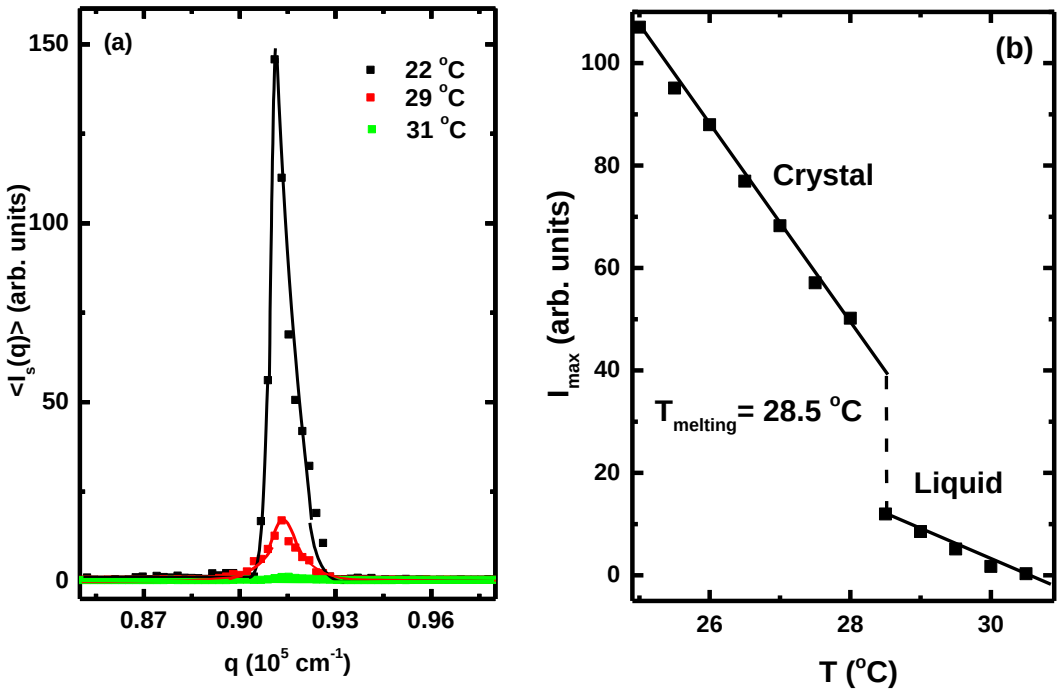


**Figure 6.5** (a) Bragg peak corresponding to (111) peak of FCC structure of unimmobilized PNIPAM-co-Aac microgel crystal as a function of temperature, *T*. (b) Variation of Bragg peak intensity, $I_{max}$ as a function of temperature. Lines are guide to the eye. Dotted line indicates the temperature at which microgel crystals undergo melting.

Fig. 6.5(b) shows the variation of Bragg peak intensity, $I_{max}$ as a fucntion of $T$. With increase in temperature, the Bragg peak intensity continuously decreases and show a sudden jump at T = 28.5 ºC. The sudden jump is identified as the melting temperature, $T_m$ of the crystal [54] as iridescence disappeared after 28.5 ºC. After

melting, no noticable change was observed in the peak position. As the temperature of the suspension was increased from 22 ºC to 32 ºC, microgel particles deswells as a response to temperature which resulted in the decrease of effective volume fraction of the suspension, leading to the melting of microgel crystals.

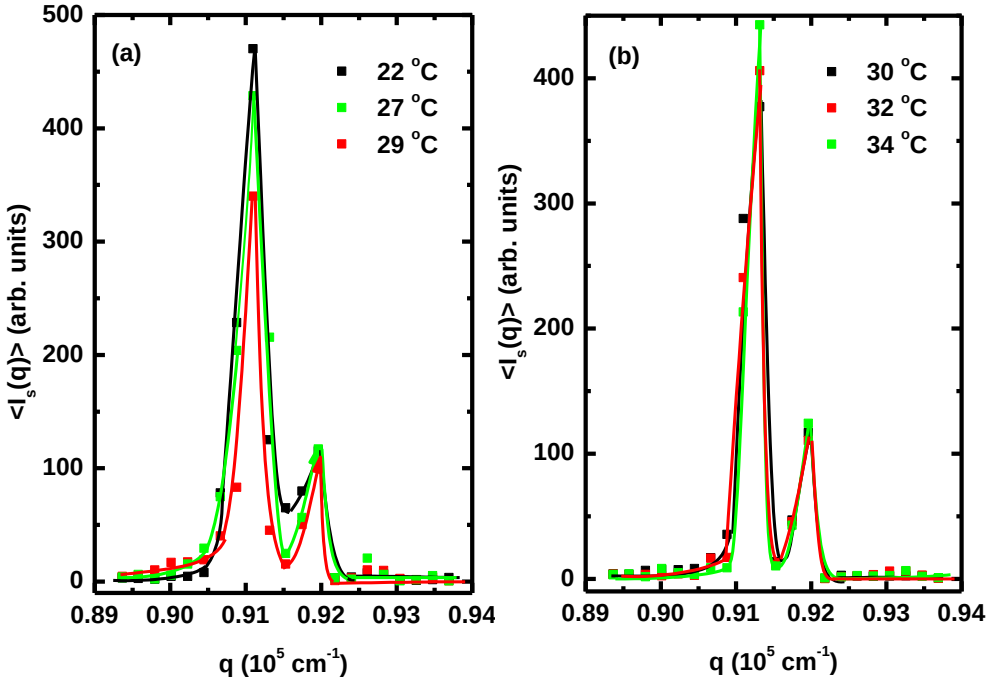


**Figure 6.6** Bragg peak corresponding to (111) peak of FCC structure of immobilized PNIPAM-co-Aac microgel crystal as a function of temperature, *T*. (a) before VPT of microgel particles, (b) after VPT of microgel particles. Continuous lines are guide to the eye.

PNIPAM-co-Aac microgel crystals are immobilized in PAAm hydrogels as described in section 6.2.4. The temperature response of immobilized microgel crystals is investigated using SLS. Bragg peak corresponding to (111) plane of FCC structure in immobilized PNIPAM-co-Aac microgel crystal is monitored as a function of temperature, *T*. For the sake of clarity, the Bragg diffraction spectra of immobilized microgel crystals having different behaviour are given separately (Fig. 6.6). A sharp peak around $q = 0.91 \times 10^5$ cm$^{-1}$ at $T = 22$ ºC was observed in the Bragg diffraction spectrum corresponding to (111) planes of FCC structure. A peak at $q = 0.92 \times 10^5$

$cm^{-1}$ corresponds to (002) planes of HCP structure. The scattered intensity, $\langle I_s(q) \rangle$ is recorded as a function of temperature, *T*. Bragg diffraction spectrum at T = 22, 27, 29 ºC for the immobilized microgel crystals is shown in Fig. 6.6(a) where the particles are in swollen state (before VPT) and the Bragg peak intensity is found to decrease with temperature. Fig. 6.6(b) shows the Bragg peak corresponding to (111) planes of FCC structure at T = 30, 32, 34 ºC where the particles are in deswollen state as elucidated from Fig. 6.3. Unlike unimmobilized microgel crystals which exhibited melting at $T_m$ = 28.5 ºC, immobilized microgel doesn't undergo melting. Crystalline order is preserved in the sample even at 34 ºC, indicated by the sharp peak in the Bragg diffraction spectrum (Fig. 6.8(b)).

Immobilization of microgel crystals in hydrogels has helped in retaining the structural ordering in the sample even beyond the VPT of microgel particles. The sample has showed iridescence even at 35 ºC. It can be mentioned that immobilization of microgel crystals has permanently locked the structural ordering in the sample. Even though the effective volume fraction of microgel crystals is decreased due to increase in the temperature, hydrogel matrix surrounding these crystals prevents them from melting and also acts as water reservoir for the microgel particles to swell back upon cooling. Intensity of the Bragg peak was plotted as a function of temperature (Fig. 6.7). As the temperature of the sample was increased, Bragg peak intensity, $I_{max}$ varied in a non-monotonous manner.

With the increase in temperature, the Bragg peak intensity decreases continuously up to 29 ºC. At 30 ºC, $I_{max}$ begins to increase with the temperature and increases up to 34 ºC. As the temperature is increased from 25 ºC to 29 ºC, the diameter of the particle decreases. Though the increase in refractive index of the

particle, $\mu_p$ with increase in *T*, $I_{max}$ decreases as the diameter of the particle decreases with *T* (Fig. 6.3), as the change in the $\mu_p$ is very small (Fig. 6.5). These particles are closely index matched with the surrounding hydrogel at T ≤ 29 ºC and its contribution to $\langle I_s(q) \rangle$ be very negligible. The scattered intensity $\langle I_s(q) \rangle$ decreases with temperature as it depends on the size of the particle as $a^6$ (Eqn. 6.1). At 30 ºC, increase in $I_{max}$ was due to sudden decrease in the diameter of the particle which concomitantly increases the refractive index of the particle, $\mu_p$ and particle form factor, $P(a)$ due to VPT of the microgel particles (Fig. 6.3). The scattered intensity increases with the increase in refractive index of the particle and particle form factor and decreases with decrease in the diameter of the particle. Large increase in the refractive index of the particle which is caused by the deswelling of the particle has resulted in the increase in the scattered intensity, $\langle I_s(q) \rangle$ from the immobilized microgel crystal between 30 ºC to 35 ºC.

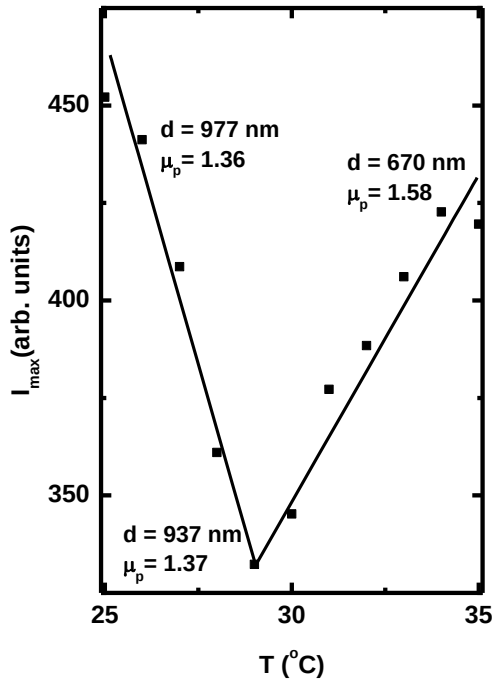


**Figure 6.7** Variation of Bragg peak intensity, $I_{max}$ corresponding to (111) plane of FCC structure as a function of temperature, *T*. Lines are guide to the eye.

## 6.4 Conclusions

Stimuli responsive PNIPAM-co-Aac microgel particles of size 1100 nm are synthesized and their temperature and pH response is studied. The temperature response of dilute PNIPAM-co-Aac microgel suspension in unimmobilized condition and in immobilized condition is studied using SLS. For the same laser intensity, the scattered intensity from the immobilized sample is found to be higher than that from the unimmobilized sample. It is due to the increase in the static inhomogeneity in the sample upon immobilization of microgel particles in the hydrogel medium. The sudden increase in the scattered intensity around 30 ºC was due to the increase in the refractive index of the particle and particle form factor caused by the sudden deswelling of microgel particle at VPT. The scattered intensity continued to increase up to VPT of the particle and almost remained constant with the temperature. Dense PNIPAM-co-Aac microgel sample at pH 5.00 is found to crystallize in the pregel solution. The structure of recrystallized PNIPAM-co-Aac microgel crystals was found to be FCC-HCP co-existing structure, using SLS. These microgel crystals are successfully immobilized in poly acrylamide hydrogel (PAAm) matrix by polymerizing the pregel solution with microgel crystals at low temperature (~15 ºC). Polymerization carried out at low temperature has prevented the microgel crystals from melting upon immobilization. The structure of immobilized microgel crystals remained the same as that of unimmobilized microgel crystals. Upon immobilization in PAAm hydrogel, the sample has become more transparent due to the index matching between the microgel particles and the hydrogel matrix. The temperature response of microgel crystals in unimmobilized case and immobilized case was studied by monitoring the Bragg peak intensity of (111) peak of FCC structure. Unimmobilized microgel crystal, upon increasing the temperature, exhibited crystal to

liquid transition consistent with the literature. Immobilization of microgel crystals in PAAm hydrogel has prevented melting of microgel crystals. The hydrogel matrix around these microgel crystals has prevented them from undergoing melting transition. Bragg peak was observed even beyond VPT of microgel particles from the immobilized microgel crystals, which indicate the structural ordering in the sample is preserved. The variation in the Bragg peak intensity with temperature was non-monotonous from the immobilized microgel crystals. Non-monotonous variation in the Bragg peak intensity was due to factors like diameter of the particle, particle form factor and the refractive index of the particle dominating at different range of temperature.

# CHAPTER 7

# SUMMARY AND FUTURE WORK

This chapter gives the summary and conclusion of the investigations made towards the thesis using PNIPAM microgel particles and their dense suspension.

## 7.1 Summary and conclusions

This chapter summarizes the investigations carried on stimuli responsive microgel suspensions under dilute and dense conditions and also under immobilized conditions in polymer hydrogels using experimental techniques *viz*., optical tweezers, static and dynamic light scattering techniques, 3D dynamic light scattering technique and UV-Visible spectroscopy. Stimuli responsive microgels are soft and core-shell structured particles with densely cross-linked core and a thin shell (20~30nm) of dangling polymer chains. Suspensions of stimuli responsive microgels exhibit liquid, crystalline and glassy phases similar to the other colloidal or atomic/molecular systems at appropriate conditions. A brief literature review on colloids and stimuli responsive microgels, structure and dynamics of microgel suspensions and their applications was presented in chapter 1. The motivation and objective for the present study on stimuli response microgel particles and their crystalline assemblies under unimmobilized and immobilized conditions were discussed in chapter 1.

Synthesis of PNIPAM and PNIPAM-co-Aac microgel particles by free radical precipitation polymerization was discussed in chapter 2. Theory of light scattering and optical tweezers and their instrumentation and calibration procedures were discussed in detail. Details of home built optical tweezers set-up were given in this chapter. Characterization of microgel particles for their size, size polydispersity, surface

charge density and VPT with respect to temperature and pH was given in detail in chapter 2. Analysis of light scattering and UV-Visible spectroscopy data to obtain structural ordering parameters of microgel crystals was also presented in chapter 2.

Dilute PNIPAM-co-Aac microgel suspensions at different pH in the range 3.00 to 5.00 were prepared for identifying the VPT of microgel particles as a function of pH. DLS technique is conventionally used to identify the VPT but it requires particle concentration of the order of $10^7$ particles/$cm^3$. In chapter 3, we have shown that VPT of a single PNIPAM-co-Aac particle can be identified unambiguously by using optical tweezers. Towards that we have designed and assembled optical tweezers set-up and characterized the trap parameters using established methods. Optical tweezers is shown to be an alternate technique to identify VPT of PNIPAM-co-Aac microgel particles. Trap stiffness was used as the parameter to identify the VPT as a function of pH. A sudden jump in the trap stiffness was observed as a function of pH. Occurrence of sudden change in trap stiffness was identified as the VPT by numerically computing trap stiffness and comparing it with that measured experimentally. The jump in the trap stiffness is understood to arise due to the sudden increase of microgel particle size with concomitant sharp decrease in the refractive index occurring at VPT at pH = 4.25.

After investigating the VPT of PNIPAM and PNIPAM-co-Aac microgel particles using DLS & optical tweezers, an attempt was made to understand the collective behaviour of these microgel particles by assembling them in crystalline order. Unlike hard spheres and charged colloid spheres, microgel particles are closely index matched with the solvent. This index matching helps in minimizing multiple scattering of light, hence facilitates the study of dense suspensions for their structural

ordering using light scattering. Towards understanding the equilibrium structure of PNIPAM microgel crystals under dense condition, PNIPAM microgel suspension of two different sizes (633 nm and 235 nm) with volume fractions above and below the cubic close packed limit, 0.74 were prepared by concentrating the samples using ultra-filtration technique. Dense microgel crystals were subjected to structural investigation using static light scattering (SLS) and UV-Vis spectroscopy techniques with volume fraction above and below 0.74. As prepared sample of dense PNIPAM microgel crystals exhibited FCC-HCP coexistence. Upon recrystallizing them, by rising the temperature above 35 ºC and cooling them to room temperature with a cooling rate of 0.1 ºC/hour, the sample with $\phi < 0.74$ was found to transform into an FCC structure. Whereas the sample with $\phi > 0.74$ was found to remain in FCC-HCP coexistence state even upon recrystallization. The study using different cooling rates resulted altering the relative fraction of FCC and HCP in the FCC-HCP coexistence state. The reason for FCC-HCP coexistence is understood by investigating the dynamics in the coexistence state. DLS studies have revealed sub-diffusive dynamics at short times due to the entanglement of dangling polymer chains in the shells of neighbouring particles. Thus entanglement is responsible for stabilizing the HCP phase over FCC resulting in observing FCC-HCP coexistence in dense microgel crystals with $\phi > 0.74$. The sub-diffusive behaviour of these microgel particles was found to become diffusive upon heating the crystal beyond their melting point.

In order to know whether electrostatic interactions between charged microgel particles under dense conditions, suspension of PNIPAM-co-Aac microgel particles were prepared and assembled them into crystalline order. The crystal structure of dense ionic microgel crystals were investigated for their stability at differ pH values ranging from 3.00 to 5.00. The disassociation constant of acrylic acid ($pK_a$) is 4.25.

Hence, the microgel particles exhibit neutral to charged transition upon increasing the pH of the suspension from 3.00 to 5.00 due to the presence of acrylic acid moieties on the polymer. The structure of PNIPAM-co-Aac microgel crystals was found to be FCC-HCP coexistence under as prepared conditions for values of pH ranging from 3.00 to 5.00. Upon recrystallization, the sample with pH 3.40 has transformed to FCC structure whereas recrystallized microgel crystals at pH 3.70, 4.10, 4.35, 4.70, and 5.00 were found to remain in FCC-HCP coexistence state. Samples which exhibited FCC-HCP coexistence showed sub-diffusive behaviour at short times similar to that of uncharged PNIPAM spheres in PNIPAM microgel crystals. The sub-diffusive behaviour of microgel particles at short times was due to the entanglement of dangling polymer chains in the shells of neighbouring particles. Thus PNIPAM-co-Aac microgel particles, though charged at high pH, under dense conditions behave like neutral PNIPAM microgel particles.

With an aim to understand the effect of immobilization on the VPT of individual PNIPAM microgel and on the stability of crystalline order, microgel crystals were immobilized in polymer hydrogel medium known as portable photonic crystals and also found several applications. PNIPAM microgel suspensions with different concentrations were immobilized in poly-acrylamide (PAAm) hydrogels by photo polymerization. In order to avoid melting of PNIPAM microgel crystals due to the heat liberated during polymerization, immobilization process was carried out at 15 ºC. The structure of these crystals before and after immobilization was investigated using SLS and found to be FCC-HCP coexistence. Microgel crystals under unimmobilized condition showed melting at T = 28.5 ºC whereas microgel crystals under immobilized condition showed iridescence 35 ºC i.e., even beyond VPT of these particles. We have showed that immobilization of microgel crystals in PAAm

hydrogel matrix has extended the stability of microgel crystals against melting. Bragg peak intensity of microgel crystals in hydrogel matrix was monitored as a function of temperature and found to vary non-monotonously. This behaviour is shown to arise from the decrease in the particle size and simultaneous increase in the refractive index of the microgel particle with temperature.

Key findings of this thesis are summarized below.

i. Indigenously designed and developed an optical tweezers set-up. Using which for the first time shown that VPT can be identified on a single microgel particle and shown that it gives a sharp transition as compared to that of conventional method of identifying VPT using DLS. VPT manifests as a sudden jump in the trap stiffness and is understood to arise from sudden decrease in the particle size with concomitant increase in the refractive index of the particle.

ii. For the first time FCC-HCP coexistence is shown to be the stable state for dense PNIPAM microgel crystals with volume fraction, $\phi > 0.74\phi > 0.74$ by performing detailed annealing studies. It is also shown that PNIPAM microgel crystals with volume fractions, $\phi < 0.74\phi < 0.74$ crystallize into FCC structure. Entanglement of dangling polymer chains between shells of neighboring microgel spheres is shown to occur in PNIPAM microgel crystals with$\phi > 0.74$, $\phi > 0.74$ and is evidenced by observing sub-diffusive behavior at short times. The entanglement is shown to disappear upon heating the crystals well about their melting temperature.

iii. Through detailed annealing studies, it was shown that overlap of dangling polymer chains between the shells of neighbouring spheres is responsible for

the stability of FCC-HCP coexistence observed in microgel crystals with $\phi > 0.74$.

iv. In dense pH responsive microgel crystals, as prepared samples in the pH range 3.00 to 5.00 crystallized in FCC-HCP coexisting structure. At pH = 3.40 ($\phi \approx 0.5$), the sample upon recrystallization was found to crystallize into FCC structure whereas the samples at other pH (3.7, 4.0, 4.35, 4.7, 5.0) with $\phi > 0.74$ has remained in the FCC-HCP state. Dynamics of PNIPAM-co-Aac microgel particles at short times in dense suspensions is found to be diffusive in sample with $\phi < 0.74$ and is sub-diffusive in sample with $\phi > 0.74$. The phase behaviour of ionic microgel crystals with $\phi > 0.74$ was found to be similar to that of dense microgel crystals of uncharged PNIPAM spheres. Our results suggested that Coulombic interaction between PNIPAM-co-Aac microgel particles is not dominant under dense conditions and does not play a major role in stabilizing the crystal structure.

v. Stimuli responsive PNIPAM-co-Aac microgel crystals were successfully immobilized in poly-acrylamide hydrogel (PAAm) matrix. The structure of stimuli responsive microgel crystal is shown to remain unaltered before and after the immobilization. Immobilization of microgel crystals is shown to extend the stability of microgel crystals against melting beyond VPT. Bragg peak intensity as a function of temperature from immobilized microgel crystals was found to vary non-monotonically. That non-monotonic behaviour is shown to arise from the simultaneous decrease of particle diameter with concomitant increase in the refractive index of the microgel particle with increasing temperature.

## 7.2 Scope for the future work

1. Employing optical tweezers to investigate first order/discontinuous process in stimuli responsive microgels with high polydispersity.
2. Identification of VPT of microgel particles by systematically varying the cross-linker, initiator and co-monomer concentration to improve existing theories that describe VPT in stimuli responsive microgels and swelling/deswelling behavior of macrogels.
3. Investigation of phase behaviour of microgel particles with varying cross-linker concentration with volume fraction, $\phi > 0.74$ to assert the role of softness of the particle in determining the crystal structure at higher densities.
4. Phase behaviour of ionic microgels with different surface charge density on microgel particles to validate the theoretical model which predicted non-cubic structures for charged microgels at higher densities.
5. Immobilization of neutral PNIPAM microgel of various sizes and investigating the response of these crystals to external stimuli.

## References


[1] P. N. Pusey and W. van Megen, Nature **320**, 340 (1986).

[2] B. V. R. Tata and S. S. Jena, Solid State Communications **139**, 562 (2006).

[3] P. S. Mohanty and W. Richtering, The Journal of Physicsl chemistry B **112**, 14692 (2008).

[4] E. B. Sirota, H. D. Ou-Yang, S. K. Sinha, P. M. Chaikin, J. D. Axe, and Y. Fujii, Physical Review Letters **62**, 1524 (1989).

[5] D. Gottwald, C. N. Likos, G. Kahl, and H. Löwen, Physical Review Letters **92**, 068301 (2004).

[6] N. A. Clark, A. J. Hurd, and B. J. Ackerson, Nature **281**, 57 (1979).

[7] B. V. R. Tata, R. G. Joshi, D. K. Gupta, J. Brijitta, and B. Raj, Current Science **103**, 10 (2012).

[8] B. V. R. Tata, in *Statistical physics of complex fluids*, edited by Shigenao Maruyama, and Michio Tokuyama (Tohoku University, Sendai, Japan, 2007).

[9] R. S. Crandall and R. Williams, Science **198**, 293 (1977).

[10] K.-Q. Zhang and X. Y. Liu, Nature **429**, 739 (2004).

[11] A. Scotti, U. Gasser, E. S. Herman, M. Pelaez-Fernandez, J. Han, A. Menzel, L. A. Lyon, and A. Fernández-Nieves, Proceedings of the National Academy of Sciences **113**, 5576 (2016).

[12] A. Cacciuto, S. Auer, and D. Frenkel, Nature **428**, 404 (2004).

[13] J. K. G. Dhont, C. Smits, and H. N. W. Lekkerkerker, Journal of Colloid and Interface Science **152**, 386 (1992).

[14] P. Schall, I. Cohen, D. A. Weitz, and F. Spaepen, Nature **440**, 319 (2006).

[15] W. van Megen and S. M. Underwood, Physical Review E **49**, 4206 (1994).

[16] E. R. Weeks, J. C. Crocker, A. C. Levitt, A. B. Schofield, and D. A. Weitz, Science **287**, 627 (2000).

[17] J. H. Holtz and S. A. Asher, Nature **389**, 829 (1997).

[18] Z. Cai, N. L. Smith, J.-T. Zhang, and S. A. Asher, Analytical Chemistry **87**, 5013 (2015).

[19] J. M. Weissman, H. B. Sunkara, A. S. Tse, and S. A. Asher, Science **274**, 959 (1996).

[20] J. R. Taylor, *An Introduction to Error Analysis* (University Science Books, Sausalito, California, 1982).

[21] P. L. Flaugh, S. E. O'Donnell, and S. A. Asher, Appl. Spectrosc. **38**, 847 (1984).

[22] R. J. Carlson and S. A. Asher, Appl. Spectrosc. **38**, 297 (1984).

[23] G. Pan, R. Kesavamoorthy, and S. A. Asher, Physical Review Letters **78**, 3860 (1997).

[24] C. E. Reese, A. V. Mikhonin, M. Kamenjicki, A. Tikhonov, and S. A. Asher, Journal of Americal Chemical society **126**, 1493 (2004).

[25] S.-H. Kim, S. Y. Lee, S.-M. Yang, and G.-R. Yi, NPG Asia Mater **3**, 25 (2011).

[26] Y. Iwayama, J. Yamanaka, Y. Takiguchi, M. Takasaka, K. Ito, T. Shinohara, T. Sawada, and M. Yonese, Langmuir **19**, 977 (2003).

[27] S.-i. Takata, K. Suzuki, T. Norisuye, and M. Shibayama, Polymer **43**, 3101 (2002).

[28] O. D. Velev, T. A. Jede, R. F. Lobo, and A. M. Lenhoff, Nature **389**, 447 (1997).

[29] J. E. G. J. Wijnhoven and W. L. Vos, Science **281**, 802 (1998).

[30] B. J. Ackerson and K. Schätzel, Physical Review E **52**, 6448 (1995).

[31] J.-J. Lietor-Santos, B. Sierra-Martin, R. Vavrin, Z. Hu, U. Gasser, and A. Fernandez-Nieves, Macromolecules **42**, 6225 (2009).

[32] D. M. Heyes and A. C. Branka, Soft Matter **5**, 2681 (2009).

[33] U. Gasser, J. S. Hyatt, J. J. Lietor-Santos, E. S. Herman, L. A. Lyon, and A. Fernandez-Nieves, The Journal of Chemical Physics **141**, 034901 (2014).

[34] R. S. H. L. Brannon-Peppas, *Absorbent Polymer Technonogy* (Elsevier Publishing Company, Amsterdam, 1990), Vol. 8, Studies in Polymer Science, p.^pp. 288.

[35] P. G. Bolhuis, D. Frenkel, S.-C. Mau, and D. A. Huse, Nature **388**, 235 (1997).

[36] L. V. Woodcock, Nature **385**, 141 (1997).

[37] P. N. Pusey, W. van Megen, P. Bartlett, B. J. Ackerson, J. G. Rarity, and S. M. Underwood, Physical Review Letters **63**, 2753 (1989).

[38] I. P. Dolbnya, A. V. Petukhov, D. G. A. L. Aarts, G. J. Vroege, and H. N. W. Lekkerkerker, EPL (Europhysics Letters) **72**, 962 (2005).

[39] S. Pronk and D. Frenkel, The Journal of Chemical Physics **110**, 4589 (1999).

[40] B. R. Saunders and B. Vincent, Advances in Colloid and Interface Science **80**, 1 (1999).

[41] C. L. A. Berli and D. Quemada, Langmuir **16**, 10509 (2000).

[42] A. Fernandez-Nieves, A. Fernandez-Barbero, B. Vincent, and F. J. d. l. Nieves, The Journal of Chemical Physics **119**, 6 (2003).

[43] A. Fernández-Nieves, A. Fernández-Barbero, B. Vincent, and F. J. de las Nieves, Langmuir **17**, 1841 (2001).

[44] K. S. Schmitz and L. B. Bhuiyan, Physical Review E **63**, 011503 (2000).

[45] I. Sogami and N. Ise, The Journal of Chemical Physics **81**, 6320 (1984).

[46] B. V. R. Tata, P. S. Mohanty, and M. C. Valsakumar, Solid State Communications **147**, 360 (2008).

[47] B. V. R. Tata and A. K. Arora, Journal of Physics: Condensed Matter **4**, 7699 (1992).

[48] Mallika Das, Hong Zhang, and, and Eugenia Kumacheva, Annual Review of Materials Research **36**, 117 (2006).

[49] B. Sierra-Martin, J. R. Retama, M. Laurenti, A. Fernández Barbero, and E. López Cabarcos, Advances in Colloid and Interface Science **205**, 113 (2014).

[50] Y. Guan and Y. Zhang, Soft matter **7**, 6375 (2011).

[51] Z. Meng, J. K. Cho, V. Breedveld, and L. A. Lyon, The Journal of Physical Chemistry B **113**, 4590 (2009).

[52] Y. Gao, X. Li, and M. J. Serpe, RSC Advances **5**, 44074 (2015).

[53] D. Schmaljohann, Advanced Drug delivery reviews **58**, 1655 (2006).

[54] J. Brijitta, B. V. R. Tata, and T. Kaliyappan, Journal of Nanoscience and Nanotechnology **9**, 5323 (2009).

[55] C. D. Jones and A. Lyon, Macromolecules **33**, 8301 (2000).

[56] L. A. Lyon, J. D. Debord, S. B. Debord, C. D. Jones, J. G. McGrath, and M. J. Serpe, The Journal of Physical Chemistry B **108**, 19099 (2004).

[57] J. Wu, B. Zhou, and Z. Hu, Physical Review Letters **90**, 048304 (2003).

[58] E. C. Cho, J. Lee, and K. Cho, Macromolecules **36**, 9929 (2003).

[59] B. R. Saunders, Langmuir **20**, 3925 (2004).

[60] J. Gao and B. J. Frisken, Langmuir **19**, 5217 (2003).

[61] I. Varga, T. Gilányi, R. Mészáros, G. Filipcsei, and M. Zrínyi, The Journal of Physical Chemistry B **105**, 9071 (2001).

[62] M. Stieger, W. Richtering, J. S. Pedersen, and P. Lindner, The Journal of Chemical Physics **120**, 6197 (2004).

[63] H. Senff and W. Richtering, The Journal of Chemical Physics **111**, 1705 (1999).

[64] H. Zhibing and W. Jianzhong, in *Dekker Encyclopedia of Nanoscience and Nanotechnology, Second Edition* (Taylor & Francis, 2009), pp. 2243.

[65] T. Hellweg, C. D. Dewhurst, E. Brückner, K. Kratz, and W. Eimer, Colloid and Polymer Science **278**, 972 (2000).

[66] A. Frenendaz-nieves, A. Fernández Barbero, B. Vincent, and F. J. de las Nives, The Journal of Chemical Physics **119**, 10383 (2003).

[67] J. Mattsson, H. M. Wyss, A. Fernandez-Nieves, K. Miyazaki, Z. Hu, D. R. Reichman, and D. A. Weitz, Nature **462**, 83 (2009).

[68] W. G. Hoover, S. G. Gray, and K. W. Johnson, The Journal of Chemical Physics **55**, 1128 (1971).

[69] R. Agrawal and D. A. Kofke, Molecular Physics **85**, 23 (1995).

[70] J. Brijitta, B. V. R. Tata, R. G. Joshi, and T. Kaliyappan, The Journal of Chemical Physics **131**, 074904 (2009).

[71] U. Gasser, J. J. Lietor-Santos, A. Scotti, O. Bunk, A. Menzel, and A. Fernandez-Nieves, Physical Review E **88**, 052308 (2013).

[72] D. Gottwald, C. N. Likos, G. Kahl, and H. Löwen, The Journal of Chemical Physics **122**, 074903 (2005).

[73] U. Gasser, B. Sierra-Martin, and A. Fernandez-Nieves, Physical Review E **79**, 051403 (2009).

[74] U. Gasser and A. Fernandez-Nieves, Physical Review E **81**, 052401 (2010).

[75] P. J. Flory, *Principles of Polymer chemistry* (Cornell University Press, Ithaca and London, 1953).

[76] T. Hino and J. M. Prausnitz, Journal of Applied Polymer Science **62**, 1635 (1996).

[77] G. Romeo, L. Imperiali, J.-W. Kim, A. Fernández-Nieves, and D. A. Weitz, The Journal of Chemical Physics **136**, 124905 (2012).

[78] R. G. Joshi, B. V. R. Tata, and J. Brijitta, AIP Conference Proceedings **1349**, 208 (2011).

[79] Y. Chen, J. E. Gautrot, Z. Li, and X. X. Zhu, Soft Matter **3**, 571 (2007).

[80] H. Sugiyama, T. Sawada, H. Yano, and T. Kanai, Journal of Materials Chemistry C **1**, 6103 (2013).

[81] J. Meid, T. Friedrich, B. Tieke, P. Lindner, and W. Richtering, Physical Chemistry Chemical Physics **13**, 3039 (2011).

[82] I. Lynch and K. A. Dawson, The Journal of Physical Chemistry B **108**, 10893 (2004).

[83] S. A. Asher, J. Holtz, L. Liu, and Z. Wu, Journal of the American Chemical Society **116**, 4997 (1994).

[84] N. C. Panoiu, M. Bahl, and J. R. M. Osgood, Optics Letters **28**, 2503 (2003).

[85] Y. Liu, Y. Zhang, and Y. Guan, Chemical Communications, 1867 (2009).

[86] R. Kimmich, *Principles of Soft-Matter Dynamics: Basic Theories, Non-invasive Methods, Mesoscopic Aspects* (Springer Netherlands, 2012).

[87] A. Van Blaaderen, J. Peetermans, G. Maret, and J. K. G. Dhont, The Journal of Chemical Physics **96**, 4591 (1992).

[88] R. G. Joshi, B. V. R. Tata, and J. Brijitta, The Journal of Chemical Physics **139**, 124901 (2013).

[89] M. Medina-Noyola, Physical Review Letters **60**, 2705 (1988).

[90] M. Das, H. Zhang, and E. Kumacheva, Annual Review of Materials Research **36**, 117 (2006).

[91] A. K. Arora and B. V. R. Tata, *Ordering and phase transitions in charged colloids* (Wiley - VCH, 1996), 1st edn., Complex fluids and fluid microstructure series.

[92] B. V. R. Tata, J. Brijitta, and R. G. Joshi, Int J Adv Eng Sci Appl Math **5**, 240 (2013).

[93] B. J. Frisken, Appl. Opt. **40**, 4087 (2001).

[94] A. Ashkin, J. M. Dziedzic, J. E. Bjorkholm, and S. Chu, Optics letters **11**, 288 (1986).

[95] J. Hu, K. Hiwatashi, T. Kurokawa, S. M. Liang, Z. L. Wu, and J. P. Gong, Macromolecules **44**, 7775 (2011).

[96] J. Meid, F. Dierkes, J. Cui, R. Messing, A. J. Crosby, A. Schmidt, and W. Richtering, Soft Matter **8**, 4254 (2012).

[97] F. Gruner and W. Lehmann, Journal of Physics A: Mathematical and General **13**, 2155 (1980).

[98] N. A. Mahynski, A. Z. Panagiotopoulos, D. Meng, and S. K. Kumar, Nature Communications **5**, 4472 (2014).

[99] M. Shibayama, F. Ikkai, S. Inamoto, S. Nomura, and C. C. Han, The Journal of Chemical Physics **105**, 4358 (1996).

[100] Burce J. Berne and Robert Pecora, *Dynamic light scattering* (John wiley & sons, New York, 1976).

[101] R. Finsy, Advances in Colloid and Interface Science **52**, 79 (1994).

[102] C. Urban and P. Schurtenberger, Journal of Colloid and Interface Science **207**, 150 (1998).

[103] V. C. Martelozzo, A. B. Schofield, W. C. K. Poon, and P. N. Pusey, Physical Review E **66**, 021408 (2002).

[104] M. Kerker, *The scattering of light* (Academic press, New York, 1969).

[105] P. N. Pusey, Current Opinion in Colloid & Interface Science **4**, 177 (1999).

[106] P. N. Pusey and W. Van Megen, Physica A: Statistical Mechanics and its Applications **157**, 705 (1989).

[107] H. Furukawa and S. Hirotsu, Journal of the Physical Society of Japan **71**, 2873 (2002).

[108] B. V. R. Tata, R. G. Joshi, D. K. Gupta, J. Brijitta, and B. Raj, Current Science **103**, 1175 (2012).

[109] M. Clements, S. R. Pullela, A. F. Mejia, J. Shen, T. Gong, and Z. Cheng, Journal of Colloid and Interface Science **317**, 96 (2008).

[110] S. Tang, Z. Hu, Z. Cheng, and J. Wu, Langmuir **20**, 8858 (2004).

[111] S. Tang, Z. Hu, B. Zhou, Z. Cheng, J. Wu, and M. Marquez, Macromolecules **40**, 9544 (2007).

[112] J. D. Debord and L. A. Lyon, The Journal of Physical Chemistry B **104**, 6327 (2000).

[113] A. M. Alsayed, M. F. Islam, J. Zhang, P. J. Collings, and A. G. Yodh, Science **309**, 1207 (2005).

[114] A. Ashkin, Physical review letters **24**, 156 (1970).

[115] R. M. Simmons, J. T. Finer, S. Chu, and J. A. Spudich, Biophysical Journal **70**, 1813 (1996).

[116] B. Lukić, S. Jeney, C. Tischer, A. J. Kulik, L. Forró, and E. L. Florin, Physical Review Letters **95**, 160601 (2005).

[117] A. Ashkin, Proceedings of the National Academy of Sciences **94**, 4853 (1997).

[118] G. Knöner, S. Parkin, T. A. Nieminen, N. R. Heckenberg, and H. Rubinsztein-Dunlop, Physical review letters **97**, 157402 (2006).

[119] M. Tassier, R. M. L. Evans, R. L. Warren, N. J. Bailey, and J. M. Cooper, New Journal of Physics **14**, 115032 (2012).

[120] Y. Hong, J.-W. Pyo, S. H. Baek, S. W. Lee, D. S. Yoon, K. No, and B.-M. Kim, Optics letters **35**, 2493 (2010).

[121] H. Maruyama, F. Arai, and T. Fukuda, Lab on a Chip **8**, 346 (2008).

[122] A. Ashkin, Biophysical Journal **61**, 569 (1992).

[123] T. Tlusty, A. Meller, and R. Bar-Ziv, Physical Review Letters **81**, 1738 (1998).

[124] K. C. Neuman and S. M. Block, Review of Scientific Instruments **75**, 2787 (2004).

[125] E. L. Florin, A. Pralle, E. H. K. Stelzer, and J. K. H. Hörber, Applied Physics A **66**, S75 (1998).

[126] M. Wordemann, *Structured light fields: Application in optical trapping, manipulation and organization* (Springer, Heidelberg, 2012).

[127] A. R. Zakharian, P. Polynkin, M. Mansuripur, and J. V. Moloney, Opt. Express **14**, 3660 (2006).

[128] W. H. Wright, G. J. Sonek, and M. W. Berns, Appl. Opt. **33**, 1735 (1994).

[129] A. Rohrbach and E. H. K. Stelzer, Appl. Opt. **41**, 2494 (2002).

[130] S. N. S. Reihani and L. B. Oddershede, Optics Letters **32**, 1998 (2007).

[131] W. P. Wong and K. Halvorsen, Opt. Express **14**, 12517 (2006).

[132] A. K. Arora and B. V. R. Tata, *Ordering and phase transitions in charged colloids* (Wiley - VCH, 1996), 1st edition edn., Complex fluids and fluid microstructure series.

[133] F. M. Fazal and S. M. Block, Nat Photon **5**, 318 (2011).

[134] Y. Kimura and P. R. Bianco, Analyst **131**, 868 (2006).

[135] T. A. Nieminen, V. L. Y. Loke, A. B. Stilgoe, G. Knöner, A. M. B. nczyk, N. R. Heckenberg, and H. Rubinsztein-Dunlop, Journal of Optics A: Pure and Applied Optics **9**, S196 (2007).

[136] H. C. V. d. Hulst, *Light Scattering by small particles* (Dover publications Inc., New york, 1981).

[137] M. Mohammadi, Advances in Colloid and Interface Science **62**, 17 (1995).

[138] J. P. Cook and D. J. Riley, Journal of Colloid and Interface Science **370**, 67 (2012).

[139] D. Frenkel and A. J. C. Ladd, The Journal of Chemical Physics **81**, 3188 (1984).

[140] Z. Cheng, W. B. Russel, and P. M. Chaikin, Nature **401**, 893 (1999).

[141] W. K. Kegel and J. K. G. Dhont, The Journal of Chemical Physics **112**, 3431 (2000).

[142] B. R. Saunders and B. Vincent, Journal of the Chemical Society, Faraday Transactions **92**, 3385 (1996).

[143] W. Jianzhong and H. Zhibing, in *Dekker Encyclopedia of Nanoscience and Nanotechnology, Second Edition* (Taylor & Francis, 2009), pp. 2243.

[144] H. Cynn, C. S. Yoo, B. Baer, V. Iota-Herbei, A. K. McMahan, M. Nicol, and S. Carlson, Physical Review Letters **86**, 4552 (2001).

[145] D. Errandonea, R. Boehler, S. Japel, M. Mezouar, and L. R. Benedetti, Physical Review B **73**, 092106 (2006).

[146] R. G. Joshi, HBNI, 2014.

[147] N. A. Mahynski, S. K. Kumar, and A. Z. Panagiotopoulos, Soft Matter **11**, 280 (2015).

[148] N. A. Mahynski, S. K. Kumar, and A. Z. Panagiotopoulos, Soft Matter **11**, 5146 (2015).

[149] N. A. Mahynski, A. Z. Panagiotopoulos, D. Meng, and S. K. Kumar, Nat Commun **5**, 1 (2014).

[150] J. R. Edison, T. Dasgupta, and M. Dijkstra, The Journal of Chemical Physics **145**, 054902 (2016).

[151] J. K. Cho, Z. Meng, L. A. Lyon, and V. Breedveld, Soft Matter **5**, 3599 (2009).

[152] Y. Xia, B. Gates, Y. Yin, and Y. Lu, Advanced Materials **12**, 693 (2000).

[153] D. J. Norris and Y. A. Vlasov, Advanced Materials **13**, 371 (2001).

[154] J. D. Joannopoulos, P. R. Villeneuve, and S. Fan, Nature **386**, 143 (1997).

[155] P. A. Rundquist, P. Photinos, S. Jagannathan, and S. A. Asher, The Journal of Chemical Physics **91**, 4932 (1989).

[156] Z. Hu, X. Lu, and J. Gao, Advanced Materials **13**, 1708 (2001).

[157] M. Chen, L. Zhou, Y. Guan, and Y. Zhang, Angewandte Chemie International Edition **52**, 9961 (2013).

[158] T. Kanai, D. Lee, H. C. Shum, and D. A. Weitz, Small **6**, 807 (2010).

[159] K. Lee and S. A. Asher, Journal of the American Chemical Society **122**, 9534 (2000).

[160] K. Kishore and K. N. Santhanalakshmi, Journal of Polymer Science: Polymer Chemistry Edition **19**, 2367 (1981).

[161] S. Nayak, S. B. Debord, and L. A. Lyon, Langmuir **19**, 7374 (2003).

[162] M. Shibayama, Macromolecular Chemistry and Physics **199**, 1 (1998).